Re-Os Chronostratigraphy of the Lower Jurassic Fernie Formation

By

Jonathan Alan Scott Toma

A thesis submitted in partial fulfillment of the requirements for the degree of

Master of Science

Department of Earth and Atmospheric Sciences
University of Alberta

Abstract

Biostratigraphy brackets the deposition of the Gordondale and Poker Chip Member of Lower Jurassic Fernie Formation between Late Hettangian and Early Toarcian stages. Through employing Re-Os chronostratigraphy we have expanded upon these previous age estimates by providing high-precision radiometric age constraints for subsurface upper and lower Gordondale Member contacts, and intermediate sections of the Gordondale Member of Northwestern Alberta, Canada of the Western Canadian Sedimentary Basin (WCSB). Re-Os data coupled with biostratigraphy and chemostratigraphy (Os, Sr) resolves the lower Gordondale Member contact to Late Sinemurian-Early Pliensbachian stages (191.14 ± 0.94 Ma and 192.0 ± 1.4 Ma), subunit 1B of the lower Radioactive Unit of the Gordondale Member to the Late Pliensbachian-Early Toarcian stage (183.9 ± 1.3 Ma), and the Gordondale-Poker Chip contact to an Early Toarcian stage (179.83 ± 0.60). In addition, characterization of the kerogen carbon isotopic composition of the Gordondale and Poker Chip Member has revealed correlations between ^{187}Re/^{188}Os and $\delta^{13}C_{kerogen}$ isotope fraction that implicate organic-matter type as a probable source for ^{187}Re/^{188}Os isotope fractionation. Lastly, experimental investigations of USGS material SBC-1 reveals cold and hot (subcritical) water to be an effective non-destructive extraction technique for the removal of Re and Os from Organic Rich Shales/Sedimentary rock (ORS), which has immediate implications for how fluid interacts with, and disturbs, the Re-Os systematics of ORS in geologic settings.

Acknowledgments

I would like to extend gratitude to my supervisor Dr. Robert Creaser for providing me with mentorship throughout the duration of this project. Without his academic assistance and funding support this project would not be possible. Sincere thanks are provided to Dr. Creaser's laboratory technicians Krystle Moore, Mark Simms, and Barbara Zinger for their assistance in analytical training. To Dr. Creaser's graduate students, Danny Hnantyshin and Sam Bowmen, I would like to thank for many of the fruitful discussions related and unrelated to geology and enthralling game nights that provided a much-needed break from the tedium of graduate life. Andy DuFrane and Guangcheng Chen of the ICPMS facility are thanked for their assistance related to data acquisition. I would also like to show appreciation to Dr. Karlis Muehlenbachs for allowing me to work with him on a side-project in his stable isotope lab and allowing me to drop by his office unannounced for extended discussions on geochemistry and its historical underpinnings. To my undergraduate thesis advisor, Dr. Chris Holmden of the University of Saskatchewan, I would like to thank for setting in motion an earnest fascination of the field of isotope geochemistry. Thanks is also given to the following from the Alberta Geologic Survey for their assistance with sample collection and sample archiving: Dinu Pană, Tyler Hauck, Tiffany Playter, Hilary Corlett, and Terry Poulton of the Geological Survey of Canada. Last but not least I would like to thank my forever loved, and soon-to-be wife, Karina Currie for her patience, support, and understanding of the demands of graduate life - for which I am eternally grateful.

Table of Contents

List of Tables

List of Figures

X

List of Abbreviations

$(CH_3)_2CO$ Acetone

C   Carbon

CIE   Carbon Isotope Excursion

CAMP   Central Atlantic Magmatic Province

$CHCl_3$ Chloroform

CrO_3 Chromium Trioxide

FCO   First Common Occurrence

FO   First Occurrence

GSSP   Global Boundary Stratotype Section and Point

HCl   Hydrochloric Acid

NJT   Jurassic Time scale Nannofossil Zone

HNO_3 Nitric Acid

LIP   Large Igneous Province

LCO   Last Common Occurrence

LO   Last Occurrence

OAE   Ocean Anoxic Event

ORS   Organic-rich Sedimentary Rocks

Os   Osmium

Re   Rhenium

NaOH   Sodium Hydroxide

Sr   Strontium

H_2SO_4 Sulfuric acid

SO_2 Sulfur Dioxide

T-OAE   Toarcian Ocean Anoxic Event

TOC   Total Organic Carbon

H_2O Water (dihydrogen monoxide)

WCSB   Western Canadian Sedimentary Basin

1| Introduction

1.1 Introduction

The Western Canada Sedimentary Basin (WCSB) is composed of a series sedimentary rock units deposited from the Proterozoic to Cenozoic era that extends from the Rocky Mountains to the Canadian Shield. Comprising the basin are stratigraphic units that are, in part, the source and reservoir rocks of the largest oil sand reserves in the world (Alberta's Energy, 2005). Stratigraphic beds of particular interest are organic-rich shales of the Lower Jurassic Fernie Formation of the WCSB that are the proposed source rocks of the Athabasca, Cold Lake and Peace River oil sands of Alberta, Canada (Finlay et al., 2012). These organic-rich sedimentary rocks (ORS) were deposited in the Panthalassa Ocean on the western margin of North America under transgressive-regressive cycles that yielded intermittently anoxic conditions during the Early Jurassic. By the Pliensbachian, terrane accretion and thrusting on the western margin of North America resulted in the development of a foreland basin, which may have amplified basin restrictivity (Pană et al., 2018a). High rates of organic matter (OM) accumulation coupled with optimal redox conditions lead to the widespread preservation of OM, and subsequent burial and maturation from Type I/II kerogen into bitumen. Prior to maturation, the average Total Organic Carbon (TOC) content of the basal shale units was estimated by Asgar-Deen (2003) to be as high as 30 wt.%. At the moment, it remains unclear as to whether OM enrichment in the basin was causally connected to either local or global Early Jurassic events. Recent chemostratigraphic evidence derived from Os and organic C isotope stratigraphy demonstrated that mid-to-upper stratigraphic units of the Gordondale Member and the lower sections of the Poker Chip Member overlap with the Toarcian Ocean Anoxic Event (T-OAE) (Them, 2016; Them et al., 2016, 2017). One effect of the T-OAE was the peripheral spread of coastal anoxia conducive for high rates of OM preservation (Jenkyns, 2010), which presents itself as a potential candidate for implicating OM enrichment in the basin. Prior to this event, Boreal ammonite zones *Echioceras raricostatum* and *Uptonia jamesoni* of the Late Sinemurian-Early Pliensbachian experienced similar, albeit more limited in

extent, rates of OM preservation that resulted in the widespread deposition of bituminous shales in Europe (Duarte et al., 2010; Gómez et al., 2016). Extensive organic matter enrichment (TOC = 20 wt.%) and Type II oil-prone kerogen, for example, found in the Lusitanian Basin located in Portugal is a comparable analogue to the Gordondale Member (Duarte et al., 2012; Riediger et al., 1991). Interestingly, the carbonate ramp system of the Lusitanian Basin, and the resulting organic-rich intervals are reminiscent of the relationship between the Nordegg carbonate ramp and the Gordondale carbonaceous ORS of the Lower Fernie Formation of the WCSB. Discriminating between these Early Jurassic events, by way of delimiting accurate and precise time markers for shale packages of the Lower Fernie Formation, provides an opportunity to resolve the underlying cause of OM enrichment in the WCSB.

Researchers since the 1950s have characterized the biostratigraphy of the Lower Fernie Formation of the WCSB using macro- and micro-faunal assemblages, which bracket its depositional age between Hettangian and Toarcian stages of the Early Jurassic (Spivak, 1949; Frebold, 1957). Emergent radioisotopic geochronometers in turn have provided a robust numerical framework for constraining the depositional history of stratigraphic units, including stratigraphic members, such as the Red Deer Member, of the Lower Fernie Formation (Hall et al., 2004). Two commonly employed chronostratigraphic methods include (1) U-Pb zircon dating and (2) ^{40}Ar/^{39}Ar sanidine dating of interstratified volcanic (tuff and/or tephra) ash layers and/or volcanic lava flows (Gradstein, 2012). Dating interstratified volcanic ash layers provides a direct measure for constraining the depositional age for a stratigraphic unit, whereas dating volcanic lava flows at most provides an upper or lower limit estimate on the age of the stratigraphic unit. The former geochronometer has been successfully applied to multiple interstratified bentonite ash layers of the Red Deer Member, yielding both multi-grain and single-grain U-Pb zircon ages with a precision < 1% that agree with intercalated ammonite and coccolith flora (Hall et al., 2004). Uranium-Lead zircon dating of ash layers, however, can be complicated by Pb-loss through crystal radiation damage as U decays to Pb and/or inheritance of older (xenocrystic) grains in the form of cores surrounded by younger (phenocrystic) overgrowth rims, which may bias the volcanic ash age to *appear* younger or older than it truly is (Bowring et al., 2006). In the case of the latter example, xenocrystic cores may account for up

to half of the total zircons analyzed for U-Pb zircon tuff/tephra geochronology (Bowring et al., 2006). This hinders the application of multi-grain U-Pb zircon data for high-precision geochronology and has become the main reason why single-grain U-Pb CA-TIMS zircon dating has supplanted the multi-grain U-Pb zircon approach (Gradstein, 2012).

The development of a third chronostratigraphic method over the past two and half decades, namely the Rhenium-Osmium (Re-Os) ORS geochronometer, provides an alternative, albeit complimentary, approach for temporally reconstructing the stratigraphic record (Cohen et al., 1999; Creaser et al., 2002; Ravizza and Turekian, 1989). By exploiting the natural radioactive decay of ^{187}Re into ^{187}Os through accessing the hydrogenous Re and Os component present in the organic matter of organic-rich sediment acquired during marine anoxic sediment deposition, the timing of sediment deposition can be constrained to within < 1% uncertainty in some cases (Selby and Creaser, 2003; Selby and Creaser, 2005). Measuring the hydrogenous Re and Os component of ORS has the ancillary advantage of providing a means for characterizing the Os isotopic composition of contemporaneous seawater, which can be employed as a paleo-oceanographic tracer (Cohen et al., 1999; Cohen et al., 2004). These two facets of the Re-Os ORS chronometer coupled with argillaceous sediments (shale) dominion over the exogenic environment have resulted in widespread applications ranging from Late Jurassic Timescale calibration to tracing millennial scale glacial movements of the Pleistocene (Garrels and Mackenzie, 1969; Rooney et al., 2016; Selby, 2007).

Preliminary studies of Finlay et al. (2012) have attempted to date sections of the Gordondale Member using Re-Os ORS geochronology, but variable ^{187}Os/^{188}Os$_i$ ratios hampered their attempts, resulting in highly imprecise, although biostratigraphically consistent, Early Jurassic age of 184 ± 29 Ma (Finlay et al., 2012). Here we aim to build upon previous work carried out by Hall et al. (2000), Asgar-Deen (2003), Asgar-Deen et al. (2003, 2004), and Finlay et al. (2012) detailing the biochronology and geochronology of the Gordondale and Poker Chip Member of the Lower Fernie Formation by employing Re-Os ORS geochronometry to constrain the precise temporal history of deposition. This is complemented with ^{87}Sr/^{86}Sr chemostratigraphy, to provide subsidiary constraints for radiometric dates. In addition, the

kerogen carbon (C) isotopic composition of the Gordondale and Poker Chip members is examined to further expand upon the relationship between Re and Os and organic matter. Lastly, experimental work involving Re and Os partitioning between ORS and subcritical water is explored to better understand Re and Os mobility during hot fluid-rock interactions, which may have implications for mobility during continental weathering and/or diagenesis, or hydrothermal fluid interaction.

2|Rhenium-Osmium Systematics

2.1 Re and Os Elemental Chemistry

Rhenium (Re) is a transition metal with atomic number 75 located in Group 7b and Period 6 of the Periodic Table, and has comparable geochemical characteristics to transition elements Molybdenum (Mo) and Manganese (Mn), Rhenium has nine oxidation states that range from -1 to +7 and two naturally occurring isotopes, mass ^{185}Re and ^{187}Re (Shirey and Walker, 1998). Mass ^{185}Re is a stable isotope of Re with an isotopic abundance of 37.40 % ± 0.02 in nature, whereas mass ^{187}Re is an unstable radionuclide of Re with a natural abundance of 62.60 % ± 0.02 (Berglund and Wiser, 2011). The radioactive nuclide ^{187}Re decays by beta emission into the stable isotope ^{187}Os, and forms the basis of the ^{187}Re-^{187}Os geochronometer. The transmutation of ^{187}Re into ^{187}Os, depicted in the decay equation (2.1), generates a proton (Z), a negatron (e$^-$), and an electron antineutrino ($\bar{v}_e$), while simultaneously emits 2.65 KeV of energy equivalent to ~ 1/25th of the binding energy of the ^{187}Re atom.

$$Equation\ (2.1)\ {}^{187}_{75}Re \rightarrow\ {}^{187}_{76}Os + e^- +\ \bar{v}_e$$

The rate at which the parent isotope, ^{187}Re, decays into its daughter isotope, ^{187}Os, can be expressed both in terms of its *decay constant* (λ) and *half-life* (T$_{1/2}$). Historically, attempts at measuring the ^{187}Re decay constant have been made through laboratory experiments and geological measurements (Dickin, 2018). However, the former have hampered accurate measurements of ^{187}Re decay constant, though Smoliar et al. (1996) were able to revise previous estimates of ^{187}Re decay constant to 1.666 x 10^{-11} yr^{-1} (T$_{1/2}$ = 4.16 x 10^{10} yr) through cross-referencing ^{187}Re-^{187}Os ages of group IIIA iron meteorites with precisely measured, and presumably coeval, ^{53}Mn-^{53}Cr angrite meteorite crystallization ages, which has now become the more widely accepted and used decay constant (Dickin, 2018). Attempts at refining the ^{187}Re decay constant of Smoliar et al. (1996) were made by Selby et al. (2007) via intercalibrating the ^{187}Re-^{187}Os molybdenite chronometer with the ^{238}U-^{206}Pb zircon chronometer in temporally-related magmatic systems, which successfully yielded a value of 1.667 x 10^{-11} yr^{-1} (± 0.31%) that

agrees within error of earlier estimates by Smoliar et al. (1996), and thereby established the ^{187}Re decay constant of 1.666 x 10^{-11} yr^{-1} as the most accurate and precise estimate to date.

Osmium (Os) is a platinum group element with atomic number 76, sharing geochemical affinities with Ru, Rh, Pd, Re, Ir, and Pt, and is located in Group 8 and Period 6 of the Periodic Table. Osmium has eleven oxidation states that range from -2 to +8 and seven naturally occurring isotopes with corresponding abundances of: ^{184}Os = 0.02 ± 0.01, ^{186}Os = 1.59 ± 0.03, ^{187}Os = 1.96 ± 0.02, ^{188}Os = 13.24 ± 0.08, ^{189}Os = 16.15 ± 0.05, ^{190}Os = 26.26 ± 0.02, and ^{192}Os = 40.78 ± 0.019 (Berglund and Wiser, 2011; Shirey and Walker, 1998). There are two radiogenic isotopes of Os, mass ^{187}Os and ^{186}Os. As discussed previously, the former isotope, ^{187}Os, is the radiogenic daughter product of the beta decay of ^{187}Re, whereas the later isotope, ^{186}Os, is the radiogenic daughter product of the alpha decay of ^{190}Pt, and has a half-life of $T_{1/2}$ = 4.9 x 10^{11} years (Dabek and Halas, 2007). Mass ^{186}Os is in turn radioactive and decays via alpha emission into ^{182}W, which has a half-life of $T_{1/2}$ = 2.0 x 10^{15} years (Dabek and Halas, 2007). The exceedingly large half-life of ^{186}Os, however, means that it can be assumed to be stable for geological purposes.

2.2 Re and Os in the Crust and Mantle

The Re-Os isotope system is unique amongst other radioisotope systems (Rb-Sr, Sm-Nd, and U-Pb), in that both elements are incompatible with lithophile (silicate) phases and compatible with chalcophile (sulfide), siderophile (iron-metal), and organophile (reduced organic matter) phases (Allègre and Luck, 1980; Carlson, 2005). As a result, Re and Os are scarcely present in quantities exceeding parts per trillion (ppt) levels in the upper continental crust (UCC) (Re= 207 ppt; Os = 31 ppt), while remaining enriched at the parts per billion (ppb) level in host-metallic and -sulfide phases that dominate the core-mantle reservoirs (Dubin and Peucker-Ehrenbrink, 2015; Shirey and Walker, 1998). By comparison, the fraction of crustal Re and Os relative to the mantle reservoir is ~5 x 10^{-3} and ~5 x 10^{-5} (Dubin and Peucker-Ehrenbrink, 2015). The preferential enrichment of Re over Os in the crustal reservoir is related to differences in partitioning behaviour during partial melting of the mantle. Rhenium is moderately

incompatible in the mantle and Os is compatible in the mantle (Carlson, 2005). During mantle partial melting, Re will be enriched in the melt phase, while Os will be enriched in the residue phase (Carlson, 2005; Shirey and Walker, 1998). Allègre and Luck (1980) expressed the Re/Os fractionation between silicate phases in mathematical terms using an enrichment factor (f = $(ReOs)_A$ /$(Re/Os)_{mantle}$), and calculated an enrichment factor of 300 for tholeiitic basalts and 100 for granites when normalized to mantle peridotites, whereas follow-up studies have found a $^{187}Re/^{188}Os$ fractionation of 50 in the continental crust and 0.4 in the fertile mantle (Esser and Turekian, 1993; Shirey and Walker, 1998). The Re/Os fractionation in the crustal reservoir coupled with time-integrated changes of ^{187}Re to ^{187}Os has resulted in a radiogenic crustal reservoir ($^{187}Os/^{188}Os_i$ = 1.26) that is isotopically distinct from the unradiogenic mantle reservoir ($^{187}Os/^{188}Os_{iDepletedMantle}$ = 0.113; $^{187}Os/^{188}Os_{iPrimitiveMantle}$ = 0.1296) (Carlson, 2005; Esser and Turekian, 1993, Shirey and Walker, 1998). The isotopic heterogeneity of the crust-mantle reservoirs has in turn permitted researchers to conduct petrogenetic tracer studies involving crustal evolution, crustal contamination, and seawater Os isotope evolution (Allègre and Luck, 1980).

2.3 Crustal Budget of Re and Os

The Re and Os crustal budget is divided amongst its sources (inputs) and sinks (outputs). Broadly speaking, crustal sources fall into two isotopic end-members: radiogenic and unradiogenic sources. Crustal sources that fall in the former end-member include eroding continental crust (Re_{UCC} = 207 ppt; Os_{UCC} = 31 ppt; $^{187}Os/^{188}Os$ = 1.26), eroding organic-rich sediments (ORS) ($^{187}Os/^{188}Os$ = 2.2-2.42) and aeolian dust ($^{187}Os/^{188}Os$ = 1.05), whereas those that fall in the latter end-member include hydrothermal input to the oceans ($^{187}Os/^{188}Os$ = 0.113), cosmic dust ($^{187}Os/^{188}Os$ = 0.127), eroding mafic/ultramafic rocks ($^{187}Os/^{188}Os$ = 0.113) (Dubin and Peucker-Ehrenbrink, 2015; Meisel et al., 1996) (Figure 2.1). Crustal sinks of Re and Os include sulfide deposits, organic-rich sediments, either in the form of anoxic marine or lacustrine muds, and the ocean reservoir. Sulfide deposits contain up to 5 ppm and 50 ppb of hydrothermally sourced Re and Os ($^{187}Os/^{188}Os$ = 0.113) (Hannah and Stein, 2002). Anoxic marine and lacustrine muds, however, contain up to hundreds of ppb Re and several ppb Os,

and have temporally variable Re and Os isotopic compositions related to the input source (i.e. continental vs. hydrothermal) of hydrogenous Os in the water column (Cohen, 2004; Dubin and Peucker-Ehrenbrink, 2015). The Re and Os isotopic composition of modern marine muds, for example, reflects the isotopic signature of contemporaneous seawater (Sharma et al., 1997, Peucker-Ehrenbrink Ravizza, 2000). The modern ocean reservoir, which contains up to 7.42 ppt and 9.82 ppq of predominantly fluvial (30 %) sourced Re and Os, has a radiogenic $^{187}Re/^{188}Os$ and $^{187}Os/^{188}Os$ isotopic composition of 4,200 and 1.06 (see Figure 2.1) (Peucker-Ehrenbrink Ravizza, 2000). Therefore, reconstructing the Re and Os isotopic composition of the ocean reservoir in deep time is made available by measuring the Re and Os isotopic composition of contemporaneous ORS.
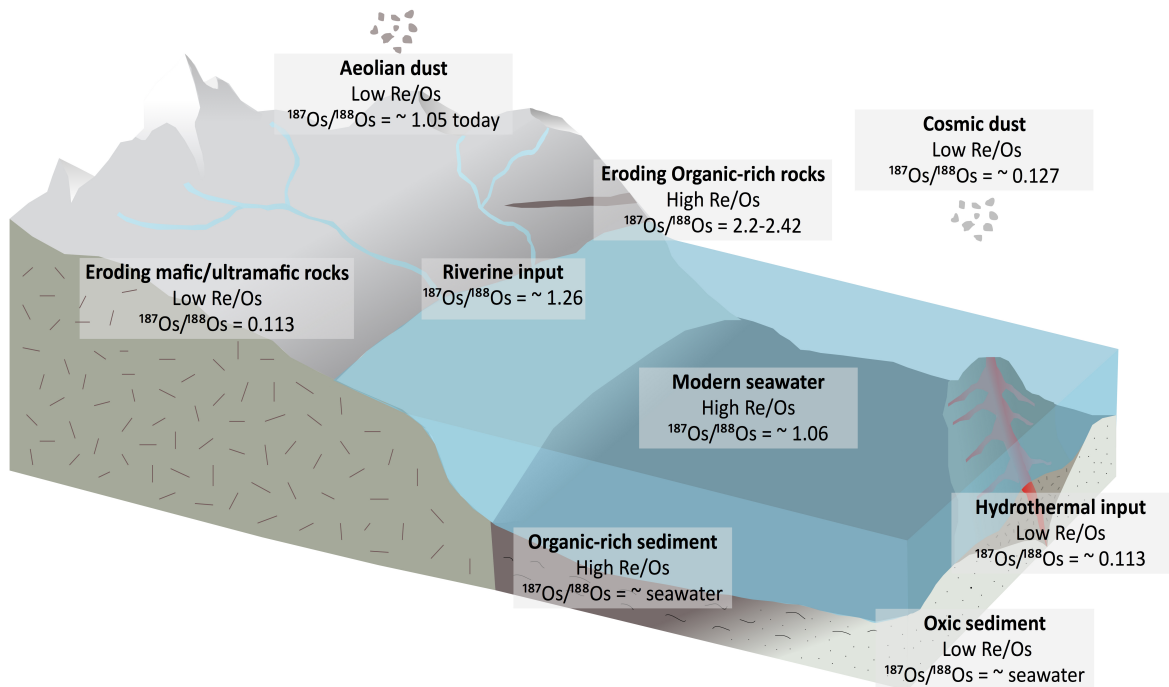
Figure 2.1 Schematic detailing Re/Os and $^{187}Os/^{188}Os$ of various crustal sources and sinks (modified after Cohen, 2004; Peucker-Ehrenbrink and Ravizza, 2000; Strauss et al., 2013).

2.4 Marine Os Isotope Record

The Os isotopic composition of marine muds is controlled by the various fluxes of Os to the marine budget, which for the modern ocean includes fluvial input ([Os] = 295 kg/yr), mantle/extraterrestrial input ([Os = 126 kg/yr), and aeolian input ([Os = 28 kg/yr) (Levasseur et al., 1999; Peucker-Ehrenbrink and Ravizza, 2000). A predominantly fluvial input of Os to the modern ocean is reflected in its modern Os isotopic composition (1.06). The Os inventory of the ocean is, however, expected to vary on geologic time scales exceeding its residency time in the ocean (10-40 Ka) (Peucker-Ehrenbrink and Ravizza, 2000). At this level of temporal resolution the marine Os budget will reflect either a homeostasis between its Os inputs or a single Os flux disproportionally dominating the marine landscape. In the latter case, a geologic event, in the form of rapid continental weathering, meteorite impact, and Large Igneous Province (LIP) eruption, can exert enough control over the marine Os budget such that major Os isotopic perturbations are recorded in the marine rock record (Cohen, 2004). While such geologic events are rare, perturbations of this magnitude have been documented across both Precambrian and Phanerozoic eons (Cohen, 2004; Kendall et al. 2015; Turgeon and Creaser, 2008; Them et al., 2017). A salient example is the bolide impact that resulted in the K-T mass extinction event that shifted the Os isotopic composition of seawater from a pre-K-T value of ~ 0.45 to ~ 0.2 at the K-T boundary by delivering a near-instantaneous amount of 1.9×10^{7} kg of dissolved Os to the oceans (Peucker-Ehrenbrink and Ravizza, 2000). Comparable geologic events, such as the Cenozoic Ocean Anoxic Event 2 (OAE2) triggered by LIP emplacement, contributed 97% of the total Os flux to the oceans during the entire 550 Ka interval, and resulted in an unradiogenic Os isotope seawater composition with values that ranged from 0.2 and 0.1 (Turgeon and Creaser, 2008).

However, it is not universally observed that every perturbation recorded in the marine rock record is tied to a major geologic event. For example, anoxic muds control a disproportionate fraction of the Re (70%) and Os (10%) upper Continental Crustal (UCC) budget that when eroded have the potential to dramatically shift the scale of the Os budget in their direction

(Dubin and Peucker-Ehrenbrink, 2015). Similarly, marine sedimentary basins restricted from the open ocean can superficially record Os isotopic perturbations even when the inputs of Os to the open ocean are in a homeostasis (McArthur et al., 2008, Poirier and Hillaire-Marcel, 2009). This occurs when rapid drawdown of Re and Os from the water column to the sediment-water interface perturbs the Os isotope composition of restrictive basins, such that localized isotopic heterogeneities dominate organic-rich facies (McArthur et al., 2008).

Therefore, in order to reconstruction a meaningful marine Os-isotope record, multiple coeval marine anoxic muds of disparate spatial localities need to be correlated to eliminate the possibility of mischaracterizing localized *Os-isotope excursions* as global events. Additionally, restricted basins have the adverse effect of compromising efforts to date organic-rich sedimentary rocks using the Re-Os isochron method, due to widely fluctuating Os isotopic compositions in the water column over short timescales reflected in the sedimentary archive (McArthur et al., 2008; Turgeon et al., 2007).

2.5 Re and Os in Organic-rich Sediments

Rhenium in seawater consists of a mixture of particulate and dissolved phase Re. The former fraction is unreactive in seawater, and consequently settles to the seafloor to form the detrital component of Re ($Re_{detrital}$ = 0.05-0.5 pbb) in marine sediment, whereas the latter fraction permeates seawater as the stable heptavalent perrhenate ion (ReO_4^-), and is reductively captured by organic matter as Re(IV) to form the hydrogenous component of marine sediment (Koide et al., 1986; Morford and Emerson, 1999). A positive correlation between Re and total organic carbon (TOC) provides first-order evidence of organic matter being the primary host of hydrogenous Re (Ravizza and Turekian, 1989; Selby and Creaser, 2003). Hydrogenous Re, though, is not exclusively bound to organic matter, and may, albeit in a smaller quantity, be incorporated in the crystal lattice of syngenetic pyrite (Wright, 2015). The bulk hydrogenous component of Re, however, accounts for up to 99% of the total Re budget of organic-rich sediment (Cohen et al., 1999; Dubin and Peucker-Ehrenbrink, 2015; Morford and Emerson, 1999).

Hydrogenous Re is, nevertheless, unevenly distributed in marine sediment (Koide et al., 1986). The lowest concentrations of hydrogenous Re are found in oxic sediment, such as argillaceous shales, Fe-Mn nodules or Fe-Mn oxides, and pelagic sediments (Koide et al., 1986; Morford and Emerson, 1999). The Re concentration in oxic sediment is reported to be < 0.01 ppb Re, comparable to UUC Re concentrations, and thereby of predominantly terrigenous origin. By contrast, the highest concentrations of hydrogenous Re are found in anoxic sediment, such as organic-rich mudstones, which are typically defined as having > 1 wt.% TOC (Koide et al., 1986). For example, the hydrogenous Re concentration in organic-rich mudstones is as high as 500 ppb (Dubin and Peucker-Ehrenbrink, 2015). Consequently, for marine sediment, the sediment redox regime is the discriminant factor for authigenic Re enrichment.

The tendency for anoxic sediment to become enriched in hydrogenous Re, however, is not directly controlled by the redox conditions of the water column (see Figure 2.2). The observation that dissolved Re is conservative in oxic and anoxic seawater has eliminated the hypothesis that suspended and/or settling organic matter sequesters appreciable quantities of hydrogenous Re from the water column prior to sediment deposition (Anbar et al., 1991; Colodner et al., 1993; Ravizza et al., 1991). Instead, Re enrichment likely occurs via diffusion at or below the sediment water interface as dissolved Re in pore water is reduced to an insoluble organo-complex (Crusius and Thomson, 1999). The degree of Re reduction, however, is proportional to the dissolved O_2 content of the pore water and the rate of organic carbon oxidation (Calvert and Pederson, 1993; Colodner et al., 1993; Crusius et al. 1996; Morford et al., 2011). Interestingly, the presence of dissolved H_2S has been shown to exert little influence over removal of dissolved Re from pore waters and its subsequent uptake by sulfidic sediment (Calvert and Pederson, 1993; Sundby et al., 2004). With that said, the removal of Re from pore waters in conjunction with its reductive incorporation into organic-rich sediment is likely governed by slow precipitation kinetics (Sundby et al., 2004; Yamashita et al., 2007). This in turn will restrict the Re burial flux rate in organic-rich sediments, which is estimated to range from 1.2-2.4 x 10^{-6} µmol/cm2/yr to 0.88 pmol/cm2/y (Morford et al., 2011; Sundby et al., 2004).
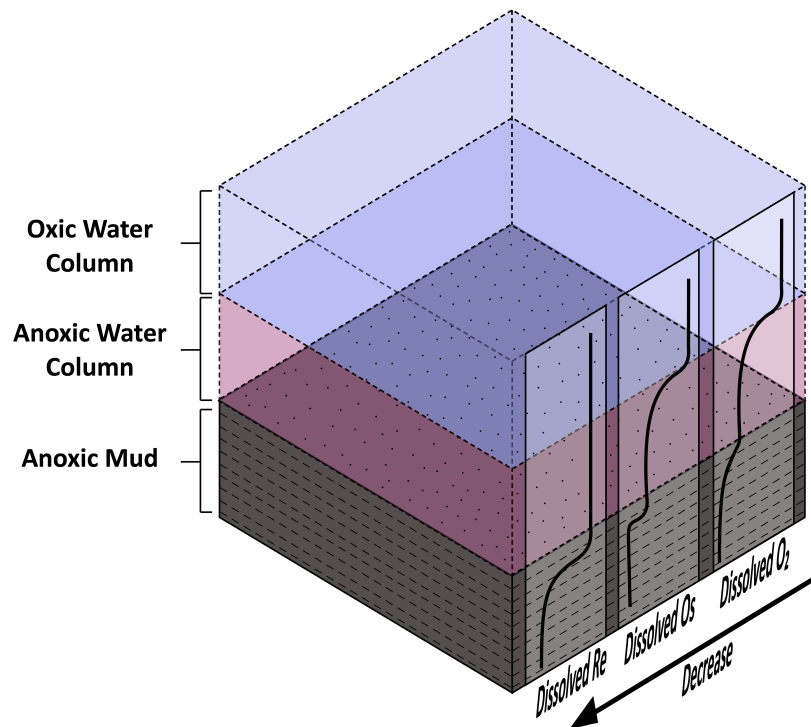
Figure 2.2 Conceptual model depicting the removal of dissolved Re and Os from seawater along a redox gradient.

Osmium is incorporated into marine sediment in both dissolved and particulate form. The former fraction is present in oxic seawater as an octavalent oxyanion ($H_3OsO_6^-$ or $HOsO_5^-$) that upon reduction to Os(IV) hydroxide or insoluble Os(III) forms the hydrogenous Os component of marine sediment, whereas the latter fraction forms the detrital/extraterrestrial Os component of marine sediment (Cohen, 2004; Yamashita et al., 2017). Hydrogenous Os is incorporated into marine sediment as organic-matter, sulfide, ferromanganese, and/or metalliferous bound Os (Koide et al., 1991; Ravizza and Turekian, 1989). Hydrogenous Os, however, constitutes the bulk reservoir for Os in marine sediment, with enrichments in excess of 1000's of ppt. In contrast, detrital Os contributes the smallest fraction to marine sediment with average concentrations similar to the UCC (0.08 ppb) (Dubin and Peucker-Ehrenbrink, 2015).

Hydrogenous Os, in contrast to Re, is enriched in both anoxic/suboxic and oxic sediment (Koide et al., 1991; Ravizza and Turekian, 1989; see Figure 2.2). Enrichments of the latter include ferromanganese oxides and metalliferous sediment, whereas enrichments of the former include organic-rich sediments and syngenetic pyrite. Ferromanganese oxides formed in deep-sea pelagic settings have average concentrations of 1.0 ppb or 100 times greater than crustal concentrations, whereas organic-rich sediment and syngenetic pyrite formed in anoxic settings exhibit average concentrations of 0.454 ppb and (UCC = 0.031 ppb) (Dubin and Peucker-Ehrenbrink, 2015; Koide et al., 1991). Due to the slow Os burial flux (6×10^{-4} pg/cm^3/yr) in oxic settings relative to those found in anoxic/suboxic settings (2-16 pg/cm^3/yr and 2-12 pg/cm^3/yr), Fe-Mn oxides contribute a marginal fraction to the marine Os budget (Lu et al., 2017). With that said, the rate of Os burial flux in anoxic/suboxic settings varies with respect to basin restrictivity and local redox conditions (suboxic vs. anoxic vs. euxinic).

Whereas organic matter is the primary host-phase for hydrogenous Os in organic-rich sediment, it still remains unclear whether dissolved Os is primarily removed from seawater in the water column or at or below the sediment water interface. Woodhouse et al. (1999) observed non-conservative behaviour in dissolved Os in a vertical profile of the Pacific Ocean that was interpreted as evidence of its partial removal from seawater by settling particles in the water column. Removal of dissolved Os (30%) coincided with a ~500 m oxygen minimum zone, which suggested that Eh conditions in the water column induced adsorptive properties in dissolved Os such that it became particle reactive (Woodhouse et al., 1999). However, a change in Eh conditions ~ 2000 m below this point resulted in desorption of dissolved Os, and its subsequent increase in concentration in the water column (Woodhouse et al., 1999). Experimental studies involving the exchange of dissolved Os in artificial seawater and reduced sediments have confirmed non-conservative behaviour in Os (Yamashita et al., 2007). However, the study concluded that the Os uptake pathway into reducing sediment occurred at or below the sediment water interface. Both these studies suggest that sequestration of dissolved Os from seawater occur both in the water column and at or below the sediment water interface.

2.6 Re-Os Geochronometry of Organic-rich Sedimentary Rocks (ORS)

Re-Os geochronometry of ORS functions by exploiting the natural radioactive decay of ^{187}Re into ^{187}Os (Ravizza and Turekian, 1989). The isochron method is used to compensate for the presence of common Os in ORS prior to any time-integrated changes of ^{187}Re into ^{187}Os. The isochron method requires selecting a suite of samples that are (1) cogenetic, (2) homogeneous in their ^{187}Os/^{188}Os$_i$ isotopic composition, (3) isotopically closed, meaning no losses/gains of parent/daughter isotopes, since the time-integrated change of ^{187}Re into ^{187}Os (i.e. $t > 0$), and (4) heterogeneous in their ^{187}Re/^{188}Os ratios. Satisfying each of these geochronological tenets yields a linear relationship termed an "isochron" on an ^{187}Re/^{188}Os (x) ^{187}Os/^{188}Os (y) plot (Figure 2.3). The measured ^{187}Re/^{188}Os$_m$ and ^{187}Os/^{188}Os$_m$ ratios of each sample (S$_1$, S$_2$, S$_3$, etc.) form this straight line, which has a slope ($e^{\lambda t}$-1) that yields the age of the ORS. The ^{187}Os/^{188}Os$_i$ ratio is derived from the y-intercept of the isochron and is interpreted as the Os isotopic composition of contemporaneous seawater. Alternatively, a Re-Os ORS age can be quantified by manipulating the Re-Os isochron equation (2) to solve for the time component (t).

$$Equation\ (2)\ \ \left(\frac{^{187}Os}{^{188}Os}\right)_m = \left(\frac{^{187}Os}{^{188}Os}\right)_i + \left(\frac{^{187}Re}{^{188}Os}\right)_m (e^{\lambda t} - 1)$$

In order to assess the quality of an isochron, York (1969) developed a statistical parameter termed, *Mean Squared Weighted Deviates* (MSWD), which measures the degree of scatter from the regression line. Linear regressions with scatter predicted from analytical errors yield an MSWD = 1, whereas scatter in excess of that predicted from analytical errors yield an MSWD > 1, and scatter less than that predicted from analytical errors yield an MSWD < 1 (Dickin, 2017). In the first and third case, the regression is termed an isochron and yields a Model 1 age on the Microsoft add-on program *Isoplot*, whereas in the second case, the regression is termed an errorchron, and yields a Model 3 age, where excess scatter about the linear regression is related to geological influence (Ludwig, 2012). Although MSWD provides a

useful statistical proxy for eliminating erroneous ages, it fails to account for the geological reasons that an age is erroneous. If the geological scatter is identifiably related to either (1) invariability in the $^{187}Re/^{188}Os$ ratios between samples and/or (2) variability in the $^{187}Os/^{188}Os_i$ ratios between samples, then an errorchron with an MSWD = 2.5 or less can be assigned as an isochron with reduced confidence in the purported age (Dickin, 2017). In addition to MSWD, *Isoplot* incorporates the *probability of fit index* as a second quality check for assessing the legitimacy of an isochron by measuring the confidence (i.e. probability) that scatter about the regression is related to the assigned analytical errors (Ludwig, 2012). Ludwig (2012) deems a 15% probability of fit as an acceptable demarcation line for a good quality isochron.
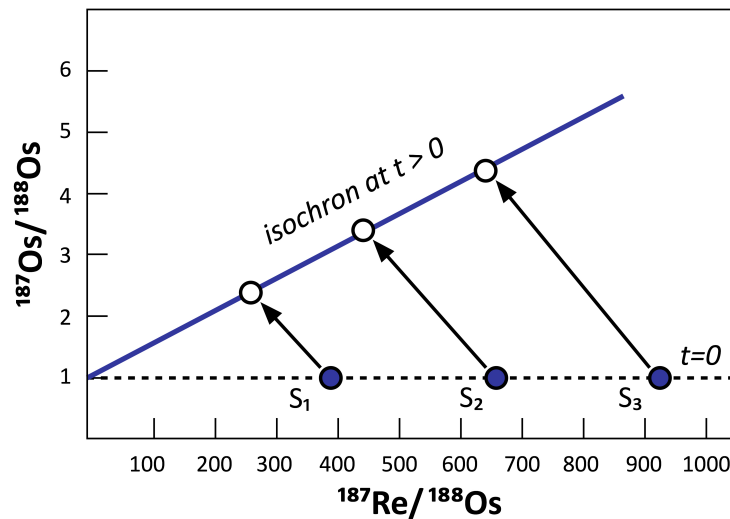
Figure 2.3 Archetype of the Re-Os isochron method. At *t = 0* the sample points (S$_1$, S$_2$, S$_3$) have the same $^{187}Os/^{188}Os_i$ ratio, represented by the horizontal dashed line intersecting the Y-axis at 1, and different $^{187}Re/^{188}Os$ ratios. At *t > 0* the points align to form a straight line defined as an isochron, which has a slope of ($e^{\lambda t}$-1) and Y-intercept ($^{187}Os/^{188}Os_i$) of 1. The points at *t > 0* are measured on a Negative Thermal Ionization Mass Spectrometer (NTIMS) and represent the present-day parent-daughter isotopes of the rock.

Ravizza and Turekian (1989) were first to apply the ^{187}Re-^{187}Os system, via the isochron method, to ORS geochronometry and infer $^{187}Os/^{188}Os_i$ potential as a paleo-oceanographic tracer. Subsequent advances in Re-Os systematics, mass spectrometry, and spike-sample

equilibration allowed Cohen et al. (1999) to obtain the first precise (2%-7% [2σ]) Re-Os depositional ages of Jurassic ORS that agreed within uncertainty of the known Hettangian, Toarcian, and Kimmeridgian depositional ages (Creaser et al., 1991; Shirey and Walker, 1995). Cohen et al. (1999) focused on immature ORS (TOC > 5 wt.%) due to the Barre et al. (1995) claim of observations of Re and Os fractionation during hydrocarbon maturation. However, the effect of hydrocarbon maturation on Re-Os systematics in ORS was re-examined by Creaser et al. (2002). Isochron regression of the Re-Os data, which included immature, mature, and overmature samples of the Exshaw Formation, yielded a depositional age of 358 ± 10 Ma (2σ; Model 3) that agreed within uncertainty of a U-Pb zircon age (363.6 ± 1.6 Ma) obtained from a proximal volcanic ash bed (Tucker et al., 1998). In addition, separate regressions of immature and mature/overmature samples yielded ages (351 ± 23 and 360 ± 13 Ma) that were statistically indistinguishable at the 2σ level (Creaser et al. 2002), which demonstrated, contrary to Barre et al. (1995), that the Re-Os systematics of ORS remained robust at temperatures of 150°C (Creaser et al., 2002). The discrepancy in Re-Os systematics between source rock and hydrocarbons reported by Barre et al. (1995) was, alternatively, argued by Creaser et al. (2002) to reflect inadequate spike-sample equilibration. Hydrous pyrolysis experiments by Rooney et al. (2009) have since confirmed Creaser et al. (2002) previous findings that negligible Re-Os isotopic fractionation occurs during oil generation.

Kendall et al. (2004) expanded the scope of Re-Os ORS geochronometry further to low TOC (< 1 wt.%) chlorite-grade metamorphosed black shales. A robust regression of the data yielded a depositional age of 607.8 ± 4.7 Ma (2σ) for the Old Fort Point Formation that was consistent with regional geologic relationships. This study showed that Re-Os systematics remains undisturbed at temperatures of 300 °C to 400 °C and that low abundance Re and Os geochronology is achievable. The ability to extract reliable Re-Os age information from low TOC shale that contained modest amounts Re (< 16 ppb) and Os (< 250 ppt) was directly related to analytical improvements in acid dissolution techniques developed by Selby and Creaser (2003). By examining the effects of non-hydrogenous (i.e. detrital) Re and Os on ORS Re-Os systematics, Selby and Creaser (2003) demonstrated that standard inverse aqua regia digestion liberated more detrital Re and Os than their newly developed CrO_3-H_2SO_4 acid mixture. The

alternative acid digestion technique, adapted from Shen et al. (1996), works by selectively oxidizing organic matter that hosts hydrogenous Re and Os. Selby and Creaser (2003) applied the CrO_3-H_2SO_4 digestion medium to the previously analyzed Exshaw Formation of Creaser et al. (2002) and obtained more precise depositional ages of 366.1 ± 9.6 Ma and 363.4 ± 5.6 Ma (2σ) that agreed within error of the U-Pb monazite age for this formation (363.4 ± 0.4 Ma). Kendal et al. (2006) subsequently applied the CrO_3-H_2SO_4 method to low TOC shales of the Tindelpina Member of the lower Tapley Hill Formation and yielded a precise age of 643.0 ± 2.4 Ma (2σ). Successful application of the CrO_3-H_2SO_4 method to extremely low abundant Re (< 1 ppb) and Os (< 50 ppt) black shales of Neoproterozoic age resulted in a decreased age uncertainty of 7.5% to 1.5% (2σ) relative to the standard inverse aqua regia technique (Rooney et al., 2011).

Re-Os ORS geochronometry has also been shown to remain undisturbed at temperatures of ≈ 650 °C (Rooney et al., 2009). In examining contact metamorphosed (overmature) black shales of the Proterozoic Atar Group proximal to a dolerite sill contact, Rooney et al. (2009) yielded statistically congruent Re-Os age information and Os_I ratios to unmetamorphosed (immature) black shales distal to the contact that otherwise would not have yielded a statistically meaningful correlation had the Re-Os geochronometry been reset in the overmature shales. These preliminary findings suggest that the Re-Os geochronometer remains robust at temperatures comparable to amphibolite grade metamorphism. However, a lack of indicator minerals warrants a more thorough investigation into well-constrained medium- to high-grade metamorphosed black shales.

Disturbance in the Re-Os geochronometer, however, has been observed in shales exposed to hydrothermal fluid of the Wollogorang Formation (Kendal et al., 2009). Re-Os regression of the data yielded a scattered and imprecise age that was statistically younger than a previously obtained U-Pb age from a proximal ash bed. In addition, a highly radiogenic O_I value coupled with paleomagnetic, geochemical, and petrographic data lead Kendal et al. (2009) to conclude that post-depositional remobilization of Re and Os by hydrothermal fluid, petrographically identified by dolomite veinlets, resulted in erroneous Re-Os depositional age information.

Developments in sampling protocol of Kendal et al. (2009) have also lead to improvements in Re-Os geochronology, specifically reproducibility between duplicate analysis of Re and Os concentrations and isotopic ratios. Proper selection of sample aliquot size was shown to influence accuracy and reproducibility between duplicate Re and Os analysis of powder aliquants. For example, it was revealed that variation in Re and Os abundances, ^{187}Re/^{188}Os and ^{187}Os/^{188}Os ratios, and ^{187}Os/^{188}Os$_I$ decreased from > ≈5% to < 5% as aliquot size increased from < 10 g to > 20 g. Kendal et al. (2009) argued that these differences in reproducibility resulted from small-scale diffusion and/or elemental decoupling in < 10g subsamples.

High-precision Re-Os ORS (< 0.5%) geochronometry, where stratigraphic ages are resolvable to single biozones (< 1 Ma intervals), has been a direct outcome of the successive analytical advances over the past two and half decades. Xu et al. (2013), for example, obtained two high-precision Re-Os ORS ages of 237.55 ± 0.95 Ma (± 0.40%; 2σ) and 236.61 ± 0.83 Ma (± 0.35%; 2σ) (decay constant uncertainty included) from Boreal ammonite biozone *Nathorstites* sp. of the Botneheia Formation that agrees within uncertainty of the single-grain U-Pb zircon age of 237.77 ± 0.14 Ma from correlative Tethyan ammonite biozone *Protrachyceras neumayri*. Studies of Georgiev et al. (2011; 2017) and Markey et al. (2016) utilizing unconventional stratigraphic sampling intervals (> 20 cm) report similar high-precision ages of < ± 1% uncertainty. Together these studies illustrate the highest-level of age-precision obtainable utilizing current analytical uncertainties, which is likely to improve in the future as the ^{187}Re decay constant becomes better constrained.

3|Geological History

3.1 Geology of the Gordondale Member

The Gordondale Member is a predominantly organic-rich mudstone unit of the Lower Jurassic Fernie Formation of the Western Canadian Sedimentary Basin (WCSB). Biostratigraphy constrains the deposition of the Gordondale Member to the Early Jurassic, beginning in the Hettangian and concluding in the Early Toarcian (Hall et al., 2000; Asgar-Deen et al., 2003; Asgar-Deen et al., 2004). During this period, the Gordondale Member was deposited in a series of transgressive-regressive episodes off the west coast of the North American Craton in a western interior seaway connected to the Panthalassa Ocean (Riediger, 1990; Poulton et al., 1994). The Gordondale Member purportedly occupied a shallow sloping continental shelf that graded eastward into a transitional mudstone facies of the Red Deer Member, followed by the Nordegg carbonate platform facies (Poulton et al., 1994). Lateral translation of the Quesnellia, Slide Mountain, and Kootenay Terrane across the Panthalassa Ocean towards the west coast of the North American craton is speculated to have lead to the development of a sill-type barrier that restricted water flux into the basin and promoted preferential water column stratification and preservation of large amounts of organic matter (Riediger, 1990; Riediger and Coniglio, 1992). Recently, however, U-Pb detrital zircon data constrained accretion of these exotic terranes onto the North American craton by the Early Pliensbachian, which is hypothesized to have formed a backbulge depozone structured as a foreland basin (Pană et al., 2018a). The development of a high relief, forebulge, structure positioned seaward relative to the marginal, low relief, backbulge depozone may have restricted water flux renewal into the WCSB, and provides an alternative solution for establishing basin anoxia (Pană et al., 2018a). During the early and late stages of sediment deposition (Lower and Upper Radioactive Units), the basin experienced intermittent phases of high rates of marine productivity, resulting in enrichments in bioavailable and redox sensitive trace elements P, Ba, U, Cr, Ni, V, Zn, and Cu (Ross and Bustin, 2006).

At present, the Gordondale Member defines a subsurface stratum that extends laterally from NW to SE across northeastern British Columbia and northwestern Alberta, Canada (Asgar-Deen et al., 2004) (Figure 3.1). Outcrop exposures, however, in the Williston Lake area (Pink Mountain and Black Bear Ridge; Figure 3.1) of NE British Columbia correlate with subsurface lithotypes of the lower Gordondale Member (Asgar-Deen, 2003; Hall et al., 2003; Poulton, 1990). In west-central Alberta the Gordondale Member reaches a maximum thickness of 50 m, which thins westward to a minimum thickness of 19 m in northeastern British Columbia (Asgar-Deen et al., 2003). In west-central Alberta, the Gordondale Member transitions into the Red Deer, which in turn transitions into the Nordegg Member to the S-SE (Figure 3.1; Asgar-Deen et al., 2004). The upper Gordondale contact is conformable with the overlying Toarcian Poker Chip Shale Member, whereas the lower contact is unconformable upon Triassic and Paleozoic strata (Asgar-Deen, 2003).
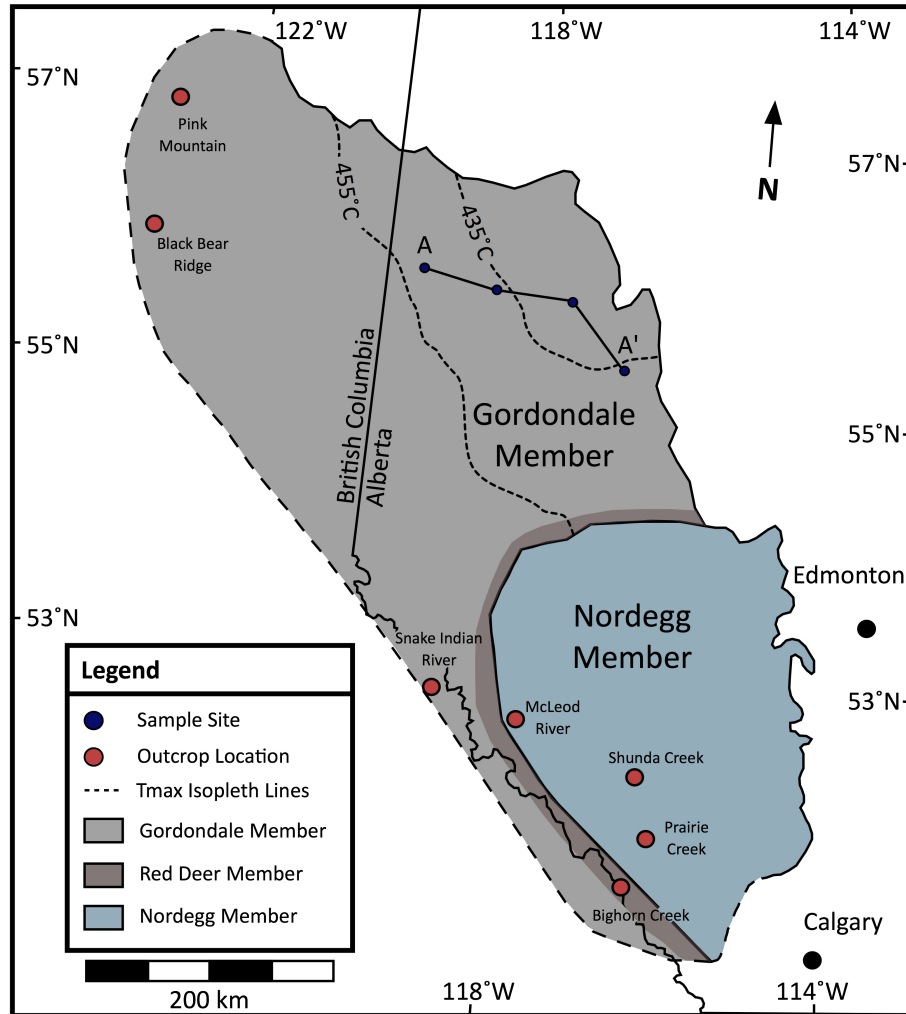
Figure 3.1 Map denoting the geographical extent of the Gordondale, Red Deer, and Nordegg Members across British Columbia and Alberta, Canada (modified after Asgar-Deen et al., 2003 and Riediger et al., 1990). A to A' indicates the spatial relationship between wells Dome Gordondale (UWI = 7-31-79-10W6), PCP Ching (UWI = 6-32-78-5W6), CND Oxy Belloy (UWI = 6-19-78-25W5) and Maclean Creek (UWI = 13-28-73-21W5) sampled for Re-Os ORS geochronology for this study. TMax isopleth lines 435°C to 455°C denote oil generation window. See Figure 10.1 in appendix for Lower Fernie stratigraphy across Alberta.

Riediger (1990) previously divided the Gordondale Member using gamma ray logs into a Lower Radioactive Unit, Middle Silty Unit, and Upper Moderately Radioactive Unit, which are equivalent in nomenclature to Unit 1, Unit 2, and Unit 3 of Asgar-Deen et al. (2003). Asgar-Deen et al. (2003) further subdivided Units 1 and 3 into subunits 1A, 1B, and 1C, and 3A and 3B. Each

of these subunits, however, varies in thickness throughout the WSCB and in some cases subunit occurrences are restricted to specific regions of the WSCB. For example, subunit 1C is only presented in the eastern sections of the Lower Gordondale Member (Range 19W5) (Asgar-Deen et al., 2003). As a result, stratigraphic units and subunits of the Gordondale only relevant to the study area (NW Alberta) are discussed. For a complete and comprehensive description of the Gordondale Member the reader is referred to Asgar-Deen (2003), Asgar-Deen et al. (2003), and Asgar-Deen et al. (2004).

3.1.1 Stratigraphy of the Gordondale Member

The Lower Radioactive Unit is a 8-29 m thick, dark brown to black, finely laminated, organic-rich argillaceous (clay = up to 16 wt.%) to phosphatic calcareous (carbonate = 45 wt.%; francolite = 3-30 wt.%) mudstone unit, with gamma-ray responses exceeding 300 API units, maximum TOC content of 28 wt.%, and minor amounts of syngenetic pyrite (1-2 wt.%) (Asgar-Deen et al., 2004; Riediger et al., 1990; Ross and Bustin, 2006). The Middle Silty Unit is a ~ 2 m thick, light grey to beige silty-calcareous unit, with a gamma-ray response of 75-100 (API), an average TOC content of 2 wt.%, and a predominantly quartz and carbonate (calcite + dolomite) mineralogy (Asgar-Deen et al., 2004; Ross and Bustin, 2006). The Upper Radioactive Unit ranges from 8-25 m thick, grades upwards from an organic-rich calcitic (carbonate = 60 wt.%, clay = 0 wt.%) to argillaceous (carbonate = 5 wt.%, clay = 44 wt.%) mudstone lithology of light to dark brown colour, with a gamma-ray response of 150-250 API, maximum TOC content of 18 wt.%, and contains francolite (3-20 wt.%) and pyrite (1 -2 wt.%) (Riediger et al., 1990; Ross and Bustin, 2006). Macrofossil faunal assemblages observed in the Gordondale Member include: ammonites, pectinoid bivalves (i.e. *Ostrea*, *Oxytoma*, *Ochotochlamys*), belemnoids, and fish debris (Asgar-Deen, 2003; Asgar-Deen et al., 2004; Hall et al., 2000). Common microfossils assemblages include coccolithophores (Asgar-Deen, 2003; Asgar-Deen et al., 2004; Hall et al., 2000) (see Figure 4.3, 4.4, and 4.5 for stratigraphic columns of the Gordondale Member).

3.1.2 Organic Matter of the Gordondale Member

Organic matter in the Gordondale Member constitutes, on average, a TOC content of 8 wt.% (Riediger et al., 1990). Marine algae in the form of liptinite and solid bitumen dominate

the bulk organic matter (Kondla et al., 2017; Riediger et al., 1990; Stasiuk et al., 1988). Lesser amounts of inertinite suggest a small fraction of the organic matter was terrestrially sourced. This is also suggested by the presence of vitrinite. However, vitrinite represents a negligible fraction relative to abundant liptinite and bituminite and minor amount of inertinite and zooclasts (Kondla et al., 2017; Riediger et al., 1990). Rock-eval analyses of Type I/II S-rich kerogen provide supplemental confirmation of a predominantly marine algal biomass (Kondla et al., 2017; Riediger et al., 1990).

4|Methodology

4.1.0 Re and Os Analytical Procedures

Methodology for Re-Os ORS geochronology was performed over four sequential operations: (1) sample collection, (2) mechanical preparation, (3) chemical separation, and (4) data collection and data reduction. The details of each methodological operation will be discussed below.

4.1.1 Sample Collection and Description

Samples for this project were collected on 16 March 2017 from the Alberta Core Research Center located in Calgary, Alberta. Drilling wells selected for Re-Os geochronological sampling included 7-31-79-10W6 and 13-28-73-10W5. During this time, assistance was provided from Dr. Creaser, Dr. Pană, Dr. Poulton, Tyler Hauck, Tiffany Playter, and Hilary Corlett. Samples TS0016-TS0020 and TS0027-TS0031 were gifted from Dr. Creaser, which were previously acquired from the Alberta Core Research Center in the early 2000's. Cores TS0016-TS0020 were sampled from well 6-32-78-5W6, whereas TS0027-TS0031 was sampled from well 6-19-78-25W5. Both cores were cataloged and mechanically processed prior to coming into my possession.

For the duration of the project, a strict sampling protocol was followed to ensure optimal ORS were selected for Re-Os geochronology. This involved obtaining samples that were (1) enriched in Re and Os, (2) collected < 1 m from stratigraphic contacts, (3) collected over < 1 m sedimentary intervals, (4) uniformly black in colour, which is a proxy for organic matter enrichment, and (5) devoid of bioturbation and hydrothermal alteration. In order to ensure samples were enriched in Re and Os a scintillometer was used to measure the U content of the samples, which can be used as a proxy for Re and Os due to similarities in redox behavior. A summary of the cores selected for Re-Os geochronology is shown in Table 1 (see appendix) and

Figure 4.1, whereas their associated stratigraphic columns and depth locations is depicted in Figure 4.3.
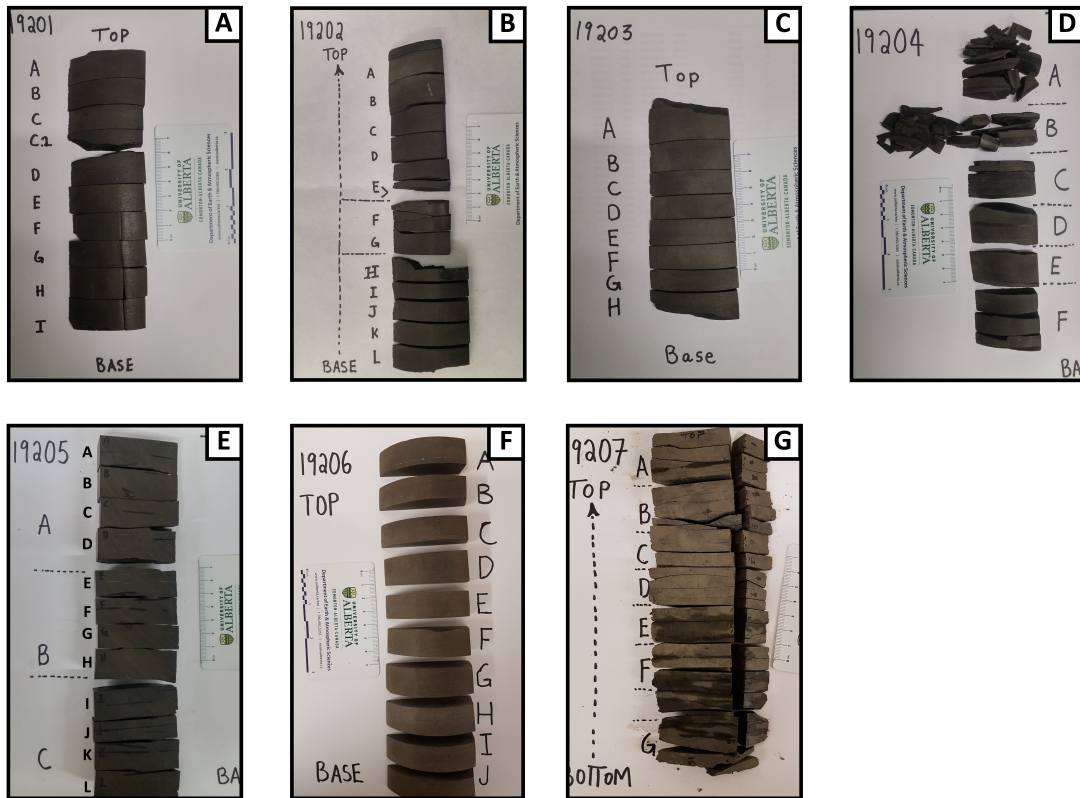
Figure 4.1 Photo A-D corresponds to Dome Gordondale and photo E-G corresponds to CNRL Maclean Creek. Each photo illustrates the post-cut cores prior to rock crushing and powdering. Sample cores were cut into 8 to 12 ~ 2 cm 15-40 g subsections, polished with a disc mill, and alphabetized in ascending order from top to base.

Dome Gordondale (UWI = 7-31-79-10W6)

Dome Gordondale well is defined as the type section of the Gordondale Member (Asgar-Deen et al. 2004). The stratigraphy of the Gordondale Member at this location is approximately 21.3 m thick. The upper Gordondale Member is contiguous with the lower section of the Poker

Chip Member. The Poker Chip-Gordondale contact occurs at a depth of approximately 1537.5 m. The Lower Gordondale Member is adjacent to the Upper Baldonnel Member (Triassic). The Gordondale-Baldonnel contact occurs at a depth of ~ 1558.8 m (Figure 4.4).

Core JT17-19201: JT17-19201 was sampled at a depth interval of 1557.35 m to 1557.54 m from the Lower Radioactive Unit of the Gordondale Member ~ 0.5 m from the Gordondale-Baldonnel (Triassic) contact. Gamma ray response at this depth was 195 API. The lithology of the core is defined as a dark brown/black calcareous mudstone containing small white phosphatic flecks (Figure 4.4).

Core JT17-19202: JT17-19202 was sampled at a depth interval of 1555.82 m to 1556.04 m from the lower Gordondale Member approximately ~ 3 m from the Gordondale-Baldonnel (Triassic) contact. Gamma ray response at his depth was 285 API. The lithology of the core is defined as a dark brown calcareous mudstone (Figure 4.4).

Core JT17-19203: JT17-19203 was sampled at a depth interval of 1537.15 m to 1537.28 m from the basal section of the Poker Chip Member approximately 0.22 m above the Poker Chip-Gordondale contact. Gamma ray response at this depth was 170 API. The lithology of the core is characterized as a dark brown mudstone (Figure 4.4).

Core JT17-19204: JT17-19204 was sampled at a depth interval of 1537.86 m to 1538.11 m from the Upper Gordondale approximately 0.36 m below the Poker Chip-Gordondale contact. Gamma ray response at this depth was 240 API. The lithology of the core is characterized as a dark brown calcareous mudstone. Core 19203 was sampled < 1 m above a partial Late Toarcian ammonite specimen described by Asgar-Deen et al. (2006) as *Yakounia* sp. (Figure 4.2 below and Figure 4.4).

Figure 4.2 Photo depicting a partial ammonite impression described by Asgar-Deen et al. (2006) as *Yakounia* sp. located approximately < 1 m below Core JT17-19203.

CNRL Maclean Creek (UWI = 13-28-73-21W5)

CNRL Maclean Creek contains a complete stratigraphic section of the Gordondale Member that is approximately 25 m thick. The Upper Gordondale Member is adjacent to the basal section of the Poker Chip Member. The Gordondale-Poker Chip contact occurs at a depth of approximately 1169 m. The Lower Gordondale Member is adjacent to an unidentified Triassic stratigraphic unit. The Gordondale-Triassic contact occurs at a depth of approximately 1194 m (Figure 4.5).

Core JT17-19205: JT17-19205 was sampled at a depth interval of 1193.04 m to 1193.28 m from the Lower Gordondale < 1 m above the Gordondale-Triassic contact. Gamma ray response at this depth was 273 API. The lithology of the core is characterized as a dark-brown/black calcareous mudstone with white phosphatic flecks (Figure 4.5).

Core JT17-19206: JT17-19206 was sampled at a depth interval of 1169.38 m to 1169.62 m from the Upper Gordondale < 1 m below the Poker Chip-Gordondale contact. Gamma ray

response at this depth was 260 API. The lithology of the core is characterized as a dark brown calcareous mudstone with white phosphatic flecks (Figure 4.5).

Core JT17-19207: JT17-19207 was sampled at a depth interval of 1168.50 m to 1168.70 m from the Lower Poker Chip member < 1 m above the Poker Chip-Gordondale contact. Gamma ray response at this depth was 220 API. The lithology of the core is characterized as a dark brown mudstone (Figure 4.5).

PCP Ching (UWI = 6-32-78-5W6)

Asgar-Deen et al. (2003) provided a full description of the lithology and biostratigraphy of well PCP Ching of the Gordondale Member. The upper Gordondale is contiguous with the lower Poker Chip Member. The Poker Chip-Gordondale contact occurs at a depth of 1208 m.

Core TS0016-0020: TS0016-TS0020 was sampled at a depth interval of 1221.78 m to 1221.94 m from the upper Gordondale Member approximately 13.78 m below the Poker Chip-Gordondale contact. Gamma ray response at this depth interval ranges from 175-300 API. The lithology of this core is described as a dark grey brown calcitic mudstone (Asgar-Deen et al., 2003). This sampling depth interval is 3.725 m below a lower Toarcian ammonite specimen identified by Asgar-Deen et al. (2003) as *Orthodactylites* sp.

Canadian Oxy Belloy (UWI = 6-19-78-25W5)

Hall et al. (2000) provided a brief description of the lithology and biostratigraphy of the Lower Gordondale Member located in the Canadian Oxy Belloy (6-19-78-25W5) well. The lower Gordondale Member overlies the Lower Triassic Montney Formation at a depth of approximately 1019 m.

Core TS0027-TS0031: TS0027-TS0031 was sampled at a depth interval of 1217.92 m to 1218.57 m from the lower Gordondale Member approximately 0.5 m from the Gordondale-Montney contact. The lithology of this core is described as a dark grey calcitic mudstone. The sampling depth transects the Late Hettangian ammonite specimen identified by Hall et al.

(2000) as *Discamphiceras* cf. *silberlingi*. Hall et al. (2000) also identified coccolith specimens with assigned Hettangian to Sinemurian ages.
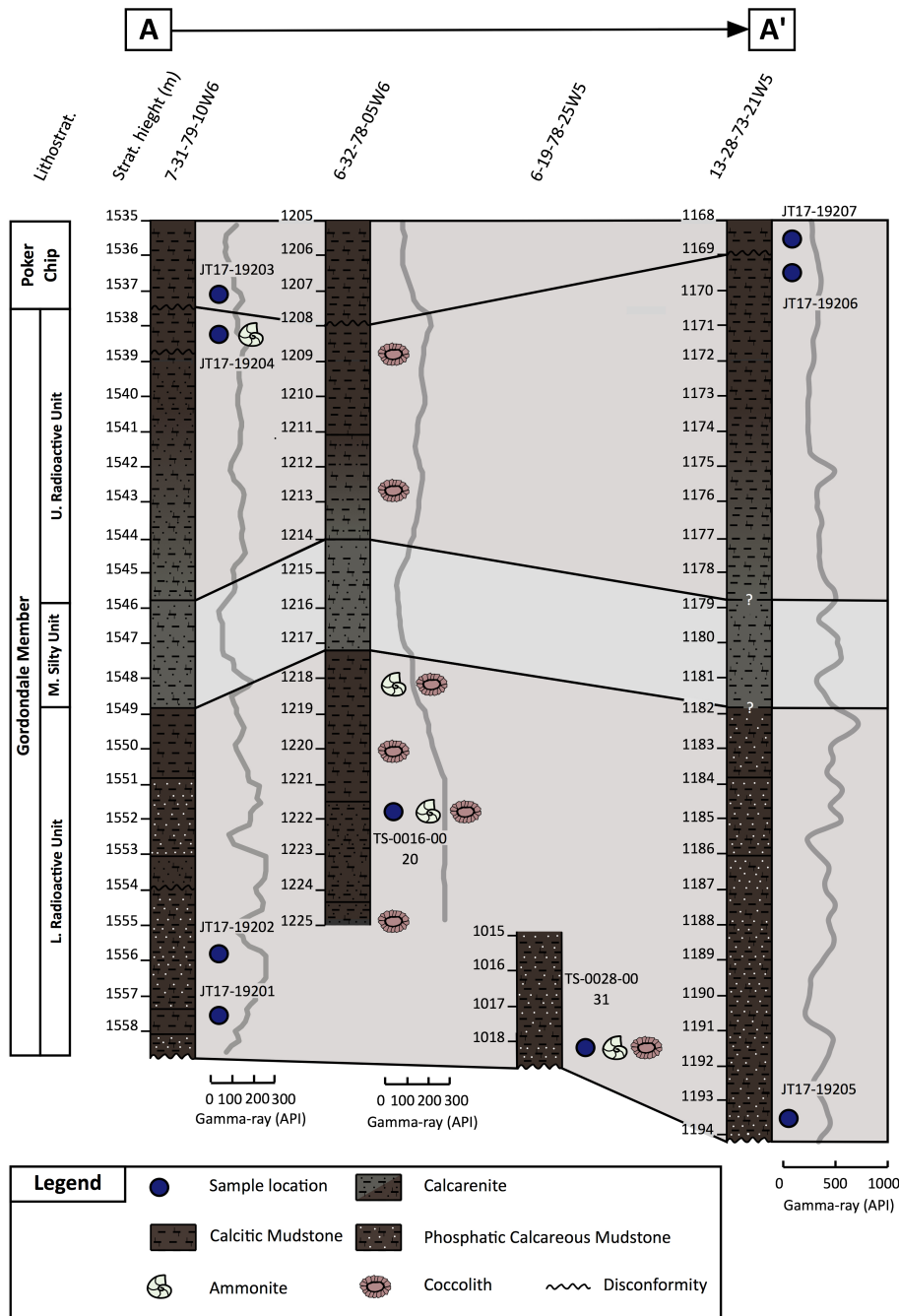
Figure 4.3 Stratigraphic columns of the Gordondale Member for wells Dome Gordondale (UWI = 7-31-79-10W6), PCP Ching (UWI = 6-32-78-05W6), CND Oxy Belloy (UWI = 6-19-78-25W5), and Maclean Creek (UWI = 13-28-73-21W5) (A-A'). For spatial context for each well across A-A' transect refer to Figure 3.0. Vertical Exaggeration (VE) = 9x. Refer to Asgar-Deen et al. (2003,

2004) for more detailed stratigraphic columns of wells Dome Gordondale and PCP Ching. Maclean Creek stratigraphy is inferred from stratigraphic descriptions of the Lower Radioactive Unity, Middle Silty Unit, and Upper Radioactive Unit by Asgar-Deen (2003) and Asgar-Deen et al. (2003/2004), therefore the upper and lower contacts of the Middle Silty Unit are inferred from gamma-ray (API) log readings. Gamma-ray logs for CND Oxy Belloy have not been digitized, and therefore are not reported here.
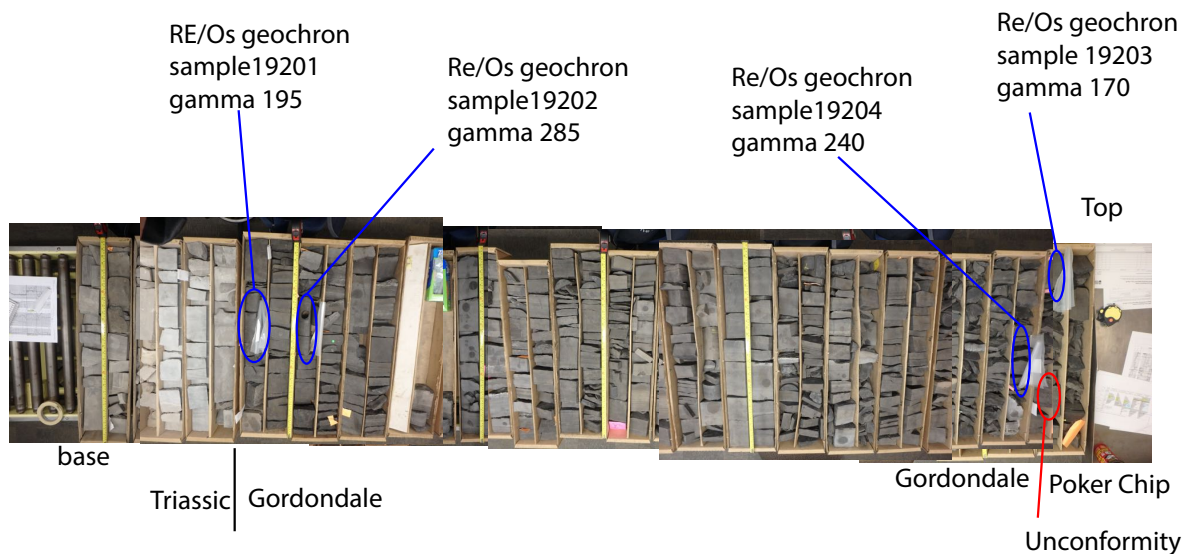
7-31-79-10W6

Figure 4.4 Re-Os ORS geochronology sampling intervals for Dome Gordondale well (UWI = 7-31-79-10W6).

13-28-73-21w5
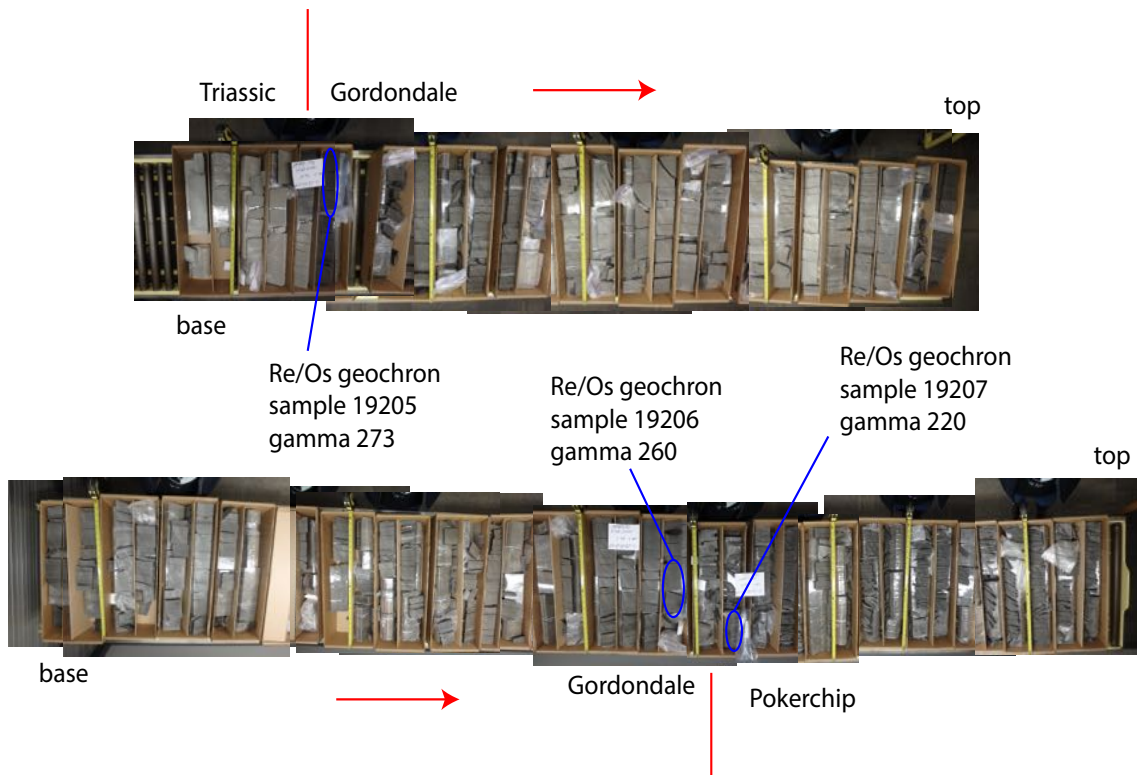
Figure 4. 5 Re-Os ORS geochronology sampling intervals for Maclean Creek well (UWI = 13-28-73-21W5).

4.1.2 Physical Separation

Whole rock cores JT17-19201 to JT17-19207 were mechanically prepared from March 2017 to September 2017 in the Rock Crushing and Mineral Separation Laboratory at the University of Alberta's Head House facility. Each core was cut longitudinally into 2/3 and 1/3 pieces using a rock saw. The former piece was processed for Re-Os geochronology, whereas the latter was cataloged and archived. A subsection sampling strategy of > 10 g aliquots were adopted to minimize the effects of possible small-scale Re and Os diffusion (Kendal et al., 2009). As a result, each core processed for Re-Os geochronology was cut laterally into 8 to 10 ~ 2 cm

15-50 g aliquant subsections. Subsections were alphabetized from top to base and inspected for any unnatural fractures, which were removed using a rock saw. Subsections were subsequently polished via disc mill to remove any metal contaminants derived from drill core and rock saw marks. Samples were rinsed with water to remove any extraneous grit, clay, and dirt prior to rock crushing and powdering.

Subsection samples were pre-screened for hydrothermal features, such as cross-cutting quartz veins, prior to rock crushing and powdering. This first-order measure helped to eliminate sub-optimal samples from being processed that may have experienced post-depositional disturbance of Re-Os systematics. After selecting optimal subsections, whole rock samples were manually crushed into rock fragments using a steel hammer and anvil. Prudent measures of taping the metal surfaces of the hammer and anvil with DUCT tape were employed to ensure no metal contact came between sample and hammer/anvil. As an additional measure of precaution, subsections were wrapped in two plastic bags, while the steel hammer was wrapped in a single plastic bag and plastic bag was tapped over the surface of the anvil. Both hammer and anvil were pre-cleaned with ethanol between each subsample and used plastic bags were discard and replaced with new ones. As a final measure of precaution, a magnet was scanned across the rock chips to remove any metal that may have penetrated through the plastic bag and into the sample during manual crushing.

Following manual crushing, subsample rock chips were placed in an automated agate mill. Rock chips were pulverized to fine powder for approximately 10 minutes per sample. Sample powder was then transferred from the agate mill to a clean glass vial that was labeled with its corresponding sample name. Between each sample, the agate mill was cleaned with ethanol and paper towels. Post-powdered sample aliquots weighed from ~15 g to ~50 g. The pre- and post-crushed sample weights were compared to attempt to quantify the amount of sample lost during manual and automated sample crushing (Figure 4.6). The amount of sample lost was largely correlated with the tenacity of the specimen. Therefore, low tensile strength, friable, mudstones tended to have less sample loss, whereas high tensile strength mudstones tended to have large sample loss. Either way, a sample loss of < 2 grams was unavoidable.
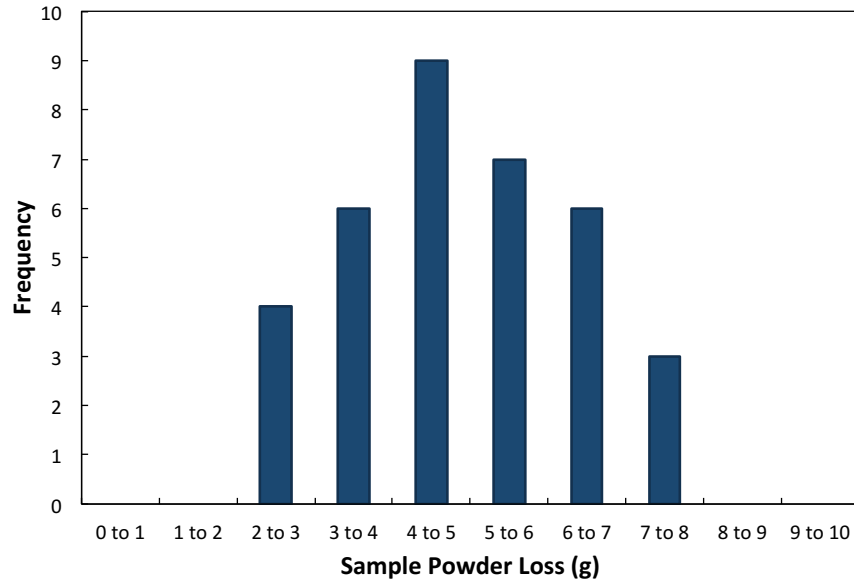
Figure 4. 6 Frequency distribution plot of sample loss in grams post-manual and -automated sample crushing. Post-crushed sample loss forms a normal Gaussian distribution. The minimum, average, and maximum loss of sample is between 2 and 3, 4 and 5, and 7 and 8 grams.

4.1.3 Chemical Separation

Whole rock powders were chemically separated from January 2017 to December 2017 in the Crustal Re-Os Geochronology Laboratory located at the University of Alberta. This lab is designated as a ISO Class 5 (M3.5) cleanroom. Designated Re and Os laminar flow workstations, however, operate as ISO Class 4 (M2.5) enclosures. A full procedural chemical separation involves six operations: (1) sample digestion, (2) Os solvent extraction, (3) Os drydown, (4) Re solvent extraction, (5) Os microdistillation, and (6) Re chromatography. Each phase of chemical separation will be discussed in detail below. A summary of the chemical separation workflow can be found in Figure 4.7. After a complete procedural separation, Re and Os will have been purified into separates ready for N-TIMS isotopic analysis.

4.1.3.1 Sample Dissolution

Whole rock powder aliquots of approximately 100 mg and a known amount of mixed ^{185}Re-^{190}Os mixed spike solution were digested via 8 mL of CrO_3-H_2SO_4 (1:1 ratio of 4 N H_2SO_4 and 4 N CrO_3-H_2SO_4 [0.5 g CrO_3 per 1 mL of 4 N H_2SO_4) oxidizing media in clean/sealed 25 mL thick-walled borosilicate glass Carius tubes in a convection oven at 240°C for 72 hours. This procedure involved the sequential transfer of H_2SO_4 (reducing media) followed by CrO_3-H_2SO_4 (oxidizing media) into an open-vessel Carius tube that were flash frozen at -72 °C via dry ice-ethanol bath. Transferring and freezing the former first allowed a barrier to form between the sample and the oxidizing media, which minimized oxidation of reduced Re and Os species prior to Carius tube sealing via blowtorch. Once sealed, thawed sample Carius tubes were agitated by vortex for 1 ½ minutes to allow full acid-sample contact, and then placed in the oven for thermal-acid digestion.

4.1.3.2 Os Solvent Extraction

Osmium solvent extraction was employed to (1) separate (gas above 39°C, likely mixed phase at 25°C) OsO_4 from aqueous ReO_4^- and (2) back-reduce OsO_4 to aqueous $OsBr_6^{2-}$. The former was performed by exploiting the strong partitioning behaviour of OsO_4 into $CHCl_3$, whereas the latter was performed by exploiting the strong reducing behaviour of 9 N HBr to reduce volatile Os(VIII) to aqueous Os(IV). Carius tubes containing post-digested samples were flash frozen via dry ice-ethanol bath, which condenses $OsO_4(g)$ to $OsO_4(s)$, and opened using a blowtorch. A 3.5 mL aliquot of chloroform was immediately transferred into the sample vessel. Once thawed, the chloroform-acid-sample mixture was transferred to a clean 50 mL centrifuge tube, which was capped, shaken for 1 minute, and centrifuged for 1 ½ minutes. The immiscible chloroform fraction was decanted to a clean 22 mL glass vial containing 3 mL of 9 N HBr. The chloroform extraction step was repeated two more times, and CrO_3-H_2SO_4 acid mixture, containing ReO_4^-, was transferred to a clean 15 mL centrifuge tube. The 22 mL glass vial

containing a mixture of 9.5 mL of chloroform and 3 mL of 9 N HBr was placed on a vortex mixer overnight.

4.1.3.3 Re Solvent Extraction

Rhenium solvent extraction is an intermediary purification step that utilizes acetone and concentrated NaOH to separate Re from Cr. Chromium suppresses ionization of Re during mass spectrometric analysis, and therefore should not be present during the final purification phase. A 2 mL aliquot of the CrO_3-H_2SO_4 sample solution containing ReO_4^- is transferred to a clean 50 mL centrifuge tube. A ~7 mL aliquot of ~ 17 N NaOH is transferred to an empty/clean 50 mL centrifuge tube. Equal parts acetone is added to the 50 mL centrifuge tube containing the NaOH. The mixture is shaken vigorously for 3 minutes and then centrifuged for 3 minutes. The acetone acts to strip any Re contaminants in the trace metal grade NaOH (Li et al. 2009). The dirty acetone is discarded to waste and the cleaned NaOH is then added to the 50 mL centrifuge containing the sample, and left to sit for half an hour. After this, 7.5 mL of clean acetone is added to the NaOH-sample mixture and is shaken vigorously for 3 minutes and then centrifuged for 3 minutes. The acetone is then transferred to a clean 22 mL glass vial. A second 7.5 mL aliquot of clean acetone is added to the sample 50 mL centrifuge tube, shaken for 3 minutes, centrifuged for 3 minutes, and transferred to the 22 mL glass vial. The 22 mL glass vial containing the Re-acetone mixture is placed on a hot plate to dry down.

4.1.3.4 Os Drydown

Os drydown is the precursor and preparatory step in purifying Os by microdistillation (Birck et al., 1997). The procedure involves separating chloroform from 9 N HBr by decanting chloroform to waste and transferring 9 N HBr via pipette to a watch glass coated in pre-cleaned Teflon tape. The 9 N HBr is subsequently evaporated on a hotplate at 80°C until < 0.1 mL remains, which is then transferred by pipette to a clean Teflon cap and dried down. The Teflon

cap containing the sample residue is sealed to its corresponding Teflon vial and stored for later use.

4.1.3.5 Os Micrcodistillation

Osmium microdistillation is the final purification step in chemically processing Os. By oxidizing Os(IV) to Os(VIII) via 4 N CrO_3-H_2SO_4 (0.08 g CrO_3/1 mL 12 N H_2SO_4) and then back reducing Os(VIII) to Os(IV) via 9 N HBr, residual organics can be separated from Os, which would otherwise suppress ionization of Os during mass spectrometric analysis. The procedure involved doping the sample residue attached to the Teflon cap with 30 µL of 4 N CrO_3-H_2SO_4 and transferring 20 µL of 9 N HBr to the center of the corresponding Teflon vial. The Teflon vial is inverted, shaken to ensure the 9 N HBr remains held by surface tension, and sealed to the Teflon cap and placed on a hotplate for 3 hours at 73°C. During the microdistillation, any reduced Os(IV) is oxidized by 4 N CrO_3-H_2SO_4 to OsO_4 and then back reduced from OsO_4 to $OsBr_6^{2-}$ by 9 N HBr.

4.1.3.6 Re Chromatography

Post-Re solvent extraction residues are dissolved in 1 mL of 0.2 N HNO_3 for approximately two hours. Anion exchange columns are prepared with EICHROM 1 X 8 100-200 mesh-size anion exchange resin, cleaned with 4 mL of 6 N HNO_3, and equilibrated with 4 mL of 0.2 N HNO_3. The loading solution is then transferred by pipette into to the column and eluted. This is followed by a four step sequential wash phase: 1 mL of 0.2 N HNO_3, 2 mL 0.2 N HNO_3, 2 mL of 0.2 N HCl, and 2 mL of 6 N HNO_3. Anion exchange chromatography finishes with collection of 4 mL of 6 N HNO_3 in a pre-cleaned PMP beaker. After collection, the purified Re solution is dried down at 80°C overnight.
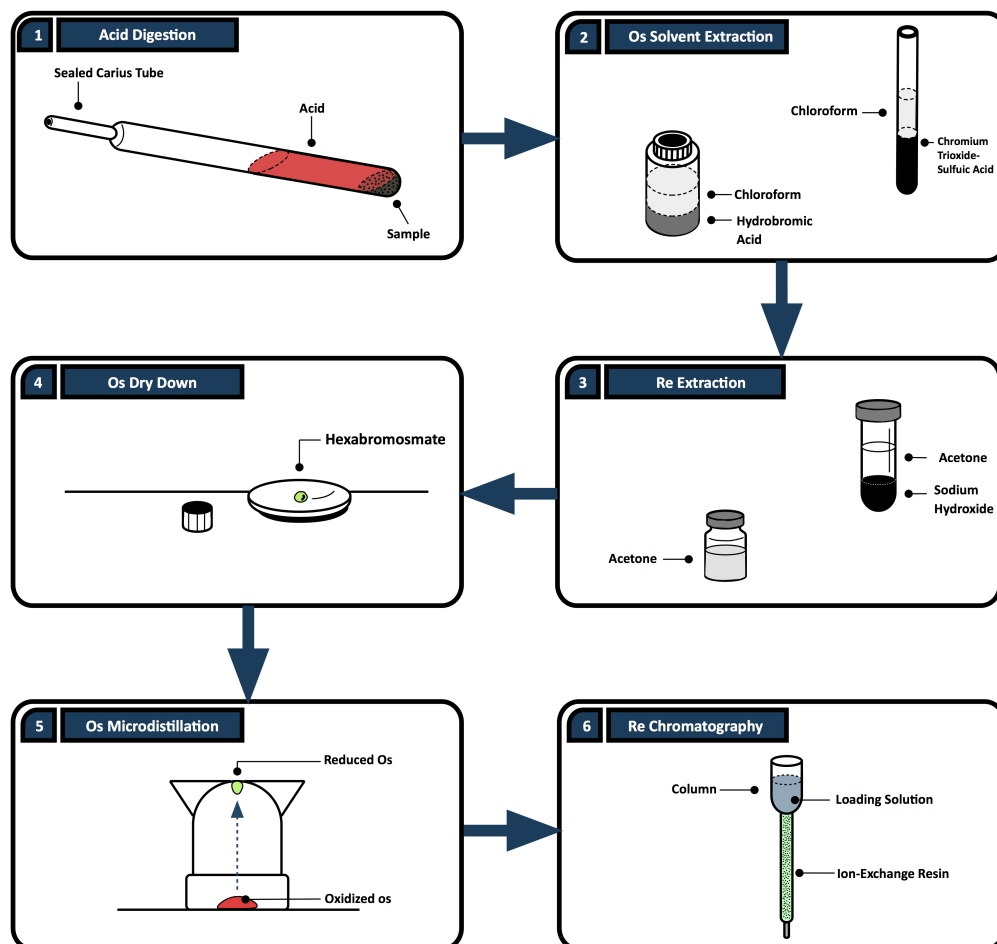
Figure 4. 7 Diagram illustrating the chemical separation workflow for isolating and purifying Re and Os.

4.1.4 Re and Os Isotopic Analysis

Aliquots of ~10-20 ng of Re and ~50-100 pg of Os separates were loaded onto Ni and Pt filaments, respectively, and coated with $Ba(NO_3)_2$ and $Ba(OH)_2$ salts. Rhenium and osmium isotopic measurements were performed on a Negative-Thermal Ionization Mass Spectrometer (N-TIMS) under a 5×10^{-8} to 7×10^{-8} tor vacuum conditions. Rhenium and osmium ion beams were detected using electron multiplier and Faraday Cups in static and peak-hopping mode. Rhenium was run over a series of 4 blocks of 25 cycles, whereas osmium was run over 6 blocks

of 16 cycles. In the case of Os, oxygen was bled into the ion source to enhance ionization to OsO_3^-. Stable Re and Os ion beams were achieved in the temperature ranges of 750-820 °C and 650-710 °C, yielding, on average, a 600 mV and 200 Kcps signal. In-house laboratory standards were run on a routine basis to monitor instrumental performance. The oxide $^{185}ReO_3^-$ was monitored for isobaric interferences of $^{185}Re^{16}O_2^{18}O_1^-$ with $^{187}Os^{16}O_3^-$, whereby intensities of $^{185}ReO_3^-$ were kept below 10 cps. Post-data reduction included isobaric oxide corrections, mass fractionation corrections, and spike-sample unmixing (isotope dilution). Rhenium and Osmium procedural blanks were performed routinely and are reported in Table 2 (see appendix). Average Re and Os blank concentrations were 0.0108 ppb and 0.127 ppt average $^{187}Re/^{188}Os$ and $^{187}Os/^{188}Os$ ratios were 935.47 and 0.293. Figure 4.8 details a timeline of Re and Os blanks concentrations throughout the duration of the project.
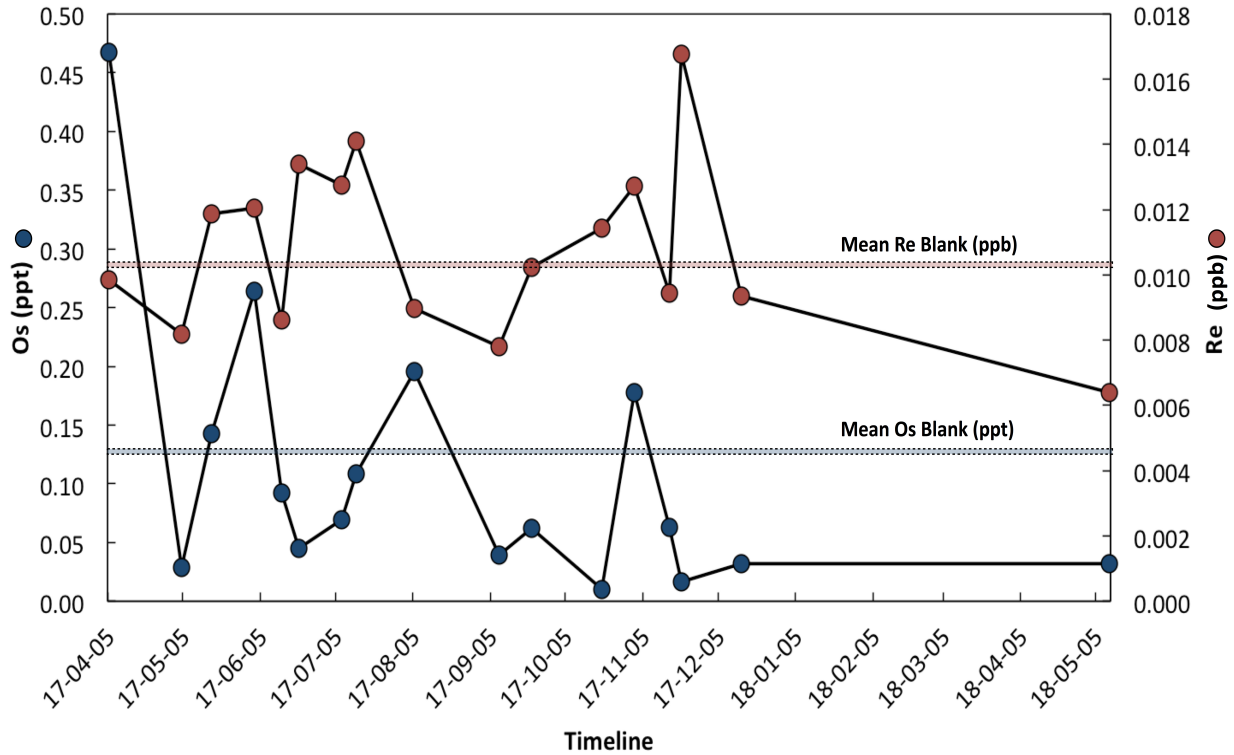
Figure 4. 8 Timeline of Re and Os procedural blanks through the duration of the project. Red and blue lines correspond to mean Re (ppb) and Os (ppt) blanks.

4.2.1 Sr Isotope Analysis

4.2.2 Geochemical Pre-screening

Samples were geochemically pre-screened for high Sr, low Rb, low Mn/Sr ratios, which are purported indicators of primary seawater (Kaufman and Knoll, 1995). Approximately 200 mg shale powder aliquots were dissolved in 20 mL of 6 N HCl for 24 hours. Supernatant was separated from sample residue and dried overnight at 80°C, which was subsequently dissolved in 10 mL of 6 N HNO_3 the following day. The sample solutions were sent for geochemical analysis by ICP-MS at the University of Alberta.

4.2.3. Acetic Acid Leach

The strontium leaching method employed was adapted from Li et al. (2012) and was performed over a series of three leaching phases. Approximately 200 mg of shale power aliquots were weighed using an analytical balance and transferred to clean 22-mL glass vials, followed by immersion in an equivalent volume of dilute (0.035 N) acetic acid to dissolve ~15% (leach 1), ~15% (leach 2), and ~35-40% (leach 3) of calcite. Each leaching phase consisted of: (1) 5 minutes of sonication, (2) agitation by vortex overnight, (3) transfer of supernatant by filtration to new 22-mL glass vial, and (4) drydown of supernatant on hotplate at 80°C. In order to quantify the amount of calcite dissolved between each phase of leaching a second replicate batch of Sr samples were processed with a slight modification to the leaching procedure. This modification was performed between steps (3) and (4) and involved desiccation of sample residues by hot plate at 80°C overnight, and subsequent weighing of sample residues.

4.2.4 Chemical Separation and Isotopic Analysis

Separation of Sr from base cations was performed by cation exchange chromatography. This involved the transfer 200-µL 0.75 N distilled HCl supernatants onto 0.75 N HCl equilibrated cation exchange columns, followed by a three-phase elution scheme: (1) rinse, (2) wash, and (3) collect. The rinse phase involved the sequential transfer of: (1) 0.5-mL of 0.75 distilled HCl (2X), (2) 1-mL of oxalic-HCl acid mixture (2X), (3) 1.5-mL of 2.5 N distilled HCl (2X), which was followed by washing of 8-mL of 2.5 N distilled HCl (2X), and then finally collection of 6-mL of 2.5 N distilled HCl. Following collection, sample separates were dried down at 80°C on a hot plate, and then analyzed by MC-ICP-MS at the University of Alberta. All Sr isotope ratios are normalized to a value of 0.710245 for the NIST SRM987 Sr standard

4.3.1 Chemical Separation and Analysis of Kerogen C Isotopes

4.3.2 Kerogen Extraction, Digestion, and Analysis

The kerogen (insoluble organic residue) of ~ 1 g shale (whole rock) powder aliquots was isolated for their organic carbon isotopes at the University of Alberta's Stable Isotope Laboratory. To ensure a pure kerogen extraction, samples were decarbonated via a treatment in 6 N HCl for 12 hours. Sample vials were centrifuged for 4 minutes and the supernatant was discarded to waste, and the remaining residues were desiccated in an oven at 65°C overnight. Two to three 20 mL carbon tetrachloride (CCl_4) solvent extractions were performed on sample residues to remove any low molecular weight (soluble) hydrocarbons. Between each solvent extraction, samples were centrifuged for 4 minutes and supernatant was discarded to waste. Following complete removal of soluble hydrocarbons, sample residues were rinsed three times with deionized water, and then desiccated in an oven at 65°C overnight.

Kerogen residue extracts of ~40-100 mg were wrapped in copper foil, and transferred into a quartz glass tube. Cupric oxide powder (~1000 mg) along with approximately half a centimeter long silver (Ag) wire was added to the quartz glass vessel. To remove any build up of cupric oxide power along the neck of the quartz glass tube a small piece of quartz wool was inserted into the tube to remove any built up powder. The quartz glass tube was degassed for approximately 8 hours using a conventional high-vacuum gas separation apparatus, and then sealed with a blowtorch. This was followed by placing the sealed quartz glass tube into an oven for ~8 hours at 800°C. Once the allotted time was reached and the reaction complete, the quartz glass tube was removed from the oven. The sealed glass tube was then cooled with liquid nitrogen, scored, and inserted into a glass breaker. The glass breaker was then placed into a vacuum-sealed glass apparatus while the bottom of the quartz glass tube remained immersed in liquid nitrogen. The seal on the glass tube was then broken, and any nitrogen present in the quartz sample tube was pumped down to allow the non-condensable gases to be removed. The liquid nitrogen was swapped for a dry ice ethanol-slurry mixture. Finally, the carbon dioxide was isolated into a glass vial. The kerogen carbon isotopes were measured using

a dual-inlet mass spectrometer, and are reported in delta notation (δ) in permil (‰) and are referenced to geologic standard VPDB.

5 | Re-Os Age Constraints of the Sinemurian-Pliensbachian boundary

5.1 Introduction

A major evolutionary step in ammonite and coccolith diversification and radiation corresponds with the Sinemurian/Pliensbachian boundary (Dommergues et al., 2000). This marked the first occurrence of *Bifericeras donovani* of the Eoderoceratidae ammonite family and *Similiscutum cruciulus* of the placoloth coccolith morphologies (Ogg et al., 2012; Thierstein and Young, 2004). Incipient rifting of Pangaea at the time resulted in the formation of the Hispanic Corridor – a proto-Atlantic seaway - that amplified faunal radiation by providing a marine connection between Western Tethys and the South American Pacific coast (Plancq et al., 2016; Venturi et al., 2006) (see Figure 5.1). This unique event permitted faunal exchange of ammonites, coccoliths, brachiopod, bivalves, and reptiles between the Tethys and paleo-Pacific oceans (Venturi et al., 2006). Warm, temperate climatic conditions triggered widespread microalgal blooms that increased marine biomass (Riding et al., 2012; Van de Schootbrugge et al., 2005). Meanwhile, marine transgressions inundated paleo-coastlines with shallow epeiric (inland) seas creating hotspots of anoxia that lead to a peripheral spread of organic-rich facies in Tethyan, Boreal, and western Pacific realms (Duarte et al., 2010; Gómez et al., 2016). Organic-rich facies located in Lusitanian (Portugal), Basque-Cantabrian (Spain) and Bristol Channel and Wessex (England) basins accumulated upwards of 20 wt.% organic matter (TOC). These prominent hydrocarbon source rocks record a 2 ‰ negative carbon isotope excursion that extends across the *Echioceras raricostatum* and *Uptonia jamesoni* ammonite zones of the Sinemurian/Pliensbachian boundary (Gómez et al., 2016). This globally pervasive perturbation in the carbon cycle was purportedly linked to dissociation of methane clathrates and/or thermogenically-sourced methane (Gradstein, 2012). Seawater $^{87}Sr/^{86}Sr$ followed a continued downward trend from the end-Triassic event, while seawater $^{187}Os/^{188}Os$ experienced a

transient lull from the mantle-like signatures recorded in the Tethyan realm that otherwise reflected an increased hydrothermal flux related to the continued expansion of the Proto-Atlantic rift system and re-establishment towards the radiogenic background signal of the Early Jurassic (Gradstein, 2012; Porter et al., 2013).

To date, the S-P boundary lacks direct radiometric age constraints. This is an important fact since reconstructing the Early Jurassic stratigraphic record begins by building a temporal framework around which geologic events can be accurately correlated, including events that transpired at the S-P boundary. According to the Geologic Time Scale 2012, the age projected for Sinemurian-Pliensbachian boundary is 190.9 ± 1.0 Ma (Gradstein, 2012). The numerical age assigned to the S-P boundary is extrapolated from linear trends in $^{87}Sr/^{86}Sr_i$ ratios of contemporaneous seawater calibrated to radiometric tie points of the base Sinemurian and Toarcian stages (Ogg et al., 2012). The S-P boundary age, however, has shifted in accord with recent age refinements for the base Sinemurian and Toarcian stages. The newly projected age for the S-P boundary is 191.4 ± 1 Ma (Ogg et al., 2016). However, recently, Ruhl et al. (2016) have proposed a slightly older S-P boundary age of 192.4 ± 0.4 Ma. Despite these S-P boundary estimates, one problem inherent with interpolated chronostratigraphic and astronomical ages is their reliance on more assumptions than radioisotopic dating, which therefore necessitates more biostratigraphic and chemostratigraphic evidence to justify their geological significance. By employing Re-Os ORS geochronometry to wells Dome Gordondale, CND Oxy Belloy, and Maclean Creek of subunit 1A of the Radioactive Unit of the Gordondale Member, we aim to (1) overcome the inherent problems of interpolated ages and (2) fill any current chronostratigraphic gaps of the S-P boundary section.

Early Jurassic: 191 Ma
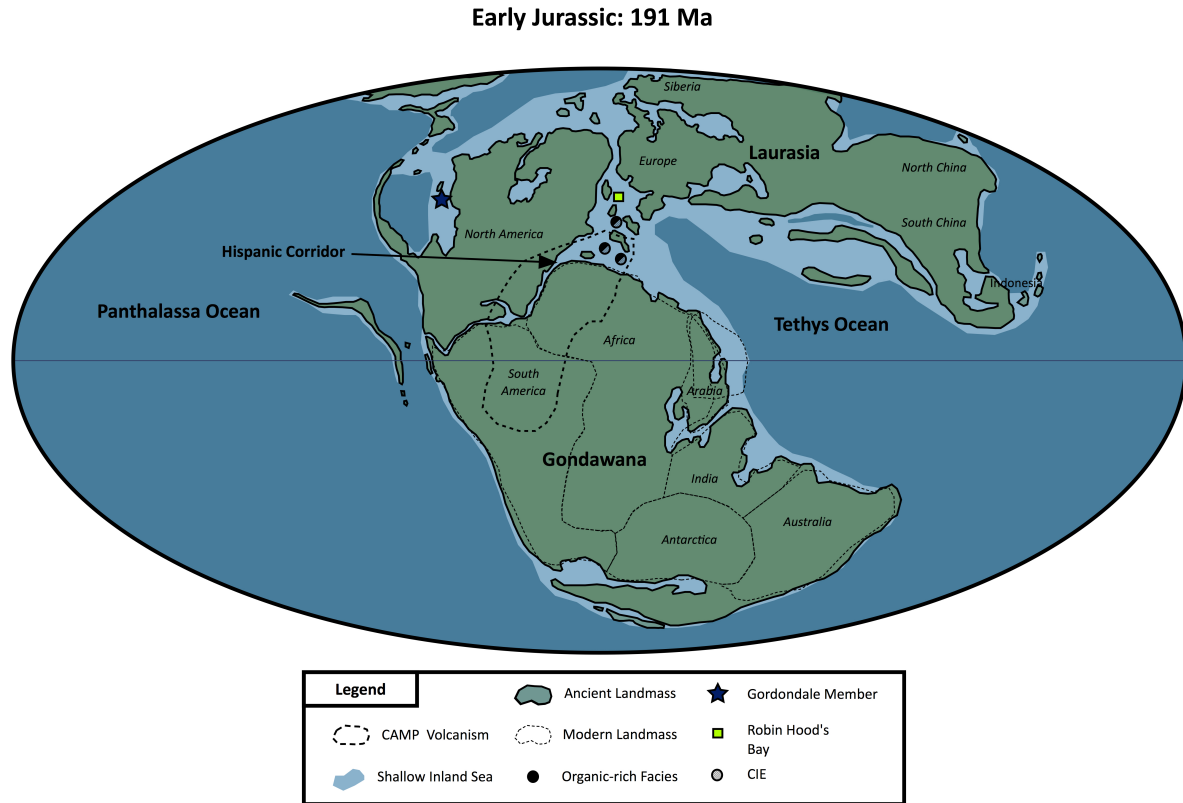
Figure 5.1 Paleogeographical reconstruction of the Early Jurassic Sinemurian-Pliensbachian boundary event (modified after Scotese, 2014).

5.2 Geological background

5.2.1 Lower Gordondale Member (Lower Radioactive Unit, Subunit 1A)

The Lower Radioactive Unit is divided into two successive subunits, 1A and 1B, in NW Alberta. Asgar-Deen et al. (2003) characterized subunit 1A as a variably thick, dark grey to brown organic-rich calcitic mudstone, unconformably overlying Triassic strata. Macrofossils observed in this succession include: ammonites, pectinoid bivalves, *Ostrea*, shell fragments, belemnoids, and fish fragments (Asgar-Deen et al., 2003).

5.2.2 Biostratigraphy of Subunit 1A

Hall et al. (2000) identified Hettangian ammonite specimen *Discamphiceras* cf. *silberlingi* (1018.15 m) in subunit 1A (CND Oxy Belloy; UWI = 6-19-78-25W5) of the Lower Radioactive Unit of the Gordondale. Occurrences of *D. silberlingi* have been observed in Nevada, Alaska and British Columbia, which correlates indirectly with international standard ammonite zone *Alsatites liasicus* in NW Europe through the co-occurrence with *A. liasicus* species in North American ammonite zone *Franziceras* sp. (Hall and Pitaru, 2003; Longridge et al., 2008; Pálfy et al., 1999). Asgar-Deen et al. (2003) subsequently identified two other ammonite specimens in subunit 1A of the basal Gordondale (UWI = 12-4-73-2W6) that resembles Hettangian *A. liasicus* and a lateral impression that resembles *Caloceras* sp. Lower Gordondale outcrop exposures in NE British Columbia of the Williston Lake region (Figure 4.1: Black Bear Ridge) contain Hettangian ammonite species *A. liasicus* that correlates with the subsurface Hettangian ammonite specimens of the Lower Gordondale (Asgar-Deen et al., 2003; Hall and Pitaru 2003; Hall et al., 2000). Outcrop exposes of the Lower Gordondale Member in Pine River, Pine Pass map area north of Williston Lake in NE British Columbia contain Early Hettangian and Early Pliensbachian ammonite specimens *Psiloceras* sp. and *Prodactylioceras* sp. (Frebold, 1970; Poulton et al., 1990). The former correlates with Tethyan and Boreal ammonite zone *Psiloceras planorbis*, whereas the latter correlates with *Prodactylioceras davoei* (Frebold, 1970; Ogg et al., 2016).

Hall et al. (2000) observed well preserved rare to frequent coccolithophores *Crepidolithus crassus*, *Crucirhabdus primulus*, *Tubirhabdus patulus*, *Mitrolithus elegans*, *?Mitrolithus jansae*, and *Parhabdolithus liasicus* alongside ammonite specimen *D. silberlingi*. Of these, *Tubirhabdus patulus*, *Mitrolithus elegans*, and *Parhabdolithus liasicus* are common in their occurrence. Collectively, coccolith biochrons of subunit 1A bracket the depositional age of the Lower Radioactive Unit of the Gordondale between Upper Hettangian and Lower Sinemurian stages (Hall et al., 2000). These are equivalent to NW European ammonite zones A. *liasicus* to *Hyperlioceras discites* (Mattioli and Erba, 1999; Pálfy et al., 2000).

5.3 Methods

A detailed description of Re-Os methodology can be found in section 3.2 to 3.5. To briefly summarize, sample powder aliquots of cores JT17-19201, JT17-1902, JT17-19205, and TS0027 to TS0031 and a known amount of mixed ^{185}Re-^{190}Os mixed spike were digested in a convection oven at 240°C for 72 hours via coupling CrO_3-H_2SO_4 (8 mL) dissolution procedure of Selby and Creaser (2003) with the Carius tube method of Shirey and Walker (1995). Rhenium and osmium fractions were subsequently separated via Os solvent extraction and Re solvent extraction modified after Selby and Creaser (2003), and then purified by Os microdistillation and Re anion exchange chromatography modified after Birck et al. (1997) and subsequently analyzed using ID-N-TIMS.

5.4 Results

5.4.1 Re and Os Concentrations and Isotopic Ratios

Rhenium and Os concentrations and isotopic ratios are listed in Table 3 (see appendix). Rhenium and Os concentrations for subunit 1 (Lower Gordondale) range from 30-560 ppb and 320-5700 ppt, with ^{187}Re/^{188}Os and ^{187}Os/^{188}Os ratios range from 390-1540 and 1.6-6.4. Replicate analysis yielded a reproducibility of < ± 1%. Samples from JT17-19202 show the highest Re and Os concentrations, followed by TS-0027-0031, JT17-19205, and JT17-19201. The same pattern, however, is not reproduced in the Re and Os isotopic ratios for each core. For instance, TS-0027-0031 exhibits the highest Re and Os isotopic ratios, followed by JT17-19205, JT17-19202, and JT17-19201. Therefore, no apparent correlation exists between Re and Os concentration and Re/Os fractionation. The Re and Os concentrations and isotopic ratios of the entire Lower Gordondale suite, however, are enriched relative to present-day UCC values and contemporaneous Early Jurassic ORS (Dubin and Peucker-Ehrenbrink, 2015; Porter et al., 2013; Porter et al., 2014).

5.4.2 Re-Os Geochronology

Rhenium-Osmium isochron plots generated by the Microsoft add-in program *Isoplot* (Ludwig, 2012) are presented in Figure 5.2. Linear regression of data from TS-0027-0031 (n = 5) yielded a Modal 1 age of 191.18 ± 0.94 Ma (2σ; Mean Squared Weighted Deviates (MSWD) = 0.52 and $^{187}Os/^{188}Os_i$ of 0.522 ± 0.017 (2σ)). Core JT17-19205 (n = 5) yields a Model 1 age of 192.0 ± 1.4 Ma (2σ; MSWD = 1.3) and $^{187}Os/^{188}Os_i$ of 0.494 ± 0.02 (2σ) that is statistically equivalent to the Re-Os age and $^{187}Os/^{188}Os_i$ ratio obtained from core TS-0027-0031. In contrast, Re-Os isochron regression of data from JT17-19201 (n =5) yields a Model 3 age of 53 ± 270 (2σ; MSWD = 805) and $^{187}Os/^{188}Os_i$ of 1.6 ± 2.3 (2σ). Regression of data from JT17-19202 (n = 8) yielded a Modal 3 age of 148 ± 41 Ma (2σ; MSWD = 805). Regression of core JT17-19202, however, yielded an $^{187}Os/^{188}Os_i$ (0.55 ± 0.33 (2σ)) similar to cores TS00-27-0031 and JT17-19205, although with a much large uncertainty. Irrespective of this observation, both JT17-19201 and JT17-19202 (UWI: 7-31-79-10W6) yielded erroneous Re-Os ages relative to their stratigraphic position.
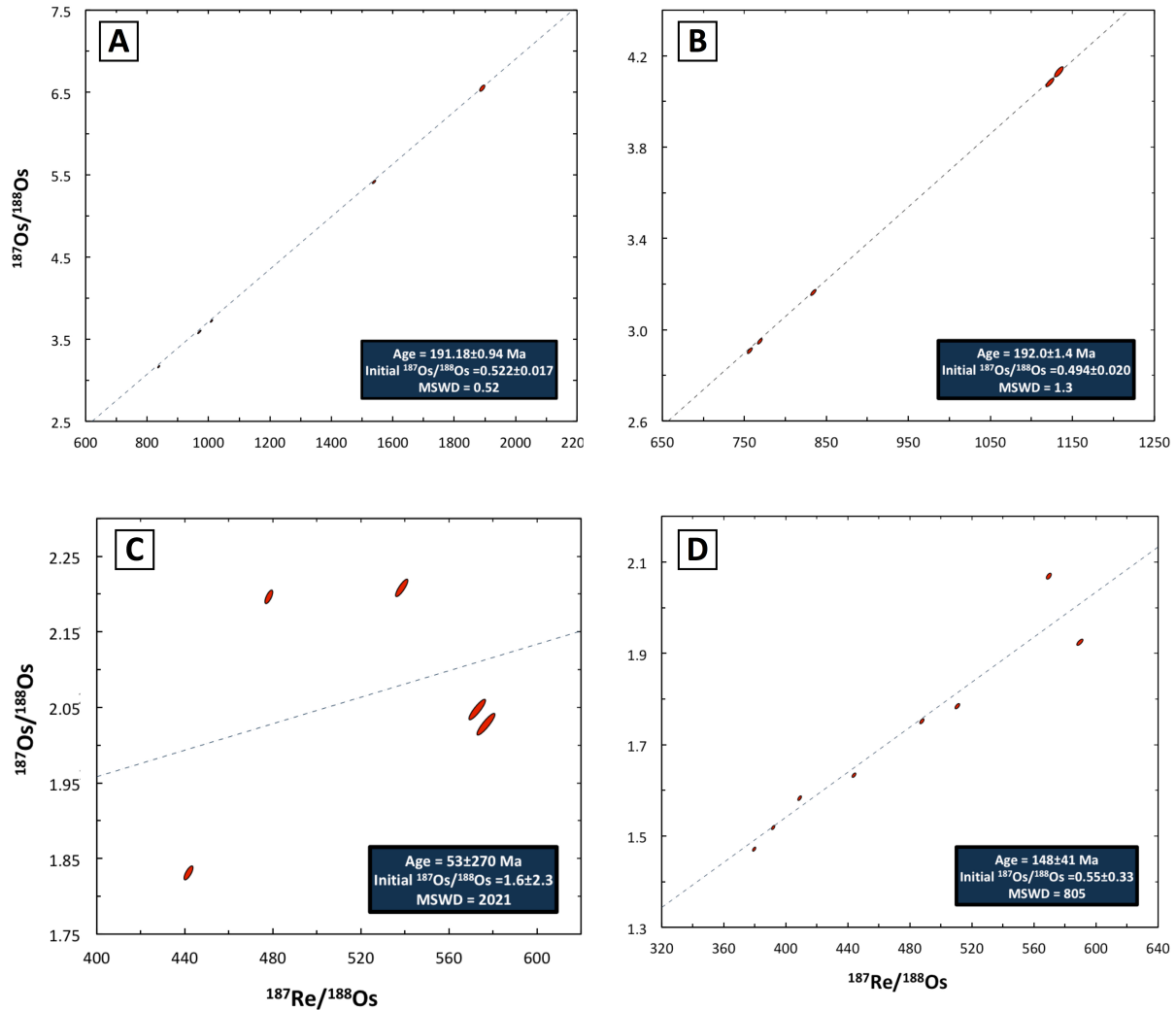
Figure 5.2 Rhenium-Osmium isochrons (A-D) for samples selected from subunit 1A (Lower Gordondale). (A) TS-0027-TS-0031 (n = 5), (B) JT17-19205 (n = 5), (C) JT17-19201 (n= 5), and (D) JT17-19202 (n = 8). Repeat analyses were included only when their $^{187}Os/^{188}Os_i$ ratios were more similar to the $^{187}Os/^{188}Os_i$ ratios of other samples relative to the $^{187}Os/^{188}Os_i$ ratio obtained from the initial measurement (e.g. TS-0029-RPT was included in the regression, while TS-0029 was omitted, since TS-0029-RPT $^{187}Os/^{188}Os_i$ ratio (0.53) is more consistent with the mean average $^{187}Os/^{188}Os_i$ ratio (0.54) for that sample set relative to TS-0029 $^{187}Os/^{188}Os_i$ ratio (0.68)). Error ellipses are reported in 2σ notation and include error propagation from blanks, oxygen isotope corrections, and weighing errors.

5.4.3 Sr Concentrations and Isotopic Ratios

Whole rock strontium along with other major and trace element concentrations are reported in Table 5 (see appendix) and leached Sr isotopic ratios are reported in Table 4 and 6 (see appendix). Measured $^{87}Sr/^{86}Sr$ isotopic ratios and associated (2σ) uncertainties of samples TS0027, TS0029, JT17-19205I, and JT17-19205L of the first leach were 0.707952 ± 0.000031, 0.707770 ± 0.000032, 0.707794 ± 0.000034, and 0.707720 ± 0.000032 and of the second leach were 0.707814 ± 0.000026, 707672 ± 0.000030, 0.707630 ± 0.000021, and 0.707683 ± 0.000025. The $^{87}Sr/^{86}Sr$ isotopic ratios of the second leach were less radiogenic than the first leach, as per Li et al. (2007), which suggests that a diagenetic and/or detrital radiogenic overgrowth component was dissolved in the first leach but not the second. In order to quantify the contribution of this anomalous $^{87}Sr/^{86}Sr$ radiogenic fraction sample TS0029 was selected for repeat analysis of its $^{87}Sr/^{86}Sr$ isotopic ratio and Rb and Sr concentration (Table 3) between leaching phases 1 and 2 (for methodology see section 4.2). Strontium isotopic ratios and Sr and Rb concentrations of sample TS0029-RPT for the first leach were 0.707855 ± 0.000026 (2σ), 7425.61 ppm, 163.74 ppm, and 0.707669 ± 0.000029 (2σ), 21579.45 ppm, and 158.50 ppm in the second leach. By using the Sr and Rb concentrations the calculated $^{87}Rb/^{86}Sr$ ratios of sample TS0029-RPT for the first and second leach were 0.0928 and 0.0309. Employing the ^{87}Rb-^{87}Sr isochron equation in combination with the measured $^{87}Sr/^{86}Sr$ ratio, the calculated $^{87}Rb/^{86}Sr$ ratio, and an assumed age of 191.18 Ma (Re-Os data) the $^{87}Sr/^{86}Sr_i$ ratio of 0.707603 ± 0.000024 and 0.707585 ± 0.000029 was calculated for the first leach and second leach (Figure 5.3).
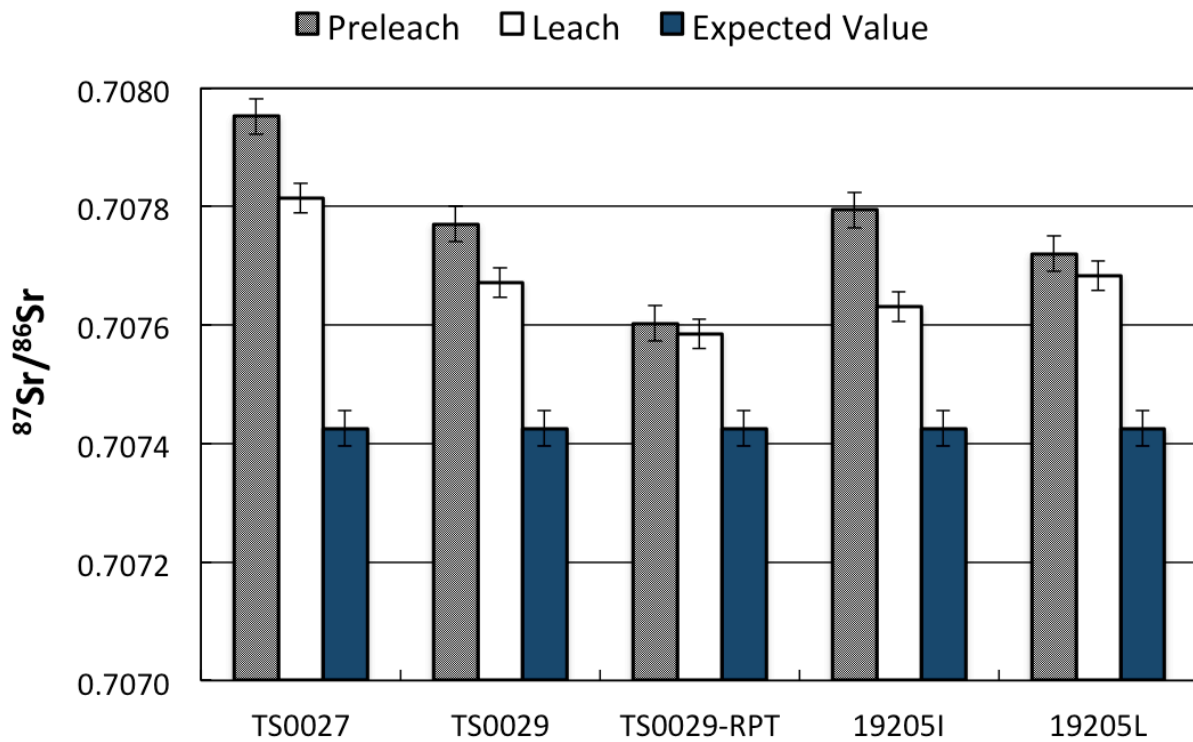
Figure 5.3 Preleached and leached ^{87}Sr/^{86}Sr isotopic compositions Gordondale (TS0027/0029/JT17-19205I/L) of subunit 1A of Lower Radioactive Unit) samples compared to expected values of contemporaneous seawater based on the high-precision Re-Os age results. The ^{87}Sr/^{86}Sr isotopic composition of repeat (RPT) analysis includes the ^{87}Rb/^{86}Sr correction as described in section 5.4.3.

5.5 Discussion

5.5.1 Re-Os Age Significance

Preferentially assigning age significance to radiometric dates requires that the geochronological precepts outlined in Chapter 2 (section 2.6) have been satisfied. For Re-Os ORS geochronology these include (1) strict adherence to close system behaviour, (2) uniformity in ^{187}Os/^{188}Osi isotopes, and (3) variation in the ^{187}Re/^{188}Os ratios between samples. Of the four cores analyzed, regressions of CDN Oxy Belloy (TS0027-0031) and Maclean Creek (19205) yielded results that indicate each of these tenets were met. For example, both CDN Oxy Belloy

and Maclean Creek yielded high-precision (<1%), low MSWD (at or below unity), ages that statistically overlap in their Re-Os ages (191.18 ± 0.94 Ma and 192.0 ± 1.4 Ma) and $^{187}Os/^{188}Os_i$ ratios (0.522 ± 0.017 and 0.494 ± 0.020). In contrast, Dome Gordondale cores (19201 and 19202) yielded highly imprecise (30%), high MSWD (30 and 805), ages. This suggests geological disturbance of some form, either variation in the $^{187}Os/^{188}Os_i$ ratios or open-system isotopic exchange, has compromised the ability of obtaining high precision age results. With that said, since all four cores were sampled from subunit 1A of the Lower Radioactive Unit, and 2/4 cores yielded high precision ages, then open-system behavior – as a probable source of age imprecision in Dome Gordondale cores – can be ruled out. This conclusion is also supported by the absence of physical features, such as hydrothermal quartz veins or bioturbation, in the cores that would otherwise suggest Re and Os re-mobilization. Therefore, it is argued that fluctuations in $^{187}Os/^{188}Os_i$ ratios of the contemporaneous water column is the major cause of the age uncertainty in Dome Gordondale cores, with possible subsidiary effects related to a lack of spread in $^{187}Re/^{188}Os$ ratios (19201: $^{187}Re/^{188}Os$ = 1.5 to 2; 19202: $^{187}Re/^{188}Os$ = 1.5 to 2.2).

5.5.2 Age Revision of subunit 1A of the Lower Radioactive Unit

Biostratigraphy brackets the depositional age of subunit 1A of Lower Radioactive Unit of the Gordondale Member to Hettangian and Sinemurian stages (Asgar-Deen et al., 2004; Hall and Pitaru, 2003; Hall et al., 2000). The assigned age, however, is Hettangian according to (1) the appearance of ammonite specimen *D. silberlingi* in the basal section (subunit 1A) of CDN Oxy Belloy, (2) correlative Hettangian ammonite specimens in Gordondale Member outcrop located in NE British Columbia, and (3) subsurface fossil specimens resembling Hettangian ammonites (UWI = 12-4-73-2W6) (Asgar-Deen et al., 2004; Hall et al., 2000). In contrast, the Re-Os ORS ages of CDN Oxy Belloy and Maclean Creek, when including uncertainty, are unequivocally Late Sinemurian to Early Pliensbachian. Thus, the radiometric data obtained from Re-Os ORS geochronology directly contradicts Lower Gordondale Member biostratigraphy based on the ammonite *D. silberlingi*. However, coccolith specimens identified by Hall et al.

(2000) in CDN Oxy Belloy, which co-occur with *D. silberlingi* (1018.5 m) and intersect TS-0027-0031 (1018.5 m) sample location, are entirely consistent with the Re-Os ORS age obtained in this study.

Hall et al. (2000) had originally argued that coccolith specimens *T. patulus, M. elegans*, and *P. liasicus* correlate with those found in upper Hettangian and Lower Sinemurian strata of Europe, and therefore bracket the depositional age of subunit 1A of the Lower Radioactive Unit of the Gordondale to this interval. However, this interpretation is now obsolete due to a more robust understanding of the Early Jurassic calcareous nannofossil record. The occurrence of *C. crassus* in NW Europe, the Mediterranean (Italy/S France), Lusitanian Basin (Portugal), N Spain, and Paris Basin (France) across the late Sinemurian to Early Pliensbachian ammonite zone *Oxynoticeras oxynotum* to *U. jamesoni* marks an important calcareous nannofossil evolutionary event in Tethyan and Boreal realms, which has officially been designated as nannofossil zone NJ3 as defined in the Geologic Time Scale (Ogg et al., 2016; Ogg et al., 2012). Although the first occurrence of *P. liasicus*, *T. patulus*, *M. jansae*, *M. elegans*, and *C. primulus* in Tethyan and Boreal realms pre-dates *C.crassus*, *they* have all been recognized to co-occur with *C. crassus* during this interval (Peti et al., 2016; Plancq et al., 2016). In addition, *P. liasicus*, *T. patulus*, and *M. elegans* in the Paris Basin and Lusitanian Basin of Tethyan and Boreal realms are only abundant in occurrence in ammonite zone *E. raricostatum* and *U*. *jamesoni* of the Late Sinemurian and Early Pliensbachian, which may help explain their apparent abundance in CND Oxy Belloy of subunit 1A (UWI = 6-19-78-25W5) of the Lower Radioactive Unit of the Gordondale Member (Peti et al., 2016; Plancq et al., 2016).

The direct calibration of *C. crassus* to standard ammonite zone *O. oxynotum to U. jamesoni* in Tethyan and Boreal realms allows us to correlate subunit 1A the Lower Radioactive Unit of the Gordondale Member with global biostratigraphic tie points. On the other hand, ammonite specimen *D. silberlingi* is only found, regionally, in three other localities – Nevada, Alaska, British Columbia - in North American strata, and is only indirectly correlated, via *A. liasicus* species, with globally recognized Early Jurassic ammonite zones (Longridge et al., 2008). Although Asgar-Deen et al. (2004) did identify ammonite fossils and impressions in the

subsurface of the Lower Gordondale Member (subunit 1A) the preservation states of these fossils lead the authors to conclude a tangential *resemblance* to ammonite genus *Alsatites* and *Caloceras*. These partial fossil remains are the only subsurface fossils in proximity to CND Oxy Belloy that link the Lower Gordondale to Hettangian stages. Hettangian ammonite specimens have been identified in Gordondale outcrop of Black Bear Ridge located in the Williston Lake area of NE British Columbia (Hall and Pitaru, 2004). However, the tie between these two disparate locations, by way of Hettangian ammonites, has been severed by the newly acquired Re-Os data, and no longer remains tenable.

More consistent with the stratigraphic framework of the Lower Radioactive Unit is the late Early Pliensbachian ammonite (?)acanthopleuroceratid *as* recognized by Poulton et al. (1990) in subsurface strata of subunit 1B of the Lower Radioactive Unit of the Gordondale Member in NW Alberta (UWI = 12-33-77-21W5) that correlates with late Early Pliensbachian ammonites identified in Gordondale Member outcrop in Section 62-15 and Pine River map area of the Williston Lake area ~ 50 km N to NW of Black Bear Ridge (see Figure 3.1). The occurrence of (?)acanthopleuroceratid ammonites in conjunction with *Prodactylioceras* sp. and *Lytoceras* sp. in Section 62-15 and Pine River purportedly correlates with international standard ammonite zone *P. davoei* of the late Early Pliensbachian (~ 187-185 Ma) (Frebold, 1970; Ogg et al. 2012; Poulton et al.,1990). Although more recently the FO of *Acanthopleuras* sp. recognized in the Sancerre-Couy Core of the Paris Basin, correlates with ammonite biohorizon *Tragophylloceras Ibex* above ammonite zone *U. jamesoni* that defines the base of the Pliensbachian stage (Peti et al., 2016).

Evidence of Late Sinemurian to Early Pliensbachian faunal assemblages have also been recognized in outcrop of the Red Deer Member– a transitional facies between The Gordondale Member and the Nordegg Member - located in Bighorn Creek of west-central Alberta (Figure 3.1). At the base of the Red Deer Member, Hall et al. (2004) identified partial specimens of *Epophioceras cf. brenoi* and *Asteroceras stellare* that correlate with Upper Sinemurian international standard ammonite zone *Asteroceras obtusum*. Approximately 2 meters above the base of the bed, Hall et al. (2004) identified partial impressions of Late Pliensbachian

ammonites *Amaltheus* sp*.* and *Amauroceras* sp*.* and coccolith specimens *B. novum*, *C. crassus*, *M. elegans*, *B. liasicus*, *S. praecarium*, and *T. patulus*. The presence of *C. crassus* is consistent with an Early Pliensbachian depositional event. In addition, a bentonite layer 0.2 m above the base of the Red Deer Member at Bighorn Creek yielded a weighted average U-Pb zircon age of 188.3 + 1.5/-1 Ma (Hall et al., 2004). A more recent single-grain U-Pb zircon analysis of the bentonite layer at Bighorn Creek yielded an Early Pliensbachian age of 188.58 ± 0.17 Ma that supports previous U-Pb data reported by Hall et al. (2004) (Them et al., 2017) (see Figure 10.1 in appendix).

Multiple other bentonite ash beds have been identified in Poker Chip and Nordegg Member outcrop elsewhere across Alberta that yield similar Pliensbachian depositional ages (Them et al., 2017; Pană et al., 2018b, in press). For example, bentonite U-Pb zircon dates in lower-to-mid sections of Nordegg Member outcrop in McLeod River, Shunda Creek, and Prairie Creek yielded consistently Early Pliensbachian ages, whereas mid-to-upper sections of Poker Chip and Nordegg Member outcrop in Bighorn Creek, Prairie Creek, and Crossnest Pass area yielded Late Pliensbachian ages (see Figure 3.1 and Figure 10.1 in appendix) (Them et al., 2017; Pană et al., 2018b, in press)

5.5.3 Implications for the Sinemurian-Pliensbachian Boundary

The International Union of Geological Sciences (IUGS) ratified Robin Hood's Bay, Yorkshire, UK as the Global Boundary Stratotype Section Point (GSSP) for the base Pliensbachian stage (Meister et al., 2006). The base Pliensbachian is marked by the first appearance of ammonite taxa *B. donovani* of ammonite zone *U. jamesoni* and coccolith flora *S. cruciulus* of calcareous Nannofossil zone NJT4a in the Pyritiferous Shale Member of the Redcar Formation, which correlates with Boreal ammonite zones in NW Europe (Meister et al., 2006; Ogg, 2016). In North America, this is equivalent to ammonite zone *Tetraspidoceras* sp. (Pálfy et al., 2000). Coinciding with the first appearances of ammonite *B. donovani* and coccolith *S. cruciulus* at Robin Hood's Bay is a seawater $^{87}Sr/^{87}Sr$ value of 0.707425 ± 0.00004, which is reproduced elsewhere globally, and defines a midpoint between the high seawater Sr value of

the end-Triassic and the low seawater Sr value of the base Toarcian (Meister et al., 2006; Ogg et al., 2012). The seawater $^{187}Os/^{188}Os$ value concurrent with the $^{87}Sr/^{86}Sr$ value recorded at Robin Hood's Bay is 0.48 ± 0.03, and purportedly reflects the steady-state background signal of the Early Jurassic (Porter et a., 2013).

Pálfy et al. 2000 interpolated a base Pliensbachian age of 191.5 +1.9/-4.7 Ma from multiple single-grain and multi-grain U-Pb zircon ages of volcanic ash beds/lava flows interstratified/overlying British Columbia strata proximal to North American ammonite zone *Tetraspidoceras* sp., which is equivalent to Tethyan and Boreal ammonite zones *E. raricostatum* and *U. jamesoni* (Pálfy et al. 2000b). The Geologic Time Scale (Gradstein, 2012), however, reported slightly younger numerical age projections of 190.3 ± 1 Ma for the GSSP at Robin Hood's Bay. Direct Re-Os ORS ages of the Pyritiferous Shale Member 2.4 to 3.0 m above the base Pliensbachian stage at Robin Hood's Bay yielded an imprecise age of 194 ± 4.8 (2.5%) that agrees within uncertainty of both Pálfy et al. (2000) and Gradstein (2012) original age estimates (Porter et al., 2013). Recent refinements of radiometric tie points at the base Sinemurian and Toarcian stages have resulted in new numerical age projections of 191.4 ± 1 Ma for the base Pliensbachian at Robin Hood's Bay that agrees independently with Pálfy et al. (2000) original chronogram estimate (Ogg et al., 2016), and Porter et al. (2013) imprecise Re-Os ORS age. Recent astronomical age projections of Ruhl et al. (2016) have challenged these previous numerical age projections by redefining the base Pliensbachian stage at 192.5 ± 0.4 Ma. The astrochronological method employed by Ruhl et al. (2016), however, has been criticized by Smith et al. (2017) on statistical grounds, and henceforth remains to be resolved. The direct Re-Os ages of 191.18 ± 0.94 Ma and 192.0 ± 1.4 Ma obtained from subunit 1A of the Lower Radioactive Unit of the Gordondale Member, however, corroborates both numerically projected ages of Ogg et al. (2016) and Pálfy et al. (2000) whilst statistically overlapping the controversial astronomical projections of Ruhl et al. (2016). However, statistical agreement between the seawater Os isotopic composition of the Gordondale Member (0.52 ± 0.02; 0.49 ± 0.02) with those measured at the base Pliensbachian at Robin Hood's Bay by Porter et al. (2013) provide ancillary support for a base Pliensbachian age of 191.18 ± 0.94 Ma (Figure 5.1/5.4).
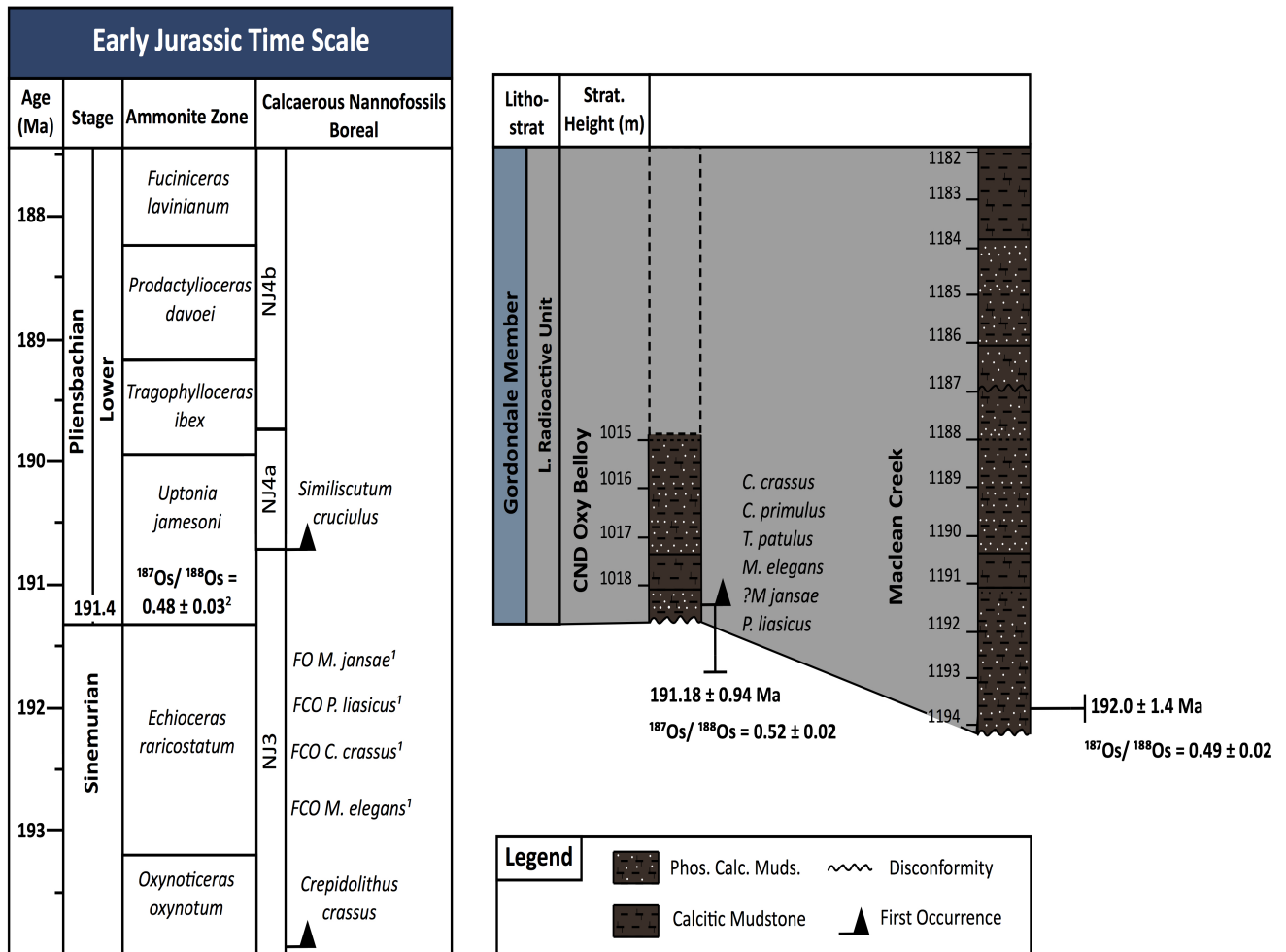
Figure 5.4 Re-Os ORS ages, $^{187}Os/^{188}Os_i$ ratios, and $^{87}Sr/^{86}Sr$ ratios of CND Oxy Belloy and Maclean Creek correlated with the Early Jurassic Time Scale (Ogg et al., 2016). The Sinemurian-Pliensbachian stage boundary is defined at Robin Hood's Bay, Yorkshire, UK by the first appearance of ammonite taxa *B. donovani*, a $^{187}Os/^{188}Os$ ratio of 0.48 ± 0.03, and a $^{87}Sr/^{86}Sr$ ratio of 0.707425 ± 0.00004. Coccolith flora of the species *C. crassus* and *M. jansae* identified in CND Oxy Belloy is consistent with a Late Sinemurian-Early Pliensbachian age corresponding to NW European ammonite zones *E. raricostatum* and *U. jamesoni*. [1]Peti et al. (2016) [2]Porter et al. (2013).

Measurements of the seawater $^{87}Sr/^{86}Sr$ value of subunit 1A of the Lower Radioactive Unit of the Gordondale Member, however, complicate a base Pliensbachian age interpretation. For example, the closest $^{87}Sr/^{86}Sr$ value, when including $^{87}Rb/^{86}Sr$ correction, recorded in

subunit 1A of the Gordondale Member is 0.707585 ± 0.000029 (TS0029-RPT). When including uncertainty, the seawater Sr value recorded in subunit 1A of the Gordondale Member is 0.000127 more radiogenic than the seawater Sr value recorded at Robin Hood's Bay, Yorkshire, UK. Assuming the $^{87}Sr/^{86}Sr$ value recorded in subunit 1A of the Gordondale Member reflects global contemporaneous seawater requires a Late Sinemurian age (193.1 -194.1 Ma) corresponding to ammonite zone *O. oxynotum* (Ogg et al., 2016; Jones et al., 1994). This Late Sinemurian age, while overlaps within uncertainty of Re-Os age 192.0 ± 1.4 (JT17-19205), is irreconcilable with the Re-Os age of 191.14 ± 0.94 (TS0027-0031) that corresponds to ammonite zones *E. raricostatum* and *U. jamesoni* of the Late Sinemurian and Early Pliensbachian. This suggests that the $^{87}Sr/^{86}Sr$ value recorded in subunit 1A of the Gordondale Member does not reflect contemporaneous seawater. Two possible reasons may account for the discrepancy between the seawater Sr value recorded in subunit 1A of the Gordondale Member and the global seawater Sr value recorded at Robin Hood's Bay: (1) Sr isotopic heterogeneity developing in response to basin restriction or (2) a diagenetic and/or detrital Sr isotopic effects interfering with the seawater Sr isotopic signal present in subunit 1A Lower Radioactive Unit Gordondale Member samples. Agreement between the seawater Os signal recorded in subunit 1A Lower Radioactive Unit Gordondale Member and the seawater Os signal recorded at Robin Hood's Bay coupled with Os (10-50 Ka) shorter residence time in the ocean relative to Sr (1-2 Ma) negates the viability of the first hypothesis. By contrast, support for the second hypothesis derives from Rb being present alongside Sr in the leachate. It is conceivable that the Rb measured was only a fraction of the entire Rb pool in the samples. An unaccounted for Rb fraction would adversely effect the seawater Sr isotopic composition by making it appear more radiogenic as ^{87}Rb decays into ^{87}Sr.

5.5.4 Sinemurian-Pliensbachian Seawater Os Composition

Dissolved Os exists in seawater as an oxyanion delivered to the oceans by vectors contributing both unradiogenic (mantle/extraterrestrial) (^{187}Os/^{188}Os$_{mantle}$ = 0.113; ^{187}Os/^{188}Os$_{extraterrestrial}$ = ~0.127) and radiogenic (continental) sourced Os (^{187}Os/^{188}Os$_{continental}$ = ~1.26) (Peucker-Ehrenrink and Ravizza, 2000). Continental weathering, for example of Precambrian bedrock, results in the transfer of radiogenic Os into rivers that become primary transport vectors of radiogenic Os into the oceans. Other anomalous radiogenic sources of Os delivered to the oceans include aeolian and anthropogenic input, although the latter flux is not applicable beyond the modern ocean reservoir. By contrast, mantle derived Os is delivered to the oceans by hydrothermal fluxes, such as deep sea vents, whereas extraterrestrial sourced Os is delivered to the oceans by micrometeorites and/or in the rare event a bolide impact, such as the 10-15 km diameter estimated asteroid impact that extirpated the dinosaurs at the K-T boundary (Peucker-Ehrenrink and Ravizza, 2000). The seawater Os isotopic composition is, therefore, relegated to the dominant Os flux delivered to contemporaneous oceans. Osmium flux estimates of the modern marine reservoir suggest riverine transport of continentally derived Os contributes the largest fractional load of dissolved Os to the oceans, which is followed by hydrothermal fluids and aeolian dust in equal proportions, and then cosmic dust (Peucker-Ehrenbrink and Ravizza, 2000). A dominantly riverine Os flux to the modern oceans, for example, has shifted the seawater Os isotopic composition (^{187}Os/^{188}Os = 1.05) towards the radiogenic Os end-member (^{187}Os/^{188}Os$_{continental-runoff}$ = 1.49-1.54) (Peucker-Ehrenbrink and Ravizza, 2000).

The seawater Os isotopic composition coincident with the end-Triassic extinction of the Rhaetian records a transient perturbation from ~0.6 to ~ 0.2 linked to CAMP flood basalt volcanism. This transient Os isotopic excursion shortly rebounded to pre-extinction values of ~0.6 by the Late Hettangian as volcanogenic gases, namely CO_2, released from CAMP volcanism increased the supply of continental runoff to the oceans through enhanced continental weathering (Kuroda et al., 2010). Kuroda et al. (2010) surmised that by the Early Sinemurian seawater ^{187}Os/^{188}Os reached a new steady state of ~0.48. Between the Early to Late

Sinemurian, however, the seawater Os isotopic composition fluctuates widely and does not signal maintenance of steady state as recognized by Kuroda et al. (2010). For example, sediment of Dorset, UK records an Os isotopic composition of 0.49, 0.38, and 0.59 in Middle Sinemurian seawater (~195-193 Ma) (Cohen et al., 1999) (Figure 5.5). In contrast, Middle Sinemurian (196.64 to 194.42 Ma) sediment of Last Creek of North American ammonite zone *Leslei* sp. (equivalent to ammonite zone *Arnioceras semicostatum* and *Caenisites turneri*), British Columbia, Canada records both unradiogenic and radiogenic values ranging from 0.11 to 0.91 (Porter et al., 2014) (Figure 5.5). By the end of North American ammonite zone *Leslei* sp. of the Late Sinemurian (~194.9 Ma), sediment of Last Creek records a seawater Os isotopic composition of 0.12. An open-ocean arc depositional setting purportedly controlled the local seawater Os isotopic composition at Last Creek through intermittently releasing unradiogenic Os into the water column (Port et al., 2014). While this explanation provides a viable account for the unradiogenic Os values recorded at Last Creek, it fails to justify the radiogenic values recorded in excess of the assumed background seawater Os composition (>0.48). By comparison, the seawater Os isotopic composition of NW European sediment of Robin Hood's Bay, Yorkshire, UK of Late Sinemurian ammonite zone *E. raricostatum* 3 m below the Sinemurian-Pliensbachian boundary is 0.37, which fluctuates between 0.24 and 0.44 over the entire 3 m interval (Figure 5.1/5.5) (Porter et al., 2013). Porter et al. (2013) posited that between the Late Sinemurian and the Early Pliensbachian, Early Jurassic seawater Os transitioned from a predominantly radiogenic to unradiogenic composition as the supply of hydrothermally sourced Os increased as proto-rifting of Pangaea continued. A transient spike to radiogenic Os values coincident with the S-P boundary, therefore, reflected a hiatus in the input of unradiogenic Os to the oceans as proto-rifting halted. Porter et al. (2013) argued, then, that seawater Os recorded at the S-P boundary at Robin Hood's Bay, and similarly observed in both CND Oxy Belloy and Maclean Creek cores, reflected the steady state background seawater Os isotopic composition first surmised by Kuroda et al. (2010). However, resolving Porter et al. (2013) hypothesized ephemeral reestablishment of a seawater Os steady state coincident with the S-P boundary with widely variable seawater Os values throughout the entirety of the Sinemurian remains challenging not withstanding the fact that some contemporaneous

seawater Os values of basal Dome Gordondale cores record isotopic values in excess (JT17-19201A $^{187}Os/^{188}Os_i$ = 0.67) of the steady state ($^{187}Os/^{188}Os$ = 0.48) proposed by Porter et al. (2013).
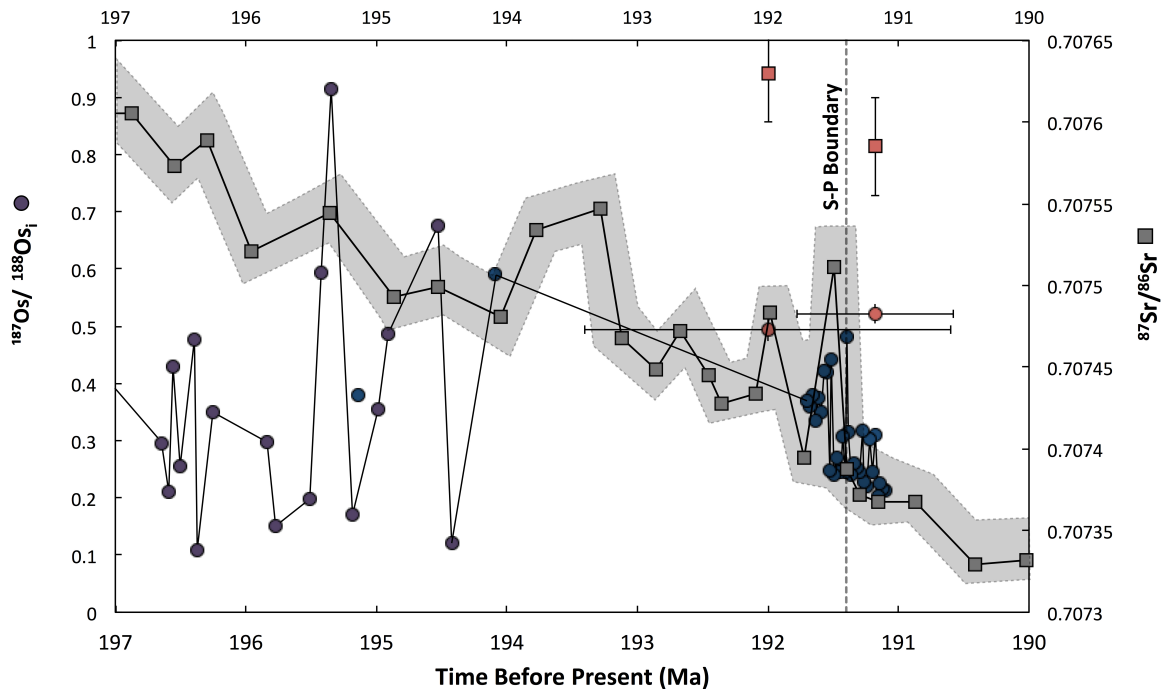
Figure 5.5 Early Jurassic seawater Os and Sr curve. Red circles and squares correspond to $^{187}Os/^{188}Os_i$ and $^{87}Sr/^{86}Sr$ ratios of sample cores (TS0027-0031 and JT17-19205) from subunit 1A of the Lower Radioactive Unit of the Gordondale Member. The seawater $^{87}Sr/^{86}Sr$ curve (shown in grey squares/bar) is derived from belemnites of Yorkshire, UK (Jones et al., 1994), and the seawater $^{187}Os/^{188}Os$ curve (shown as blue circles) is derived from Western North American and Tethyan ORS (Cohen et al., 1999; Porter et al., 2013, 2014).

If Porter et al. (2013) hypothesized reestablishment of seawater Os steady state conditions of the S-P boundary at Robin Hood's Bay remains questionable, then a second hypothesis that better accounts for the data should be proposed. One such alternative hypothesis could be that proto-rifting of Pangaea continued to supply unradiogenic Os to the oceans unabatedly through the Sinemurian-Pliensbachian transition, but that rapid influxes of

continentally derived Os to the oceans shifted the seawater Os isotopic composition to more radiogenic values.

The observed steady decline in contemporaneous seawater Sr values of 0.70795 at the end-Triassic to 0.70708 at the Late Pliensbachian supports a hypothesized persistent flux of unradiogenic Sr, and presumably Os, entering Early Jurassic oceans from increased hydrothermal activity related to continued proto-Atlantic rifting (Jones et al., 1994; Jenkyns et al., 2002; Rul et al., 2016; Van Der Meer et al., 2014) (see Figure 5.5). Jones et al. (1994) contend that the flux of continentally sourced Sr remained stable during this period, which negates the possibility of a presumed decreased continental weathering flux of radiogenic Sr to explain the observed downward trend of more unradiogenic Sr seawater values. Ruhl et al. (2016) surmise that seawater Sr coincident with the S-P boundary event stabilized around 0.70740 for approximately 2 Ma, which purportedly reflected an uptick in continental weathering rates related to volcanogenic CO_2 released from a late-stage pulse of CAMP volcanism (Korte and Hesselbo, 2011). Biotite and plagioclase $^{40}Ar/^{39}Ar$ dating of basaltic lava flows, sills, and dykes confirms a protracted CAMP emplacement event of ~ 191-187 Ma that corresponds to the S-P boundary event (Beutel et al., 2005; Jourdan et al., 2009; Marzoli et al., 2011; Nomade et al., 2006; Verati et al., 2006). This late-stage emplacement event appears to be non-localized, with both intrusive and extrusive igneous emplacement ages found in North America, South America, Portugal, and Morocco, which signals regional coverage across a proto-disaggregating Pangaea. A large magnitude event as such, therefore, offers a plausible mechanism to account for the observed shift from a presumed Late Sinemurian and Pliensbachian unradiogenic background seawater Os signal of 0.2-0.3 (Porter et al., 2013; Them et al., 2017) to a transient radiogenic signal of 0.48-0.67 concurrent with the S-P boundary as recorded at Robin Hood's Bay and the WCSB (Figure 5.6).

Although precisely constraining crustal-derived $^{187}Os/^{188}Os$ supplied by rivers to Early Jurassic oceans remains to be constrained, an approximate value can be inferred from present-day continental weathering sources ($^{187}Os/^{188}Os$ = 1.4). Assuming that Early Jurassic oceans were dominated by a binary flux of (1) hydrothermal ($^{187}Os/^{188}Os$ = 0.13) and (2) continental Os,

therefore, allows the percent contribution of each flux to be estimated [see equation 5.1/5.2]. Pre- and post-late-phase CAMP emplacement continental fluxes contributed an estimated 9-20% of the total dissolved Os delivered to the oceans, which is in contrast to an estimated 38-57% continental flux contribution concurrent with an inferred late-stage CAMP emplacement event. Comparatively this amounts to a 411-622% increase in continentally derived Os to the oceans from pre- and post-late-stage CAMP emplacement levels.

Equation 5.1

$$^{187}Os/^{188}Os_{seawater} = f_{continental}(^{187}Os/^{188}Os_{continental}) + f_{mantle}\,(^{187}Os/^{188}Os_{mantle})$$

Equation 5.2

$$f_{continental} = (^{187}Os/^{188}Os_{seawater} - \,^{187}Os/^{188}Os_{mantle})/$$

$$(^{187}Os/^{188}Os_{continental} - \,^{187}Os/^{188}Os_{mantle})$$

The relative increase in continental weathering rates coeval with the S-P boundary event are comparable to those that post-date the main-phase of CAMP volcanism of the Triassic Rhaetian and Jurassic Hettangian stages and the T-OAE (Kuroda et al., 2010; Percival et al., 2016 Them et al., 2017). The latter event, however, appears more reminiscent of the global climatic and carbon cycle perturbations that transpired at the S-P boundary event. The T-OAE, recognized for widespread deposition of organic-rich facies and biotic crisis, records a globally prominent 2‰ negative and 7 ‰ positive CIE similar, although larger in magnitude, to those observed in marine organic carbon and carbonates of the S-P boundary (Jenkyns et al., 2002; Korte and Hesselbo, 2011).

The short-term negative-CIE of Late Sinemurian Boreal ammonite zone *E. raricostatum* to Early Pliensbachian ammonite zone *U. jamesoni* is also synchronous with the deposition of organic-rich facies in the Asturian Basin (N. Spain), Lusitanian Basin (Portugal), Basque-Cantabarian Basin (N. Spain), and Middle Atlas (Morocco) (Gómez et al., 2016). Temporally equivalent organic-rich facies (up to 40 wt.% kerogen) of the basal Gordondale Member (subunit 1A of the Lower Radioactive Unit) are, therefore, predicted to record an analogous

negative-CIE. These inflections in the Early Jurassic carbon cycle are purportedly linked to destabilization of methane clathrates, release of thermogenic methane from intrusive activity, and/or CO_2-induced continental weathering (Hesselbo et al., 2000; Svensen et al., 2007). Though a prominent Os isotope excursion concurrent with the T-OAE confers a more direct causal link between carbon burial flux and rapid continental weathering triggered by climatic hothouse-inducing volcanogenic CO_2 of the Karro-Ferrar LIP event (Percival et al., 2016; Them et al., 2017). An analogous release of ^{13}C-depleted CO_2 into the atmosphere from late-stage CAMP volcanism would, therefore, viably account for both an inferred period of seawater Sr stability and an observed negative-CIE at the S-P boundary (Korte and Hesselbo, 2011; Ruhl et al., 2016; Them et al., 2017).

A $\delta^{18}O$ excursion at the S-P boundary event that extends into Early Pliensbachian ammonite zone *P. davoei*, suggest a global warming-type event possibly induced by late-stage CAMP volcanism (Gómez et al., 2016; Korte and Hesselbo, 2011; Merino-Tomé et al., 2012). A large supply of greenhouse gases to the paleo-atmosphere would create a more active hydrologic cycle, accelerate silicate weathering of the continents, and presumably increase the flux of bioavailable nutrients in the oceans. Indeed, enrichment of bioavailable elements P_2O_5 (deried from fish fossils) and Ba above average shale levels in basal sections of the Gordondale Member supports a more active hydrologic cycle (Asgar-Deen 2003; Asgar-Deen et al., 2004; Ross and Bustin, 2006). This presumably increased productivity in the water column, and therefore provides explanatory power for why basal Gordondale Member sections, which are inherently more OM-rich than any other sections of the Gordondale Member, contain OM-enrichments in excess of 30 wt.% (Asgar-Deen et al., 2004; Riediger, 1990).

Despite these similarities between the T-OAE and the S-P boundary event, the duration of the T-OAE, estimated at 300-500 Ka, is a fraction of the purported 2 Ma duration of the S-P boundary event (Ruhl et al., 2016; Them et al., 2017). If continental weathering remained in accelerated form during this entire 2 Ma interval, then a noticeable Os-IE would be present in the marine sedimentary archive. This, however, is contrary to observations at Robin Hood's Bay where a transient shift to radiogenic seawater Os values (0.48) coincident with the S-P

boundary tappers off to values of 0.32 and 0.24 over a 0.4 m interval in the base *U. jamesoni* ammonite zone (Percival et al., 2016; Porter et al., 2013; Them et al., 2017). Whether the shift in radiogenic seawater Os values recorded at Robin Hood's Bay is similarly transient in extent in the Gordondale Member of the WCSB remains to be established.

The duration of a suspected Os-IE event can be bracketed to a ~ 2 m interval via the reappearance of unradiogenic seawater Os values (0.17-0.28) (~1556 m; core JT17-19202) above a radiogenic section (0.50-0.67) (~1558 m; JT17-19201) of the basal Gordondale Member, which similarly corresponds to a zone of OM-enrichment of up to 25 wt.% kerogen in Dome Gordondale well (Figure 5.6). This allows for an upper/lower-limit estimate of an Os-IE event to be quantified via an assumed (1) average 25 m stratigraphic height of the Gordondale Member and (2) continuous sediment depositional rates over an interval of 11.79 ± 1.54 Ma (upper contact = 179.39 ± 0.60 Ma [see Figure 6.8 Chapter 6]; lower contact = 191.18 ± 0.94 Ma [Figure 5.2]). Inferred upper and lower estimate rates of sediment deposition in m/Ma, therefore, are 2.4 m/Ma and 1.9 m/Ma.

Although sediment depositional hiatuses have been observed in the Gordondale Member, low rates of sedimentation are expected in basinal depositional settings, which may help resolve presumably condensed ORS packages of the Gordondale Member (Asgar-Deen, 2003; Asgar-Deen et al., 2004). Irrespective of these inherent uncertainties, a possible maximal duration for an Os isotopic perturbation recorded in subunit 1A of the Lower Radioactive Unit of the Gordondale Member is between 0.83-1.1 Ma.

At the moment, the extent of an Os-IE in the basal Gordondale Member remains speculative. However, major carbon cycle perturbations coincident with the S-P boundary coupled with synchronous OM-enrichments of up 40 wt.% kerogen [chapter 8] in the Gordondale Member and Early Jurassic organic-rich facies elsewhere provide good reason to suspect a perturbation in the marine Os cycle. In order to test this hypothesis, a replicate studying investigating Os isotope stratigraphy through the Sinemurian-Pliensbachian transition is required. A viable candidate is the Gordondale Member since it was deposited in an open-ocean sedimentary basin.
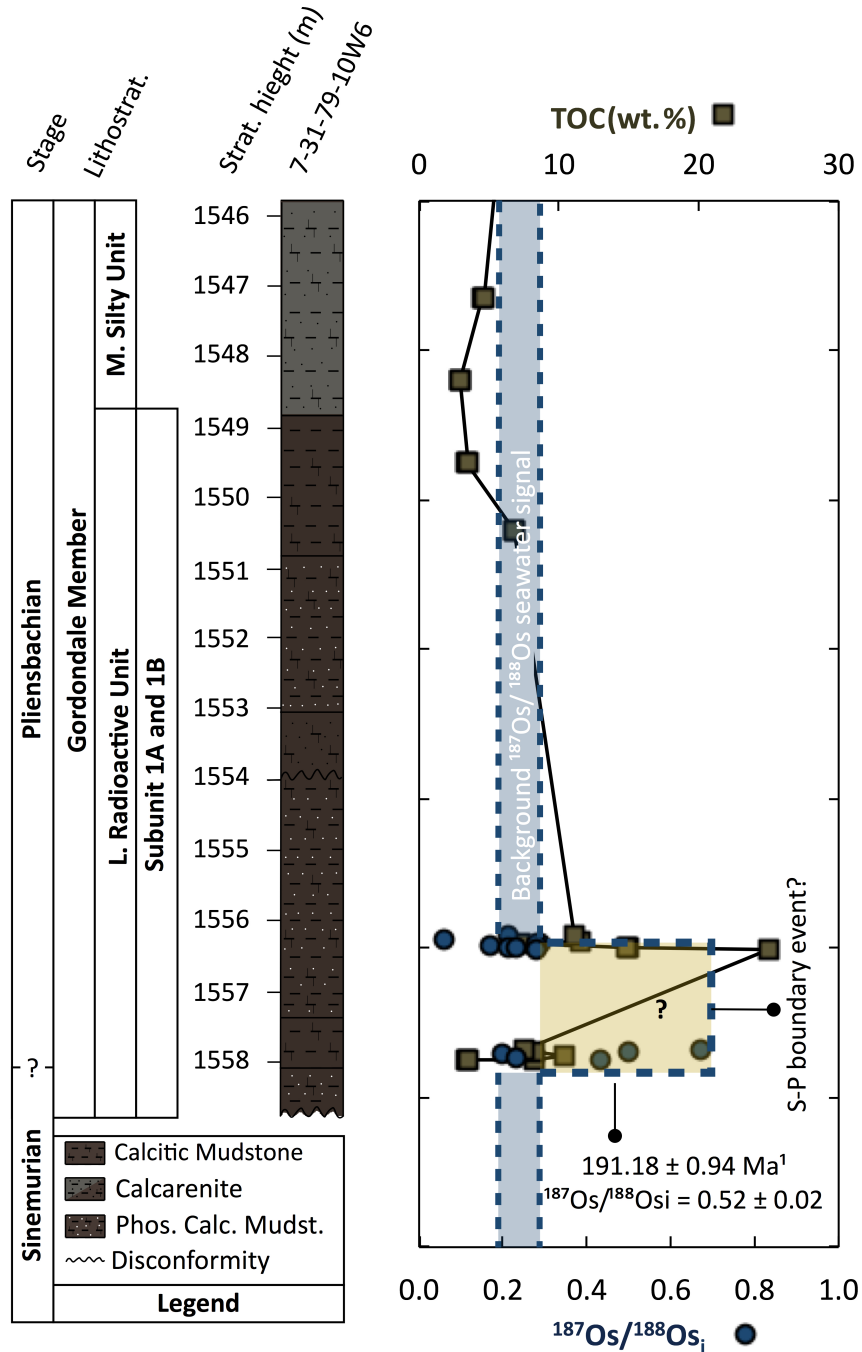
Figure 5.6 Plot of $^{187}Os/^{188}Os_i$ and TOC (wt. %) versus stratigraphic height (m) of Dome Gordondale (UWI = 7-31-79-10W6). Blue bar indicates background range of $^{187}Os/^{188}Os$ seawater values as reported by Porter et al. (2013) and Them et al. (2017). Orange bar indicates

suspected ~ 2 m stratigraphic interval of the S-P boundary event. This section corresponds to an organic-rich interval with TOC values as high as 25 wt.%. [1]Re-Os ORS age of subunit 1A of the Lower Radioactive Unit CND Oxy Belloy (UWI = 6-19-78-25W5), which has a $^{187}Os/^{188}Os$ seawater value of 0.52 ± 0.02 that matches a corresponding value of 0.50 at a depth of ~ 1557.8 m in Dome Gordondale.

5.6 Conclusion

High precision Re-Os ORS geochronology of subunit 1A of the Lower Radioactive Unit of the Gordondale Member yielded two precise depositional ages of 191.18 ± 0.94 Ma and 192.0 ± 1.4 Ma that are irreconcilable with the Hettangian age of ammonite specimen *D. silberlingi*, but agree with intercalated microflora specimens, which requires that a depositional age revision of Late Sinemurian-Early Pliensbachian be adopted for subunit 1A. Furthermore, the radiometric age agreement between subunit 1A of the Lower Radioactive Unit of the Gordondale Member and the numerical age projection of the S-P boundary at Robin Hood's bay combined with agreement in the $^{187}Os/^{188}Os_i$ ratio tentatively implies that this stratigraphic interval corresponds to the S-P boundary.

6 | Direct Re-Os ages of the Late Pliensbachian and Toarcian

6.1 Introduction

The Late Pliensbachian and Early Toarcian time interval is recognized for the ubiquitous spread of coastal anoxia, and a subsequent decline in marine biodiversity (Gradstein, 2012; Jenkyns, 2010). The triggering event responsible has been reduced to early- and late-stage volcanism of the Karro-Ferrar LIP (K-LIP) of South Africa and Antarctica (Little and Benton, 1995; Sell et al., 2014). An interstratified tephra volcanic ash layer within the top of ammonite zone *Dactylioceras tenuicostatum* of Palquilla section, Peru brackets the first episode of faunal extinction within the initial phase of K-LIP volcanism, and places a maximal age for the P-T boundary at 183.5 Ma (Sell et al., 2014). This time interval is synchronous with major negative carbon-isotope excursions recorded in Boreal, Tethyan, and North American realms (Bodin et al., 2010; Them et al., 2018). The second (main) phase of K-LIP volcanism reportedly induced the second wave of faunal extinctions, another globally prominent negative carbon isotope excursion, and a globally recorded Os isotope seawater excursion (Them et al., 2017). At this time, sea level transgressions reached a maximal height for the Early Jurassic, which resulted in a synchrony of widespread anoxic deposition of organic-rich facies that culminated in the ammonite zone *Harpoceras falciferum* of the Early Toarcian, better known as the Toarcian Ocean Anoxic Event (T-OAE) (Gradstein, 2012; Haq, 2017; Jenkyns, 2010). The multi-phased volcanism of the K-LIP is postulated to have either (1) destabilized methane hydrates and/or (2) released thermogenic methane through sill-induced metamorphism of organic-rich sediments within the Karoo basin, which perturbed the global carbon cycle by releasing large quantities of carbon into the atmosphere (Hesselbo et al., 2000; Mazzini et al., 2010; Svensen et al., 2007). As a result, the global climate was forced into a hothouse state, which induced rapid silicate weathering and widespread anoxia of the oceans (Them et al., 2017).

Concurrent with the Late Pliensbachian and Early Toarcian events was the deposition of organic-rich facies of the Upper Radioactive Unit of the Gordondale Member and basal section of the Poker Chip Member, in the Panthalassa Ocean off the west coast of North America. Here we use Re-Os geochronology from organic-rich rocks of the Lower (subunit 1B/ PCP Ching well) and Upper Radioactive Unit of the Gordondale Member and basal Poker Chip Member (Dome Gordondale and Maclean Creek well) to expand upon previous literature findings on Late Pliensbachian and Early Toarcian geologic events.

6.2 Geological background

6.2.1 The Gordondale and Basal Poker Chip Member

The upper radioactive unit is an 8 m thick brown calcareous to argillaceous mudstone unit containing abundant fish fragments and macrofossil assemblages of *Ostrea*, pectinoid bivalves, *Inoceramus*, belemnoids, radiolarians and coccoliths. Subunit 1B of the Lower Radioactive unit is characterized as an 8-25 m thick dark brown calcarenite unit with abundant fish fragments, pectinoid bivalves, *Ochotochlamys*, and *Ostrea*. Other macrofossil assemblages include ammonites and belemnoids. Microfossil assemblages include: radiolarians and coccoliths. Subunit 3B of the basal Poker Chip member is characterized as a brown calcareous mudstone unit containing ammonite and coccoliths remains.

6.2.2 Biostratigraphy of the Upper (Subunit 3A), Lower (Subunit 1B) Radioactive unit, Middle Silty, and basal Poker Chip

Asgar-Deen et al. (2003) identified Early Toarcian ammonite specimens *Harpoceras* sp. cf. *subplanatum* (1218.055 m) and *Orthodactylites* sp*.* (PCP Ching; UWI = 6-32-78-5W6; depth = 1218.135 m) in subsurface strata of subunit 1B of the Lower Radioactive Unit of NW Alberta (Figure 6.1). Approximately 1 meter below these fossil occurrences is two *Ochotochlamys* bivalve fossils (1219.61 m) (Figure 6.1). A second *Dactylioceras* sp. ammonite specimen was recognized ~ 200 km SE of this location in subsurface strata of the Middle Silty Unit (Unit 2) of NW Alberta (UWI = 1-35-62-20W5; depth = 2026.65 m) (Asgar-Deen et al., 2003). Occurrences

of *H. subplanatum* are recorded in lower-to-middle Toarcian *Fibulatum* Subzone (*H. bifrons* zone) in NW Europe and Tethyan realms, whereas *Orthodactylites* sp. cf. and *Dactylioceras* sp. are abundant in lower Toarcian *Dactylioceras tenuicostatum* and *H. Falciferum* Zone of NW Europe, and therefore constrain the top of subunit 1B (Lower Radioactive unit) and the Middle Silty Unit to the Early Toarcian (Asgar-Deen et al., 2003). This is followed by the appearance of Late Toarcian ammonite specimen *Yakounia* sp. in subsurface strata of subunit 3A of the Upper Radioactive Unit (Dome Gordondale/UWI = 7-31-79-10W6; depth = 1539.1 m; Figure 4.2), with similar occurrences recognized approximately ~ 200 m SE of this location in subsurface basal Poker Chip Member strata (Subunit 3B; 2020.31 m; UWI = 6-9-66-24W5) (Asgar-Deen et al., 2003). However, the occurrence of *Harpoceras cf. falciferum, Dactylioceras* sp. cf. *semicelatum*, and *Dactylioceras commune* in basal Poker Chip strata overlying the marginal Red Deer facies Member further SE in outcrop at East Tributary in west-central Alberta, suggest a older, Early Toarcian, age, that correlates with international standard ammonite zone *D. tenuicostatum and H. serpentinum* zones of NW Europe (Them et al., 2016).

Calcareous nannofossils have also been recorded to co-occur with each these macrofossil assemblages in varying degrees of abundances ranging from rare, to rare-to-frequent, to frequent-to-common, and abundant (Figure 6.1) (Asgar-Deen et al, 2003). The greatest diversification and/or preservation of these appear in the top section of the Lower Radioactive Unit and sections of Unit 2. Of these microfauna, *Crepidolithus superbus* and *Discorhabdus ignotus* are most diagnostic of an Early Toarcian depositional age for subunit 1B of the Lower Radioactive Unit and Unit 2 that correlate with international standard boreal calcareous nannofossil zone NJ6, which is also consistent with intercalated co-appearances of Early Toarcian ammonites *H. subplanatum*, *Orthodactylites* sp., and *Dactylioceras* sp.
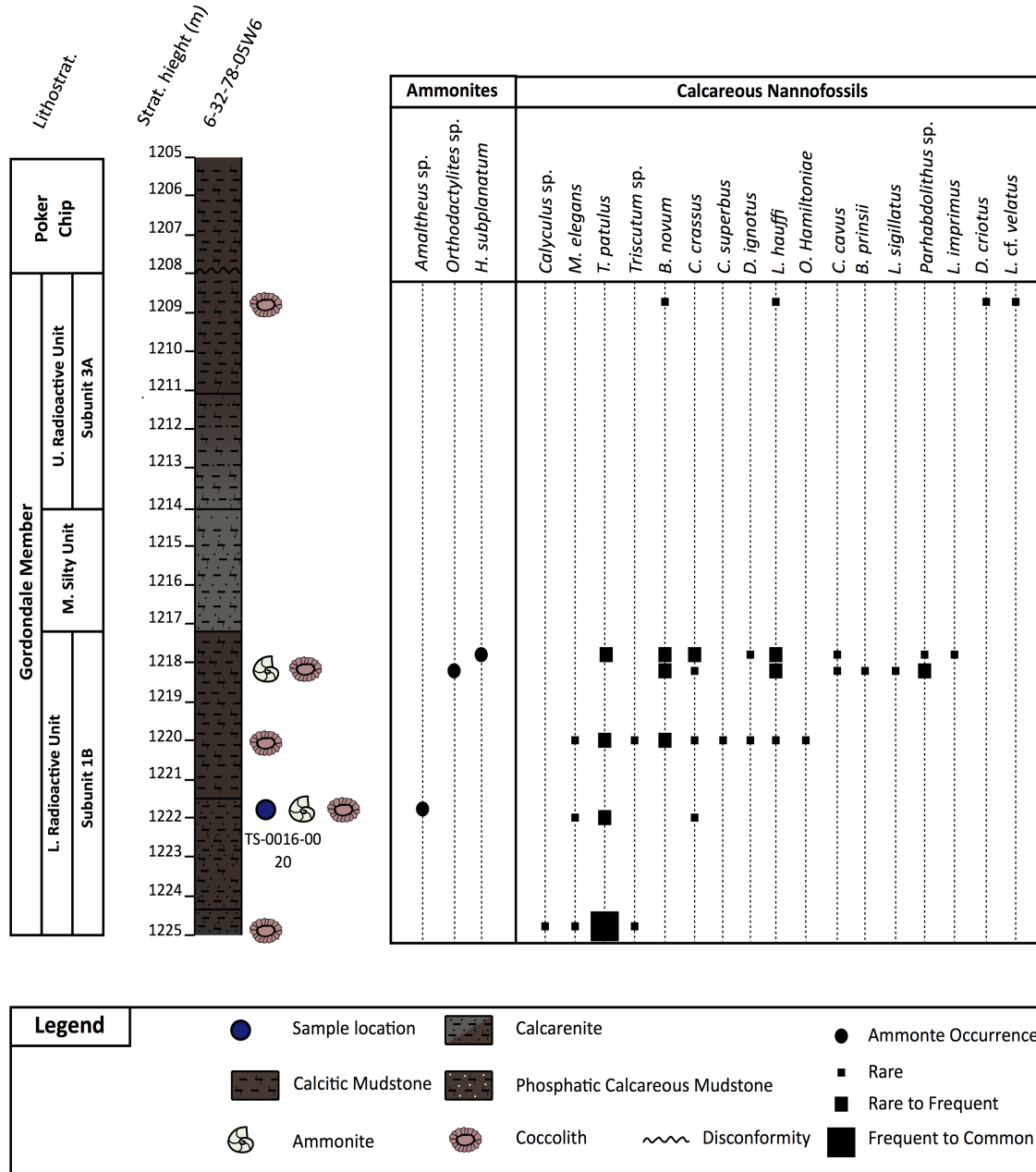
Figure 6.1 Biostratigraphy of the Gordondale (Subunit 1B, Lower Radioactive Unit and Subunit 3A, Upper Radioactive Unit) and Poker Chip Member (Subunit 3B) from well PCP Ching (UWI = 6-322-78-5W6). Sampling interval for Re/Os ORS chronostratigraphy is shown in blue. See Asgar-Deen et al. (2003) for detailed stratigraphy of PCP Ching and biostratigraphic characterization.

6.3 Methods

A complete summary of Re-Os methodology pertaining to the physical and chemical separation and data collection for samples described in this chapter can be found in section 3.1.1.

6.4 Results

6.4.1 Re and Os Concentrations and Isotopic Ratios

Rhenium and osmium concentrations and isotopic ratios are listed in Table 7 (see appendix). Rhenium and Osmium concentrations of well PCP Ching in the top section of subunit 1B of the Lower Radioactive Unit (UWI = 6-32-78-5W6; samples: TS0016-20; depth = ~ 1222 m) range from 210-311 ppb and 1090-1500 ppt and exhibit $^{187}Re/^{188}Os$ and $^{187}Os/^{188}Os$ isotopic ratios ranging from 1000-1800 and 3.2 and 6.2. Similar concentrations and isotopic ratios are found in wells Dome Gordondale and Maclean Creek of the Upper Radioactive Unit approximately ~ 1 m below the Gordondale-Poker Chip contact, with concentrations and ranging from a~ 160-475 ppb and 790-2580 ppt and $^{187}Re/^{188}Os$ and $^{187}Os/^{188}Os$ ratios ranging from 800-1900 and 3.1-6.4 (UWI = 7-31-79-10W6 and 13-28-73-21W6, depth = 1537.86 m, 1169.38 m). Approximately 1 m above the Gordondale-Poker Chip contact, in basal Poker Chip strata, Re and Os concentrations record generally lower values relative to those found in the Gordondale Member, with concentrations ranging from 87-138 ppb and 500 to 790 ppt, but exhibit similar $^{187}Re/^{188}Os$ and $^{187}Os/^{188}Os$ ratios, ranging from 960-1500 and 3.5-7.7 (UWI = 7-31-79-10W6 and 13-28-73-21W6; depth = 1537.15 m, = 1168.5 m). However, samples JT17-19203A and JT17-19203H remain enriched in Re (~ 235 ppb and ~ 149 ppb) and Os (~ 1245 ppt and ~ 1080 ppt) relative to other basal Poker Chip samples. Replicate analyses from each core varied by < ± 1 %.

In comparison to UCC Re and Os levels, the Gordondale (subunit 1B and subunit 3A) and Poker Chip Member are enriched in Re and Os by a factor of >1000. When compared to coeval

Late Pliensbachian and Toarcian shale beds of both Tethyan and western Pacific realms, Gordondale and Poker Chip samples also exhibit Re and Os enrichments, although not to the same scale as the UCC (Figure 6.2). For example, shales from Yorkshire and Mocha have Re and Os concentrations ranging from 0.7 to 40 ppb and 0.1 to 185 ppt, which translates to 0.7-8.42% and 0.02-8.33% of the Re and Os concentrations in Gordondale and Poker Chip samples (Cohen et al., 2004; Percival et al., 2016). Rhenium and Osmium concentrations of the coeval Red Deer member and overly Poker Chip member as reported by Them et al. (2017) exhibit larger concentrations than Yorkshire and Mocha but are still a fraction of those measured in the Gordondale Member and overlying Red Deer Member.
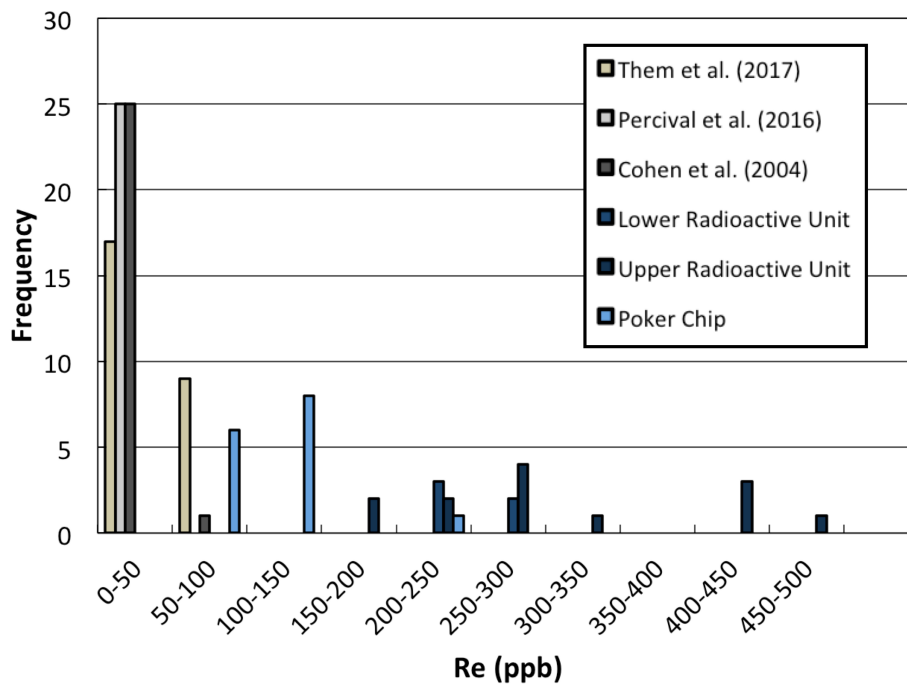
Figure 6.2 Rhenium distribution of Late Pliensbachian and Toarcian shales. The Gordondale Member (subunit 1B of the Lower Radioactive Unit and Upper Radioactive Unit) and the overlying Poker Chip shale Member exhibit the largest enrichments in Re relative to other coeval shale beds.

6.4.2 Re-Os Geochronology

Rhenium and Osmium isochrons were generated using the Microsoft add-in program *Isoplot* (Ludwig, 2012) and are presented in Figure 6.4 and 6.5, and frequency distributions of

each core's $^{187}Os/^{188}Os_i$ ratio are presented in Figure 6.3. Re-Os isochron regression of core TS0016-TS0019 (n = 4) of the Lower Radioactive Unit yielded a Model 1 age of 183.9 ± 1.3 Ma (MSWD = 1.08; 2σ) and an $^{187}Os/^{188}Os_i$ ratio of 0.505 ± 0.029. Regression of cores JT17-19204 (n =7) and JT17-19206 (n=6) from the Upper Radioactive Unit yielded two Model 3 ages of 181.2 ± 5.8 Ma (MSWD = 36; 2σ) and 184 ± 14 Ma (MSWD = 16; 2σ) and $^{187}Os/^{188}Os_i$ ratio of 0.42 ± 0.14 and 0.30 ± 0.41. Separate regressions of cores JT17-19203 (n =8) and JT17-19207 (n = 7) of the basal Poker Chip yielded a Model 3 age of 184± 12 Ma (MSWD = 37; 2σ) and a Model 1 age 182.3 ± 2.5 Ma (MSWD = 0.85; 2σ) and $^{187}Os/^{188}Os_i$ ratios of 0.53 ± 0.27 and 0.404 ± 0.041, respectively.
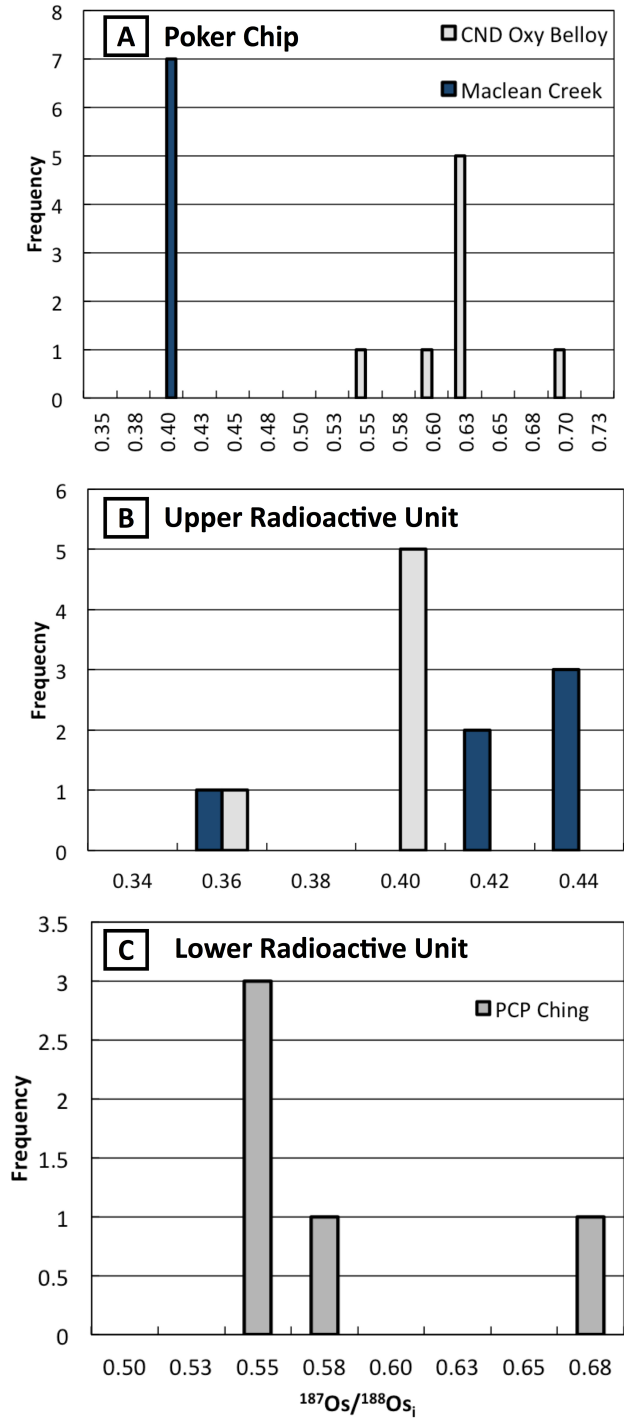
Figure 6.3 ^{187}Os/^{188}Os$_i$ distributions for samples selected for geochronology. Figure A corresponds to the Poker Chip (subunit 3B) member, whereas B and C, corresponds to the Upper Radioactive Unit (subunit 3A) and Lower Radioactive Unit (subunit 1B) of the Gordondale Member. ^{187}Os/^{188}Os$_i$ ratios were calculated using an assumed age of 183.9 Ma and 182.5 Ma for the lower Radioactive Unit (subunit 1B) and Upper Radioactive Unit of the Gordondale (subunit 3A), and 182.5 Ma for the Poker Chip (subunit 3B).
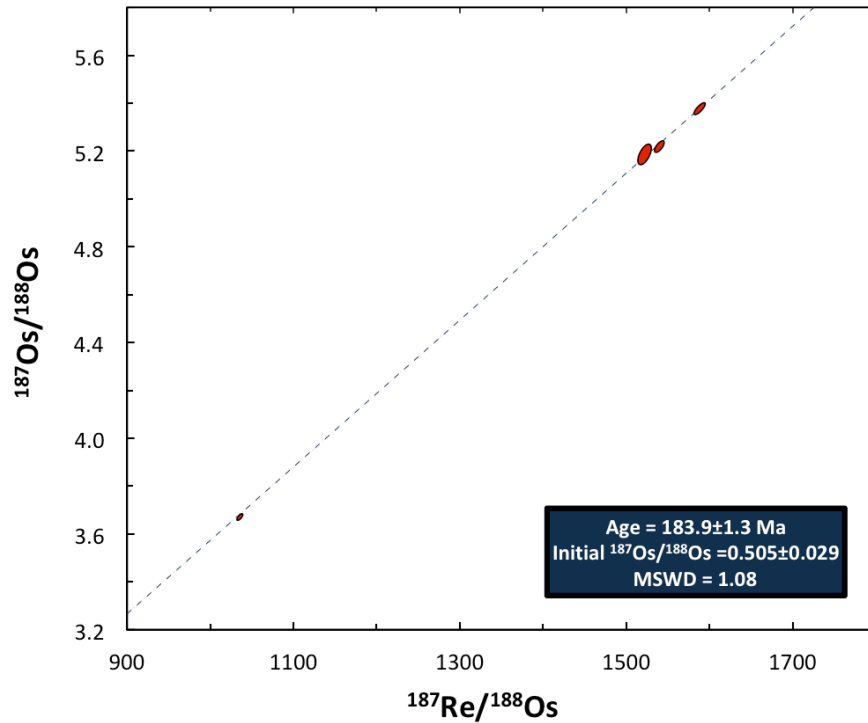
Figure 6.4 Rhenium-Osmium isochron of TS0016-TS0019 (n= 4) selected from the top of subunit 1B of the Lower Radioactive Unit of the Gordondale Member. Sample TS0020 was excluded from the regression due to Os_i deviations for trendline. Error ellipses are reported in 2σ notation and include error propagation from mass fractionation, oxygen corrections, and weighing errors. Re-Os isochron age was calculated using the [187]Re decay constant of Smoliar et al. (1996).
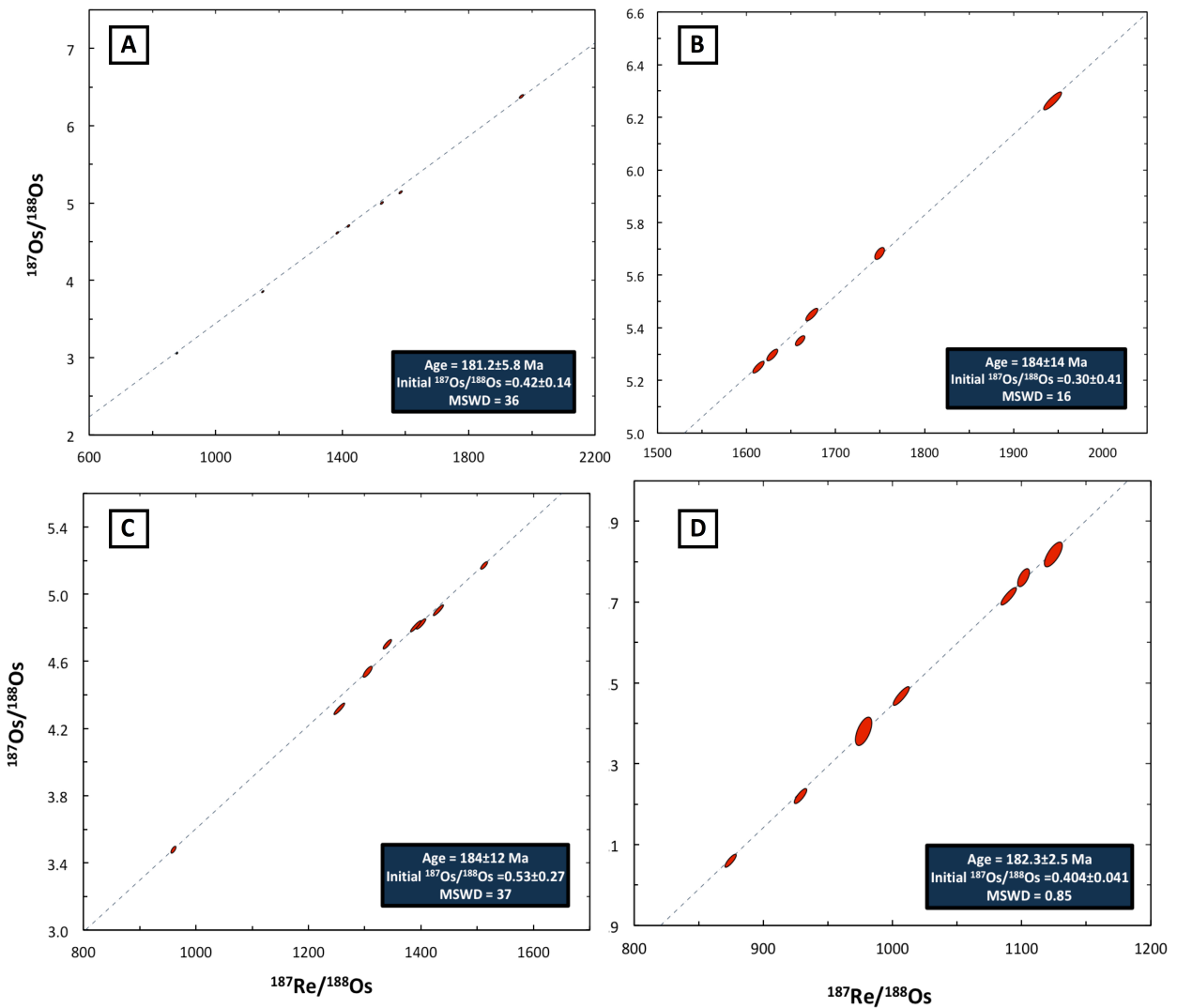
Figure 6.5 Rhenium-Osmium isochrons (A-D) for samples selected from Upper Radioactive Unit of the Gordondale Member (A and B) and subunit 3B of the Poker Chip Member (C and D). (A) JT17-19204 (n = 7), (B) JT17-19206 (n = 6), (C) JT17-19203 (n= 8), and (D) JT17-19207 (n = 7). Error ellipses are reported in 2σ notation and include error propagation from mass fractionation (Re only), oxygen corrections (Re only), blanks, and weighing errors. The ^{187}Re decay constant of 1.666 x 10^{-11} yr^{-1} was used (Smoliar et al., 1996).

6.4.3 Sr Concentrations and Isotopic Ratios

Whole rock strontium along with other major and trace element concentrations are reported in Table 5 (see appendix) and leached Sr isotopic ratios are reported in Table 4 and 6 (see appendix). Measured $^{87}Sr/^{86}Sr$ isotopic ratios and associated (2σ) uncertainties of samples JT17-19207A, JT17-19207B, TS0017, and TS0019 of the first leach were 0.707640 ± 0.000033, 0.707564 ± 0.000034, 0.707179 ± 0.000023, and 0.707194 ± 0.000065 and of the second leach were 0.707340 ± 0.000028, 707365 ± 0.000027, 0.707215 ± 0.000024, and 0.707209 ± 0.000021. The $^{87}Sr/^{86}Sr$ isotopic ratios of the second leach were less radiogenic than the first leach, as per Li et al. (2007), which suggests that diagenetic and/or detrital radiogenic overgrowth component was dissolved in the first leach but not the second. In order to quantify the contribution of this anomalous $^{87}Sr/^{86}Sr$ radiogenic fraction samples JT17-19207A and TS0017 was selected for repeat analysis of its $^{87}Sr/^{86}Sr$ isotopic ratio and Rb and Sr concentration (Table 3) between leaching phases 1 and 2 (for methodology see section 4.2). Strontium isotopic ratios and Sr and Rb concentrations of sample JT17-19207A-RPT for the first leach was 0.707573 ± 0.000040 (2σ), 10053.01 ppm, 189.38 ppm, and 0.707364 ± 0.000022 (2σ), 24814.89 ppm, and 171.60 ppm in the second leach. Strontium isotopic ratios and Sr and Rb concentrations of sample TS0017-RPT for the first leach was 0.707244 ± 0.000029 (2σ), 29841.58 ppm, 194.18 ppm, and 0.707230 ± 0.000027 (2σ), 62438.69, and 174.32 ppm in the second leach. By using the Sr and Rb concentrations the calculated $^{87}Rb/^{86}Sr$ ratios of samples JT17-19207A-RPT and TS0017-RPT for the first leach was 0.0793 and 0.0274 and 0.0291 and 0.0117 for the second leach. Employing the $^{87}Rb-^{87}Sr$ isochron equation in combination with the measured $^{87}Sr/^{86}Sr$ ratio, the calculated $^{87}Rb/^{86}Sr$ ratio, and an assumed age of 182.3 Ma (Re-Os data) for sample JT17-19207A-RPT and 189.3 Ma (Re-Os data) for sample TS0017-RPT the $^{87}Sr/^{86}Sr_i$ ratio of 0.707367 ± 0.000040 and 0.707173 ± 0.000029 was calculated for the first leach and a $^{87}Sr/^{86}Sr$ ratio of 0.707289 ± 0.000022 and 0.707200 ± 0.000027 was calculated for the second leach (Figure 6.6).
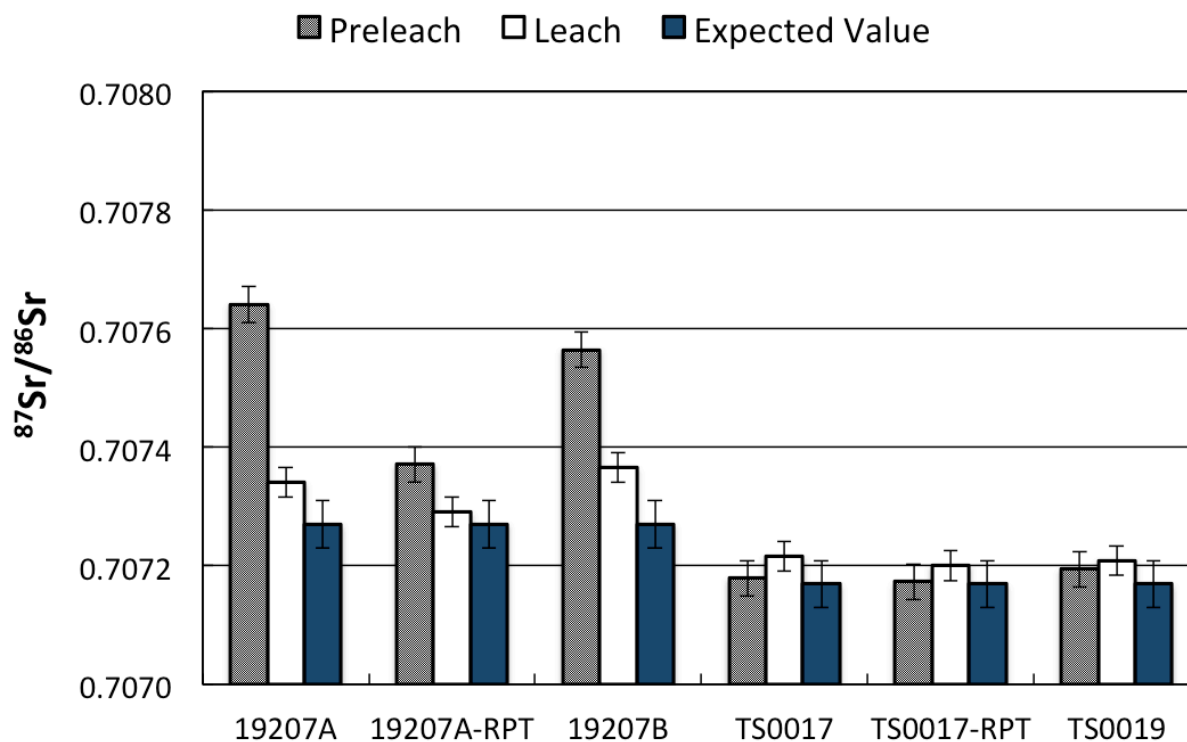
Figure 6.6 Preleached and leached ^{87}Sr/^{86}Sr isotopic compositions Gordondale (TS0017/TS0019 of subunit 1B of Lower Radioactive Unit) and Poker Chip (JT17-19207A/JT19207B) samples compared to expected values of contemporaneous seawater based off Re-Os age results. The ^{87}Sr/^{86}Sr isotopic composition of repeat (RPT) analysis includes the ^{87}Rb/^{86}Sr correction as described in section 6.4.3.

6.5 Discussion

6.5.1 Re-Os Age Significance

Assessing the legitimacy of radioisotopic dates is contingent on the axiomatic assumptions inherent in radioisotopic dating, and whether they are justly satisfied. In the case of the Re-Os ORS system this requires (1) that the ORS system remained isotopically closed since sediment deposition (t > 0), (2) uniformity in the ^{187}Os/^{188}Os ratio at the time of sediment deposition (t = 0), and (3) variability in ^{187}Re/^{188}Os at the time of sediment deposition in order

to yield variability in the $^{187}Os/^{188}Os$ ratios at present day. Regressions of TS0016-19 and JT17-19207, which yielded biostratigraphically consistent Late Pliensbachian to Early Toarcian ages with MSWD values at or below unity, provide strong indications that these assumptions were maintained. For example, the most conclusive evidence for their maintenance is shown in core TS0016-0019 (with the exclusion of sample TS0019) by the agreement between the Late Pliensbachian-Early Toarcian age obtained (183.9 ± 1.3 (0.71%) Ma [MSWD = 1.08]) and Early Toarcian ammonite specimens overlapping Boreal ammonite zone *D. tenuicostatum* and *H. falciferum* (~ 183.7-180.5 Ma) ~ 4 m above this sampling interval (Ogg et al., 2016). Whilst core JT17-19207 is not directly constrained biostratigraphically in Poker Chip strata at PCP Ching in NW Alberta, *Harpoceras* sp. and *Dactylioceras* sp. in Poker Chip strata at East Tributary in west-central Alberta and Toarcian ammonites elsewhere, indirectly support an Early Toarcian age overlapping Boreal ammonite zone *H. falciferum* (~ 182.5-180.5 Ma) (Ogg et al., 2016; Them et al., 2016).

Assigning age significance to cores JT17-19204, -19206, and -19203 is slightly more problematic due to probable divergence from one or more of the axioms relating to Re-Os ORS dating. For example, each core yielded ages with relatively large uncertainties (3.2-7.6%) and MSWD's that exceed unity (16-37). And although their ages do agree with their stratigraphic positions – providing some age significance, the large uncertainties hinder their precise temporal resolution. The reason for the large uncertainty and MSWD appears to be intimately tied to variability in the $^{187}Os/^{188}Os_i$ between samples (Figure 6.3). And although open-system behaviour, a probably secondary source of age imprecision, cannot be conclusively eliminated, the precise age information obtained elsewhere in Gordondale (TS0016-TS0019) and Poker Chip (JT17-19207) strata point towards variability in the $^{187}Os/^{188}Os_i$ between samples as the more likely of the two hypotheses. For example, by eliminating 19203B, -C and -F, from the regression analysis of JT17-19203 (n =5) and JT17-19206H from the regression analysis of JT17-19206 (n =5) - on the grounds of $^{187}Os/^{188}Os_i$ variability – yields a more precise age of 182.5 ± 1.6 (0.9%) Ma (MSWD = 0.83; $^{187}Os/^{188}Os_i$ of 0.562 ± 0.036) and 182.7 ± 7.3 (4.0%) Ma (MSWD = 2.7; $^{187}Os/^{188}Os_i$ of 0.36 ± 0.21) is obtained, whilst maintaining stratigraphic coherency.

When comparing age information and $^{187}Os/^{188}Os_i$ ratios obtained from cores analyzed above and below the Gordondale-Poker Chip Member contact (Maclean Creek or Dome Gordondale wells), it also becomes apparent that these stratigraphic units are not demarcated by a period of non-deposition, as originally hypothesized by Asgar-Deen et al. (2004), but share sediment continuity. For example, a comparison of JT-19206 (Upper Gordondale) to JT-19207 (basal Poker Chip) of Maclean Creek shows that both cores broadly agree within age (182.7 ± 7.3 (4.0%) Ma and 182.5 ± 2.3 (1.4%) Ma), but more importantly have consistent individual $^{187}Os/^{188}Os_i$ values (0.4-0.45) in a time when the seawater Os isotopic composition was intermittently fluctuating (Them et al., 2017). A similar case can be made for JT17-19204 (Dome Gordondale; Upper Radioactive Unit; Gordondale), which contains a mean $^{187}Os/^{188}Os_i$ value of 0.4 - consistent with the other two cores. Regressing cores JT17-19206 and JT17-19207 (with the exclusion of JT17-19206B/C/H – Figure 6.4) together reaffirms this conclusion, which yields a Model 1 age of 179.39 ± 0.60 (0.3%; MSWD = 1.3; n = 10) Ma and $^{187}Os/^{188}Os_i$ of 0.452 ± 0.012 (Figure 6.7/6.8). This Re-Os age positions the Gordondale-Poker Chip contact in Late Toarcian North American ammonite zone *Yakounensis* sp. (180.1 + 0.7/- 3.0 Ma; chronogram estimate) and Boreal/Tethyan ammonite zone *D. levesquei*, which is consistent with the incomplete specimen *Yakouina* sp. observed ~ 0.5 m below core JT17-19204 (Figure 4.2) of Dome Gordondale and the measured seawater $^{87}Sr/^{86}Sr$ ratio of 0.707290 ± 0.000022 (JT17-19207A), which agrees within uncertainty of the global contemporaneous seawater Sr composition of 0.70727-0.70730 (Gröcke et al., 2007; Ogg et al., 2016; Pálfy et al., 2000).

On a regional scale within the WCSB, a Late Toarcian depositional age interpretation for the Gordondale-Poker Chip contact obtained from two distinct subsurface localities (Dome Gordondale and Maclean Creek) in NW Alberta implies that the current Gordondale-Poker Chip datum defined elsewhere by Asgar-Deen (2003) and Asgar-Deen et al. (2003/2004) likely aslo corresponds to a Late Toarcian depositional time interval. Recently, however, there has been a proposal to shift the Gordondale-Poker Chip contact locally within Maclean Creek (UWI = 13-28-73-21W5) well from ~ 1169 m to ~ 1146 m based off gamma ray log readings (Asgar-Deen, 2018, personal communications). However, efforts to shift the Gordondale-Poker Chip datum in certain subsurface wells, but not others, should be proceeded with caution, since this would

likely correspond to a different interval of geologic time, resulting in regional age discrepancies for the Gordondale-Poker Chip datum.
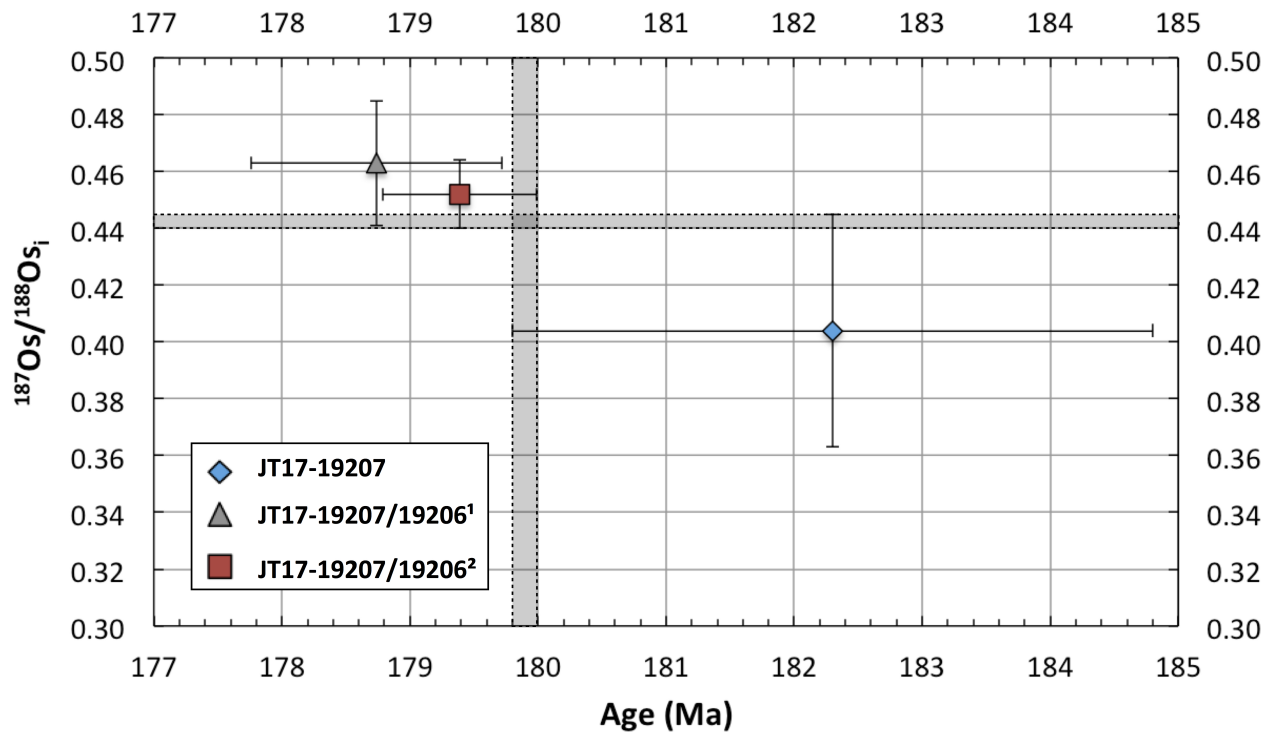
Figure 6. 7 Re-Os Isochron age and $^{187}Os/^{188}Os_i$ ratio comparison between cores JT17-19207, JT17-19207/19206[1] (exclusion of data point JT17-19206H), and 19207/19206[2] (exclusion of data points JT17-19206B/C/H) at the Poker Chip-Gordondale Member contact at Maclean Creek well. Light Grey bars indicate areas of overlapping uncertainty. Agreement within uncertainty of both Re-Os ages and $^{187}Os/^{188}Os_i$ ratios of JT17-19207 and JT17-19207/19206[2] (dark grey bar) suggests that the age produced from Re-Os Isochron 19207/19206[2] is the justifiable, and henceforth assumed, age demarcating the Gordondale-Poker Chip boundary.
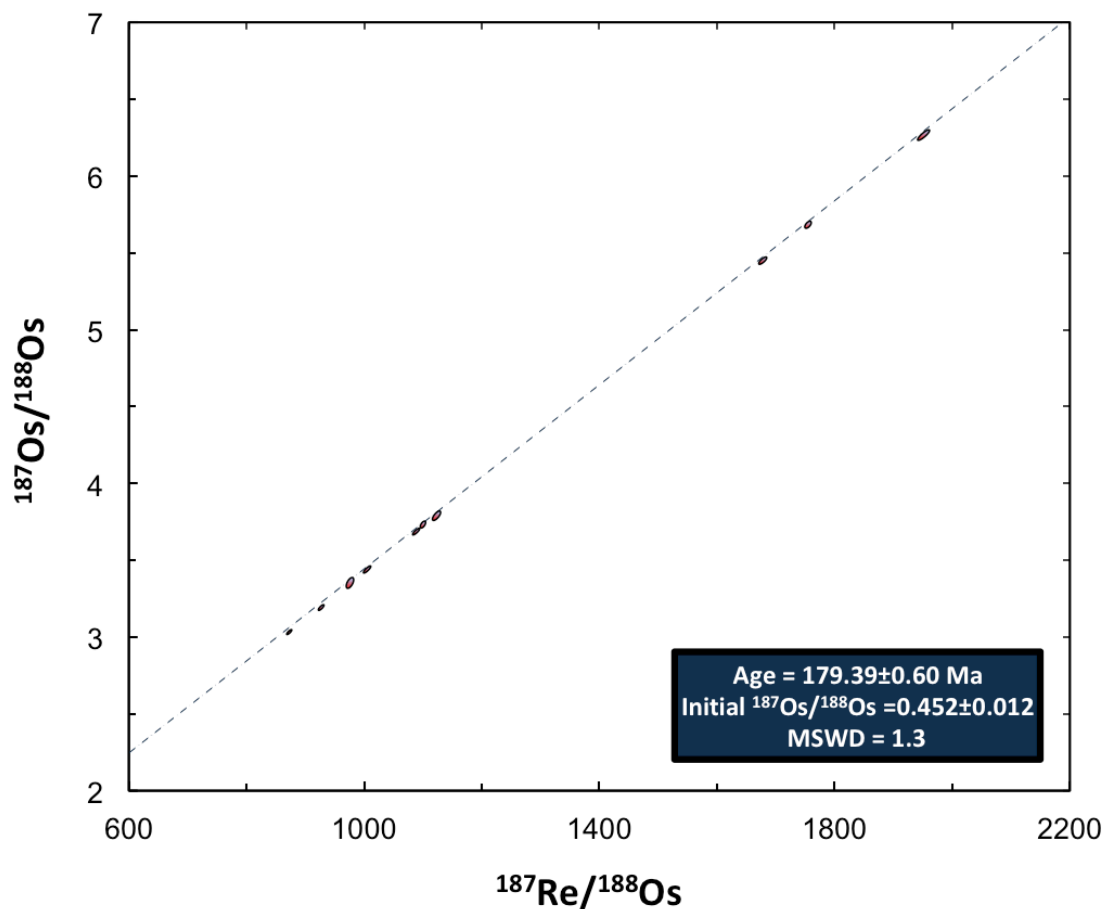
Figure 6.8 Re-Os isochron of the Gordondale-Poker boundary (Well: Mclean Creek; JT17-19206 and JT17-19207; n = 10) (with the exclusion of JT17-19206B/C/H). Error ellipses are reported in 2σ notation and include error propagation from mass fractionation, oxygen corrections, and weighing errors. The ^{187}Re decay constant of 1.666 x 10^{-11} yr^{-1} was used (Smoliar et al., 1996).

6.5.2 Limits Towards Obtaining High-precision Early Toarcian Re-Os ORS Ages

Cohen et al. (1999) made the first attempt at obtaining high-precision Re-Os ORS depositional ages for Toarcian (*D. tenuicostatum* ammonite zone) black shales. Regression of 9/10 black shale samples of Port Mulgrave, Yorkshire, UK yielded an age of 181 ± 13 Ma (MSWD = 17) and ^{187}Os/^{188}Os$_i$ of 0.80 ± 0.07. The imprecision in the Re-Os age was argued to reflect open system characteristics and/or variation in the ^{187}Os/^{188}Os$_i$ ratios (Cohen et al., 1999). A second attempt at dating Toarcian black shales of *H. falciferum* ammonite zone of the same stratigraphic unit yielded another imprecise, although improved, Re-Os isochron with a

regression age of 178.2 ± 5.6 Ma (MWSD = 3) and $^{187}Os/^{188}Os_i$ of 0.4 ± 0.15. The improvement in age precision was predominantly the result of a 5-fold increase in the $^{187}Re/^{188}Os$ ratio variation (700-2200) over the sampling interval, since the percent variance in the $^{187}Os/^{188}Os_i$ of the second regression (9.66%) exceeded that of the initial regression (6.11%). The $^{187}Os/^{188}Os_i$ variance of both regressions, which ultimately stymied obtaining a high-precision Re-Os age of *H. falciferum* ammonite zone, was argued by MacArthur et al. (2009) to result from a progression towards basin restriction in early Toarcian anoxic settings. Rapid draw down of Re and Os from the water column depletes isolated marine reservoirs of dissolved Re and Os and makes organic-rich sediment susceptible to record subtle changes in the $^{187}Os/^{188}Os$ of the water column as Os flux delivery to the basin fluctuates. This was most prominently observed in anoxic sediment of *D. tenuicostatum* ammonite zone of Yorkshire, UK, which experienced an ephemeral increase of seawater $^{187}Os/^{188}Os$ towards more radiogenic values (from ~0.4 to ~1.0) over a discrete (<5 m) sedimentary interval (Cohen et al., 2004). This drawdown effect was first observed by Turgeon et al. (2007) in a shale package (WVC777) below the Frasnian-Famennian boundary, and has subsequently been observed in modern restrictive basins, such as the Black Sea (Georgiev et al., 2011). The mode for inferring basin restriction is commonly derived from the slope of a Mo (or Re and Os) vs. TOC plot (McArthur et al., 2008). Less restrictive basins, such as Saanich Inlet, are steep slope (m = 45) prone, whereas more restrictive basins, such as the Black Sea, are shallow slope (m = 5) prone [see insert in Figure 6.9] (Georgiev et al., 2011). This relationship forms from restrictive basins having (1) high rates of organic matter preservation and (2) high uptake rates of redox-sensitive metals into organic-rich sediment. Therefore the slope will pivot towards the abscissa as basin restriction decreases the opportunity for resupply of redox-sensitive metals into the basin and invariably increases (1) and (2).

Similarities between $^{187}Os/^{188}Os_i$ variability inherent in the regression analyses of Cohen et al. (1999; 2002) and Gordondale (subunit 1 A Lower Radioactive Unit and Upper Radioactive Unit) and Poker Chip reported here seem to support MacArthur et al. (2009) thesis of more widespread basin restriction in the Early Toarcian (*D. tenuicostatum* and *H. falciferum* ammonite zone). Although accurately vindicating this hypothesis for Gordondale/Poker Chip

strata requires a full assessment of Re and ^{192}Os concentrations relative to TOC content of each sample (as per MacArthur et al. (2009) basin restriction proxy), which remains unavailable. Alternatively, we can turn to the study of Them et al. (2017) that investigated the seawater Os isotopic composition through the Pliensbachian-Toarcian boundary interval of the marginal Red Deer Member and overlying Poker Chip Member located in west-central Alberta for additional insight into basin restriction in the WCSB during the Early Jurassic. Plots of Re/TOC and ^{192}Os/TOC (Figure 6.9; m_x = slope of x/TOC) illustrate that Re and ^{192}Os co-varies with TOC throughout the *A. margaritatus* (m_{Re} = 100; m_{Os} =155) and *D. tenuicostatum* (m_{Re} = 35; m_{Os} = 72) ammonite zone of the Late Pliensbachian and Early Toarcian, which suggests a less restrictive period relative to the *P. spinatum* ammonite zone of the late Pliensbachian where the Re and ^{192}Os slope equals ~ 9 and 15. In contrast, the *H. falciferum* ammonite zone records a period of extreme restriction (m_{Re} = -0.5; m_{Os} = 6) at the depth interval of 12.0 to 15.3 m, which then transitioned into a less restrictive state (m_{Re} = 17; m_{Os} = 32) at a depth interval of 16.7 to 20.5 m in the *H. bifrons* ammonite zone. These observations suggest that marginal depositional settings of the WCSB experienced periods of both basin restriction and non-restriction. Whether periods of basin restriction observed in the marginal setting (Red Deer and overlying Poker Chip Member) of the WCSB expanded seaward in the basinal sections (Gordondale Member and overlying Poker Chip) of the WCSB remains unknown. However, ^{187}Os/^{188}Os$_i$ variability observed in cores JT17-19203, 19204, 19206 and TS0016-19 tentatively suggests basin restriction was operating to some degree.

One problem that limits the use of Them et al. (2017) chemostratigraphic data to interpret the age imprecision of the cores in this study is that the sampling strategy of Them et al. (2017) was adopted to accommodate Os isotope stratigraphy (meter scale), whereas the sampling strategy here was adopted to accommodate geochronology (cm scale). Hence, the data of Them et al. (2017) are most informative of low-resolution trends in basin restriction across Late Pliensbachian and Early Toarcian stages and least informative of high-resolution trends.
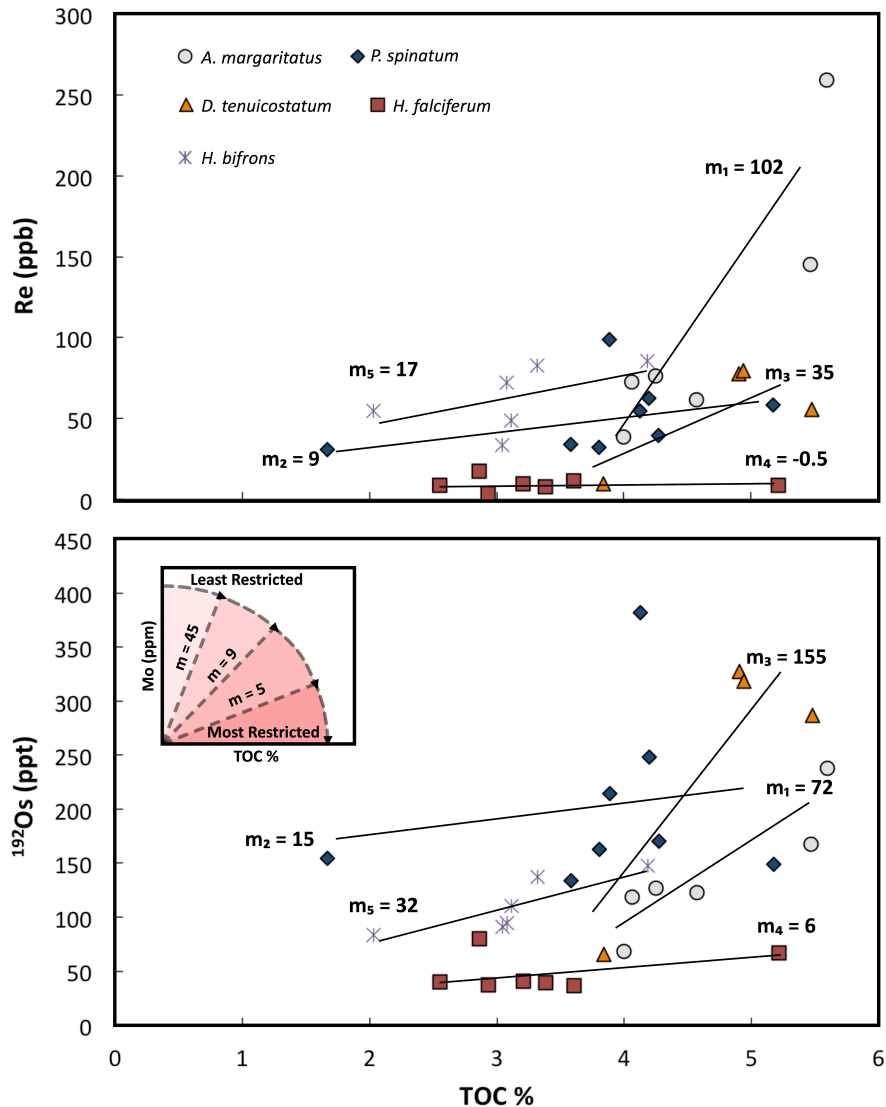
Figure 6.9 Re and ^{192}Os data plotted against TOC of the Red Deer and Poker Chip Member (Them et al., 2017). Sampling intervals range from Boreal ammonite zone *A. margaritatus* (grey circles) and *P. spinatum* (blue diamonds) of the late Pliensbachian to *D. tenuicostatum* (orange triangles), *H. falciferum* (red squares), and *H. bifrons* (light blue crosses) of the early Toarcian. The insert shown in plot ^{192}Os/TOC depicts the predicted relationship between Mo vs TOC and basin restriction. The small black arrows point in the direction that the slope (m) pivots as a basin moves towards increased restriction. Therefore, a slope of 45 – as seen in Saanich Inlet – is less restrictive than a slope of 9 or 5 as observed in the Framvaren Fjord and the Black Sea. Due to reciprocal geochemical affinities, the slopes of Re/TOC and ^{192}Os/TOC will follow the same general trend.

6.5.3 Pliensbachian-Toarcian Boundary Age?

Pálfy et al. (2000) interpolated the age of the Pliensbachian-Toarcian (P-T) stage boundary to 183.6 + 1.7/- 1.1 Ma using precise U-Pb zircon dates from Early Jurassic and Late Toarcian lava flows in British Columbia, Canada. Although this age estimate is an indirect measure of the P-T stage boundary, it still remains in statistical agreement with more recent direct estimates employing single-grain U-Pb zircon geochronology of interstratified volcanic ash layers. Mazzini et al. (2010) obtained the first high-precision U-Pb zircon ages of two tuff layers above (6.6 m and 26.1 m) an inferred P-T boundary section in the Neuquen Basin of Argentina. By assuming a linear sediment deposition rate coupled with Monte Carlo error propagation, Mazzini et al. (2010) estimated a P-T boundary age of 182.16 ± 0.6 Ma coincident with the base of a negative-CIE. Approximately 6 m above this are Early Toarcian invertebrate fauna. However, a lack of robust ammonite biomarkers prevented global biostratigraphic correlation with Tethyan and/or Boreal biochrons that would otherwise reaffirm Mazzini et al. (2010) conclusions. Sell et al. (2014) provided a more reliable P-T boundary estimate by utilizing both high-precision geochronology and biostratigraphy within the Palquilla section of Southern Peru. Uranium-Lead zircon dating of an interstratified tephra ash layer contiguous with Early Toarcian boreal ammonite zone *D. tenuicostatum* yielded an age of 183.22 ± 0.25 Ma (Sell et al. 2014). From this the authors concluded that the P-T stage boundary must be older than 183.5 Ma, which has garnered acceptance from the *Concise Geologic Time Scale* (Ogg et al., 2016).

Although our direct Re-Os ORS age of 183.9 ± 1.3 Ma agrees within uncertainty with Sell et al. (2014) P-T boundary estimate, resolving this age to a single Late Pliensbachian or Early Toarcian stage remains challenging. Re-Os age uncertainty brackets subunit 1B (depth = ~ 1221 m) of the Lower Gordondale Member in PCP Ching well to Upper Pliensbachian ammonite zone *A. margaritatus* and Lower Toarcian ammonite zone *H. falciferum* of Tethyan realms (Ogg et al., 2016). The upper age estimate agrees with Early Toarcian ammonite specimens *Orthodactylites* sp. and *Cleviceras exaratum* of standard boreal ammonite zone *D. tenuicostatum* and *H. falciferum* located 4 m above TS0016-19 sampling interval (depth = ~ 1221 m) (Asgar-Deen et al., 2003). These early Toarcian ammonites follow the tail end of a negative-CIE (depth = 1220

m - 1218 m) identified by Them et al. (2018) as the globally recorded T-OAE carbon isotope excursion coincident with Early Toarcian Boreal ammonite zone *D. tenuicostatum* and *H. falciferum* and North American ammonite zone *kanense* (Them, 2016; Them et al., 2018). By comparison, the lower age estimate agrees with Late Pliensbachian ammonite specimen *Amaltheus* sp. of standard boreal ammonite zone *A. margaritatus* that intersects TS0016-19 sampling interval (supplementary data of Them et al., 2018). The proximity of ammonite specimen *Amaltheus* sp. to core TS0016-19, therefore, shifts age plausibility towards the lower end of the age uncertainty estimate. This is further corroborated by agreement, within uncertainty, of the seawater $^{87}Sr/^{86}Sr$ composition of core TS0016-19 (TS0017-RPT-L1 = 0.707173 ± 0.000029) and belemnite samples of Yorkshire, UK corresponding to Late Pliensbachian ammonite zone *A. margaritatus* (0.707160-0.707188) (McArthur, et al. 2000) (Figure 6.10). However, a Late Pliensbachian age interpretation is complicated by (1) disagreement in the seawater $^{187}Os/^{188}Os$ isotopic composition of core TS0016-19 ($^{187}Os/^{188}Os$ = 0.505 ± 0.029) and Red Deer Member samples corresponding to *A. margaritatus* ammonite zone ($^{187}Os/^{188}Os$ = 0.18-0.29 ± 0.04) of the WCSB (Them et al., 2017) and (2) agreement, within uncertainty, of the seawater $^{187}Os/^{188}Os$ isotopic composition recorded at the P-T boundary of Tethyan realms ($^{187}Os/^{188}Os$ = 0.48-0.52) (Cohen et al., 2004; Percival et al., 2016).

Evidence suggests that the Red Deer Member was episodically transitioning between restrictive and non-restrictive basin states during the Late Pliensbachian and Early Toarcian (see section 6.5.2). The resulting effect could have been Os isotopic heterogeneities developing coastward in the marginal (Red Deer Member) sections of the WCBS, whereas seaward in the basinal (Gordondale Member) sections of the WCBS the seawater Os isotopic composition reflected the open ocean. Examination of the seawater Os isotopic composition of calcareous mudrock samples of Mochras borehole from Cardigan Bay, Wales, UK, broadly supports this hypothesis. For example, seawater $^{187}Os/^{188}Os$ values of Mochas samples of Late Pliensbachian *P. spinatum* ammonite zone, which precedes *A. margaritatus* ammonite zone, ranges from 0.28 and 0.52. In addition, seawater $^{187}Os/^{188}Os$ near the base of *P. spinatum* ammonite zone of Mochras borehole is 0.55 (Figure 6.10), which is similar, albeit slightly higher, than the seawater $^{187}Os/^{188}Os$ of 0.505 ± 0.029 measured from core TS0016-19. Although this evidence lends

credibility to the basin restriction hypothesis, it fails to account for the fact that the Re/TOC and ^{192}Os/TOC trends suggest that *A. margaritatus* ammonite zone was less restrictive than other ammonite zones in the Red Deer Member.
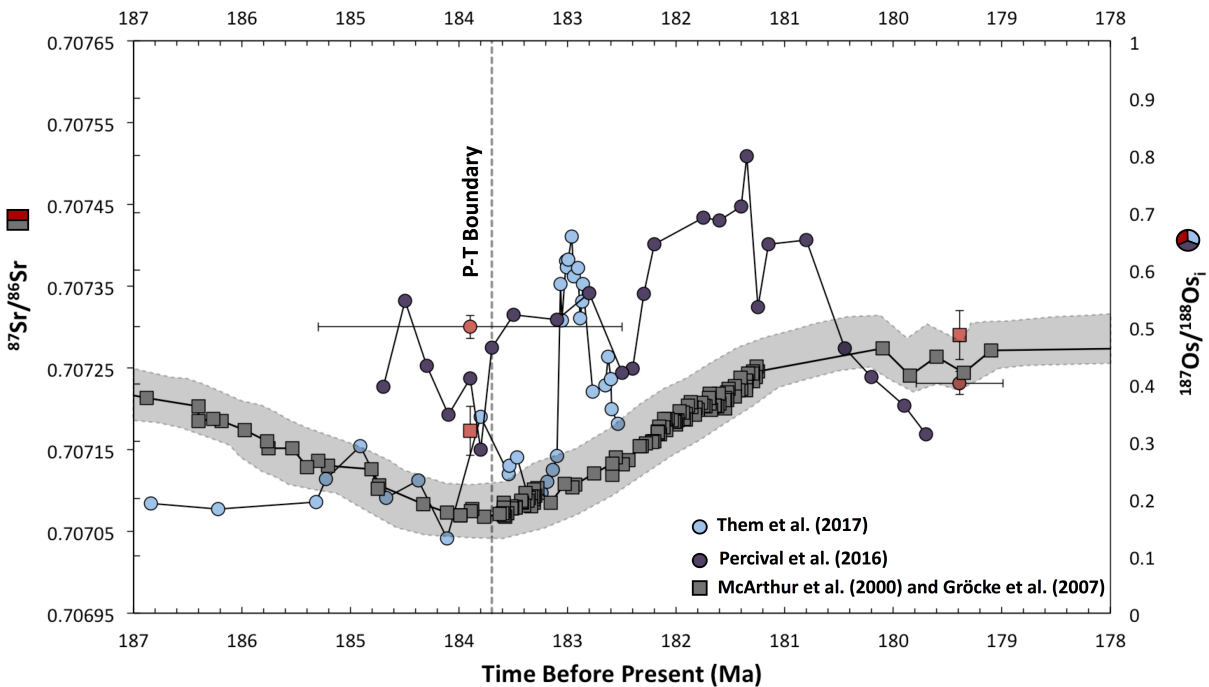
Figure 6. 10 Early Jurassic seawater Os and Sr curve. Red circles and squares correspond to ^{187}Os/^{188}Osi and ^{87}Sr/^{86}Sr ratios of sample cores (TS0016-0019 and JT17-19206/19207) from subunit 1B of the Lower Radioactive Unit and Upper Radioactive Unit of the Gordondale Member and basal Poker Chip Member. The seawater ^{87}Sr/^{86}Sr curve (shown in grey squares/bar) is derived from belemnites of Yorkshire, UK (McArthur et al., 2000), while the seawater ^{187}Os/^{188}Os curve (shown as dark/light blue circles) is derived from Western North American and Tethyan ORS (Percival et al., 2016; Them et al., 2017).

6.5.4 Late Toarcian Age Revisions

The Late Toarcian stage is divided into North American ammonite zone *Hillebrandti* sp. and *Yakounensis* sp. and equivalent NW European ammonite zone *G. thouarsense and D.*

levesquei. The Concise Jurassic Time Scale (CJTS) brackets the latter to ~ 176 to 174.2 Ma, which remains broadly consistent with previous age estimates outlined in the GST2012 (Ogg et al. 2016; Gradstein, 2012). Both published age estimates, however, remain in conflict with Palfy et al. (2000) chronogram estimate of 180.1 +0.7/-3.0 Ma for the boundary of North American ammonite zone *Hillebrandti* sp. – *Yakounensis* sp. Sell et al. (2014) reports similar age discrepancies from GTS2012 in the Palquilla stratigraphic section in southern Peru for the Late Toarcian. For example, U-Pb zircon analysis of a volcanic ash layer interstratified within Late Toarcian Boreal ammonite zone *G. thouarsense* and located ~ 5 m above ammonite specimen *Yakounia* sp. yielded an age of 180.35 ± 0.39 Ma. Sell et al. (2014) U-Pb age agrees both within uncertainty of Palfy et al. (2000) original chronogram and our Re-Os age of 179.39 ± 0.60 Ma for the Gordondale-Poker Chip contact of Maclean Creek (Figure 6.5). An impartial ammonite impression identified by Asgar-Deen et al. (2004) as *Yakounia* sp. located ~ 0.5 m below the G-PC contact at Dome Gordondale (section 4.1.1 Figure 4.2) is also analogous in form to the Late Toarcian ammonite specimen identified by Sell et al. (2014). Furthermore, the seawater Sr composition of 0.707290 ± 0.000022 at the Gordondale-Poker Chip contact of Maclean Creek agrees within uncertainty of the seawater Sr values of belemnites of the Queen Charlotte Islands, British Columbia, Canada of North American ammonite zone boundary *Hillebrandti* sp. – *Yakounensis* sp. (~0.707280) and belemnites of NW Europe of Boreal ammonite zone *G. thouarsense and D. levesquei* (~ 0.70730) (Gröcke et al. 2007; Jenkyns et al., 2002). Each of these evidences reported here suggest that the age projections for NW European ammonite zone *G. thouarsense and D. levesquei* reported by Ogg et al. (2016) and Gradstein (2012) require age revisions.

6.6 Conclusion

Sample cores of subunit 1B of the Lower Radioactive Unit (TS0016-0019) and basal Poker Chip (JT17-19207) yielded Modal 1 Re-Os ages of 183.9 ± 1.3 Ma and 182.3 ± 2.5 Ma and $^{187}Os/^{188}Os_i$ ratios of 0.505 ± 0.029 and 0.404 ± 0.041, which correspond to Late Pliensbachian and Early Toarcian ages. The seawater $^{87}Sr/^{86}Sr$ composition of these cores reflects contemporaneous seawater Sr isotopic composition. By contrast, $^{187}Os/^{188}Os_i$ variability

compromised age precision of cores from the Upper Radioactive Unit of the Gordondale (JT17-19204, 19206) and basal Poker Chip (JT17-19203). Re-Os Isochron JT17-19207/19206[2] (exclusion of JT17-19206B/C/H) yielded a high precision Early Toarcian age of 179.39 ± 0.60 and $^{187}Os/^{188}Os_i$ ratio of 0.452 ± 0.012 for the Gordondale-Poker Chip contact.

7 | Extraction of Re and Os from ORS by Hot and Cold Water

7.1 Introduction

Understanding how post-depositional fluids interact with and influence the Re-Os systematics of organic-rich rocks is important for delineating the scope of application of the Re-Os ORS chronometer. Previous research has documented the overall sensitivity of Re-Os systematics of ORS to chemical weathering in the exogenic environment and fluid-rock interaction during diagenesis (Georgiev et al., 2011; Kendall et al., 2009; Yang et al. 2009). Here we expand up this previous literature by exploring the effects of Re and Os mobility in organic-rich rocks by hot and cold water under experimental conditions.

7.3 Experimental Techniques

7.3.1 Samples

Powder aliquots of geological reference material SBC-1-0011 (USGS) were analyzed for Re and Os concentrations and isotopic ratios. SBC-1 is characterized as marine shale of the Brush Creek Member of the Lower Conemaugh Group of the Glenshaw Formation of Pennsylvanian age (Wilson, 2012). Mineralogically, SBC-1 is dominated by quartz, various clays – muscovite, chlorite, kaolinite, and minor amounts of calcite, siderite, anatase, rutile, and pyrite (Wilson, 2012). Total organic carbon contributes 1.23 percent by weight of the reference material (Wilston, 2012). Rhenium and Osmium concentrations range between 10.11-10.41 ppb and 93.3-100.5 ppt, with $^{187}Re/^{188}Os$ ratios and $^{187}Os/^{188}Os$ ratios ranging between 800.1-887.0 and 4.774-5.292.

7.3.2 Reagents

Chemical reagents used for extraction and oxidation includes ultrapure deionized (18.2 MΩ) Millipore water and trace metal grade 4 N CrO_3-H_2SO_4.

7.3.3 Temperature Extraction

A two-part sample digestion procedure was adopted. The initial digestion involved (1) approximately 200 mg of reference material SBC-1-0011, (2) an appropriate amount of ^{185}Re-^{190}Os spike, and (3) 8 mL of ultrapure deionized (18.2 MΩ) milli-pore H_2O. Non-oxidizing, milli-pore H_2O, media was added to a 15 mL Carius tube under cryogenic conditions, which was sealed via blowtorch and incubated at temperatures of 100°C, 150°C, 240°C, and 275°C in an oven for 72 hours. An additional leaching experiment was performed at room temperature (18.5°C) in a 22-mL glass vial using 8-mL of ultrapure deionized (18.2 MΩ) milli-pore H_2O for 72 hours. Following the first sample digestion/leaching phase, the leachate was transferred by filtration to a new 15-mL Carius tube under cryogenic conditions, which was immediately doped with 4-mL 4 N CrO_3-H_2SO_4 (oxidizing media). The sample Carius tube was sealed by blowtorch and digested in an oven at 240°C for 72 hours. Subsequent procedures followed the pre-described Re-Os methodology as outlined in section 4.1.3.

7.4 Results

Rhenium and osmium concentrations and isotopic ratios for reference material SBC-1-0011 under varying temperature regimes are reported in Table 8 (see appendix) and Figure 7.1. Overall, rhenium concentrations under all temperature regimes yielded lower concentrations than expected values derived from the traditional, CrO_3-H_2SO_4, digestion procedure. Re concentrations, however, did not correlate proportionally with temperature, as samples at a higher temperature regime of 275°C exhibited slightly lower concentrations than samples at a lower temperature regime of 240°C. The lowest Re concentrations (2.1 ppb) were leached at 18.5°C, whereas the highest Re concentrations (9.4 ppb) were leached at 240°C. In contrast, Os

concentrations were slightly higher than expected values at temperatures of 240°C and 275°C and lower at 150°C and room temperature (18.5°C). A 100°C temperature regime failed to yield measurable Os concentrations. However, it can be assumed that at 100°C Os was leached, since Os was leached at the lower temperature of 18.5°C. The failure to measure Os at 100°C, therefore, was likely an analytical error. At temperatures of 150°C, $^{187}Re/^{188}Os$ and $^{187}Os/^{188}Os$ ratios were 1.3 and 1.1 times higher than typical values, with temperatures of 240°C and 275°C yielding ratios that were ~ 60-70% of the expected values. At room temperature, the $^{187}Re/^{188}Os$ ratio was ~270% higher than expected values, while the $^{187}Os/^{188}Os$ ratio was only ~80% of the expected values.
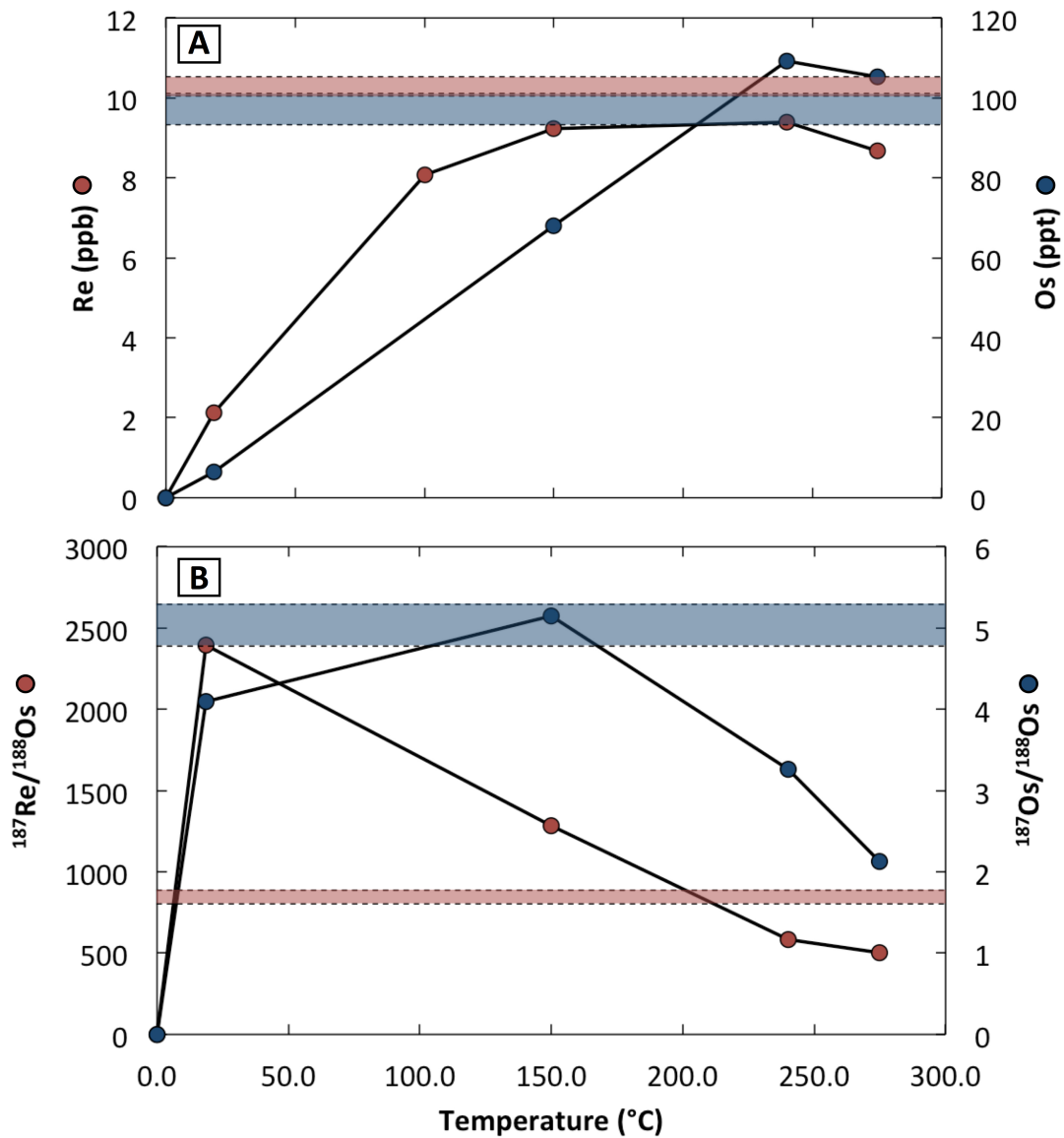
Figure 7.1 Extracted Re and Os concentrations (A) and isotopic ratios (B) using 8-mL deionized Millipore H_2O across a range of extraction temperatures. Red and blue shaded bars correspond to the expected range of Re and Os concentrations and isotopic ratios using conventional acid digestion procedures (4-mL 4 N H_2SO_4 and 4-mL 4 N CrO_3-H_2SO_4 T = 240°C for 72 hours).

7.5 Discussion

7.5.1 Re and Os Extraction Yields

The efficiency of subcritical water to extract Re from reference material SBC-1-001 is demonstrated by high extraction yields at low extraction temperatures (20% at 18.5°C, 80% at 100°C, 91% at 150°C). However, high extraction yields at low extraction temperatures did not translate to higher extraction yields at higher temperatures. For example, Re extraction yields did not scale beyond 150°C, but rather plateaued at 240°C and then slightly decreased to 85% at 275°C. In contrast, Os exhibited relatively low extraction yields at low extraction temperatures (7% at 18.5°C, 70% at 150°C) and high extraction yields (> 100%) at or beyond 240°C. Akinlua and Smith (2010) observed similar plateauing effects of redox sensitive trace elements Cr, Mn, Ni, Cd, and V at temperatures of 250°C and 300°C using conventional - High Pressure Liquid Chromatographic (HPLC) - subcritical water extraction techniques. Therefore, it can be assumed, by analogy, that Re and Os extraction yields will likely remain invariant up to extraction temperatures of 300°C.

Extracting Re and Os in variable, yet unequal, proportions from reference material SBC-1 over discrete experimental temperatures also induced $^{187}Re/^{188}Os$ isotope fractionation effects that were 2.8 (18.5°C), 1.5 (150°C), 0.7 (240°C), and 0.6 (275°C) times that of expected values derived from conventional acid digestion procedures (Figure 7.2). This trend suggests that at some temperature between 150°C and 240°C there exists an equilibrium state where Re and Os are partitioning from the solid (shale) to the liquid (water) phase at an equal rate to yield the expected $^{187}Re/^{188}Os$ value of SBC-1. By calculating the partition coefficient of Re/Os from the solid to liquid phase (see equation 7.1) at each of these discrete temperature intervals this theoretical temperature can be estimated from the slope of the relationship (Figure 7.3). The Kd(Re/Os) values of the aqueous phase at T <= 150°C are >1, which confirms previous observations that Re preferentially partitions from the solid to the liquid phase over Os, whereas at T >= 240°C the Kd(Re/Os)$_{aqueous}$ values are < 1, which confirms the inverse

observation. A Kd(Re/Os)$_{aqueous}$ value of 1 yields an equilibrium temperature of T = 217°C.

Similarly, a Kd(Re/Os)$_{aqueous}$ value of 1 yields an ^{187}Re/^{188}Os ratio of 855.63 (Figure 7.3) that falls

within the statistical limits of the expected ^{187}Re/^{188}Os value of SBC-1. This implies that an

extraction temperature of 217°C should theoretically yield an ^{187}Re/^{188}Os ratio equivalent to

the expected value of SBC-1. Presumably this also indicates that the ^{187}Os/^{188}Os ratio of the

solid phase would equilibrate with the liquid phase at this temperature.

Equation 7.1:
$$K_{D[Re/Os]} = \frac{[Re/Os]_{AQ}}{[Re/Os]_{ORS}}$$
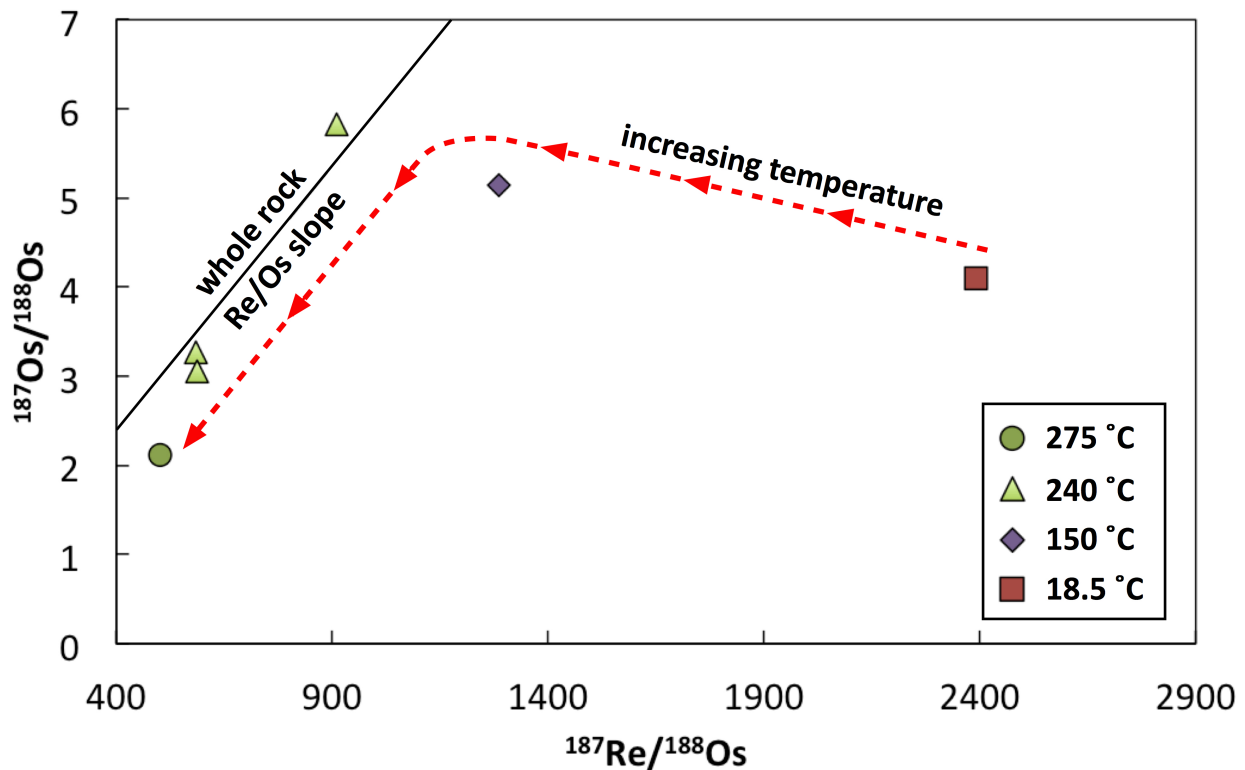
Figure 7.2 Plot illustrating various ^{187}Re/^{188}Os (X) and ^{187}Os/^{188}Os (Y) ratios at different extraction temperatures. Solid black line denotes ^{187}Re/^{188}Os and ^{187}Os/^{188}Os slope of conventionally whole rock extracted of SBC-1-0011. Dotted curved red line denotes direction of increasing temperature.
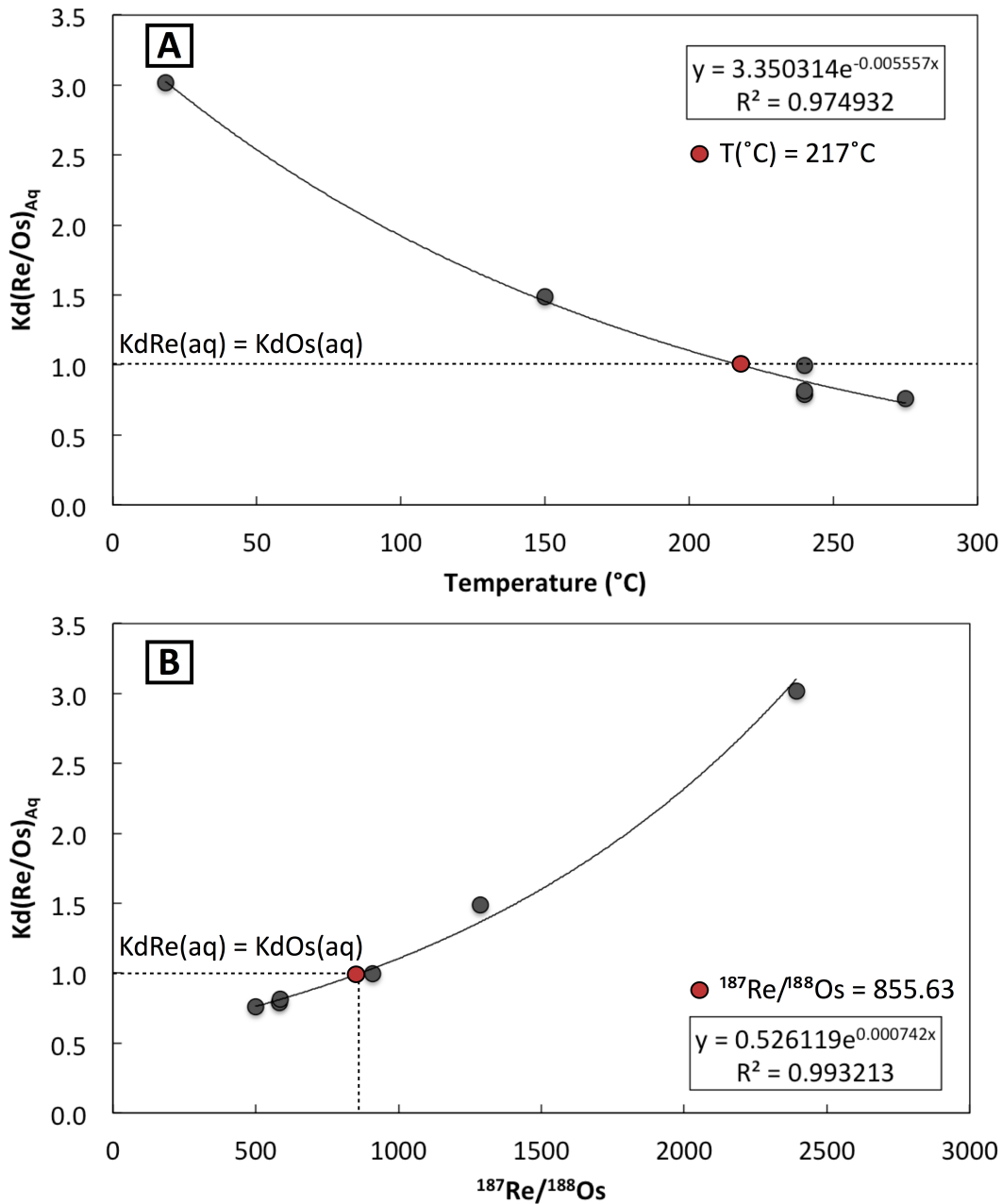
Figure 7. 3 Plots A and B denotes the relationship between the partition coefficients of Re/Os in the aqueous phase relative to temperature (A) and ^{187}Re/^{188}Os (B). Theoretical estimates here suggest that Re and Os partition from the solid to the liquid phase at equal rates (Kd(Re/Os) = 1) at a temperature of 217°C, which will yield a ^{187}Re/^{188}Os ratio of 855.63 that lies within uncertainty of ^{187}Re/^{188}Os ratio of SBC-1 derived from conventional digestion methods.

7.5.2 Controls of Re and Os Leaching

Two possible effects may be controlling the asymmetric leaching behaviour of Re and Os observed in SBC-1-0011. The first is Re and Os bonding affinity to organic matter, and the second is the effectiveness of cold and hot (subcritical) water to solvate Re and Os. The predominant organic matrix present in organic-rich sediment is kerogen, which hosts the largest fraction of Re and Os (>95%) in organic-rich sediment (Rooney et al., 2012). This insoluble, recalcitrant, organic material is, therefore, the most probable source of Re and Os present in SBC-1-0011. In isolating organic matter present in shales of the Exshaw Formation, Selby and Creaser (2003) found large amounts of Re present in the HF solutions after chemically isolating the OM. The excess Re present in the HF solution was attributed to the inadvertent leaching of Re from OM, which adversely altered the Re-Os isotopic systematics of the chemically isolated OM. Selby and Creaser (2003) followed this by testing whether Os was also removed from OM during the HF treatment phase and found that the ^{187}Os/^{188}Os isotopic composition of the solution was far too radiogenic to be attributed to the source OM, and was more likely derived from dissolution of silicate minerals. A replicate experiment, however, found that the ^{187}Os/^{188}Os isotopic composition of the second HF solution (3.06 ± 0.01) was comparable to the source OM (~ 2.97), suggesting that the HF solution had leached some Os from the OM. When compared by percentage leached, however, Re (~125%) far exceeded Os (2.9% to 8.8%). Wright (2015) observed similar Re/Os fractionations when isolating kerogen from samples of the Eagle Ford Formation by a Soxhlet extraction/HCl-HF technique. For example, ^{187}Re/^{188}Os ratio of kerogen extracts (1958 ± 121) were significantly less than the whole rock ^{187}Re/^{188}Os ratio (~2300-2800) (Wright, 2015), which was contrasted by the agreement, within uncertainty, of the ^{187}Os/^{188}Os ratios of kerogen extracts (4.85 +/- 0.46) and whole rock (~ 4.38-5.38) (Wright, 2015).

Although Selby and Creaser (2003) and Wright (2015) employed different analytical approaches to isolating OM they both managed to arrive at broadly similar results demonstrating Re preferential removal over Os from OM. These findings are also in agreement

with our experimental results employing cold/hot water as an extraction medium, which strongly suggests that the preferentially removal of Re over Os from OM manifests itself independently of the solvent used. These observations also support previous research detailing asymmetric Re and Os mobility during black shale weathering (Jaffe et al. 2000). This therefore leaves differences in bonding and/or residency internal to kerogen as the primary control over Re and Os leaching behaviour. For example, preferentially partitioning Re over Os at lower extraction temperatures may result from stronger organic chelating bonds between Os and kerogen (Rooney et al., 2012). Kerogen being a composite of biomacromolecules provides conceptual opportunity for Re and Os to be bound to different biomacromolecules, which perhaps have a propensity to interact differently with fluid mediums, oxidative or otherwise. Suppositions involving Re and Os bound to disparate biomacromolecules, while agree with our experimental data, remain speculative and require some form of combined XANES and micro-imaging analysis to characterize the precise location and valence states of Re and Os in ORS.

7.5.3 Implications for Post-depositional Re/Os Mobility

Removal of Re and Os by both cold and hot (subcritical) water from reference material SBC-1-0011 provides proxy evidence of how fluid, whether hydrothermal, groundwater, or surface runoff, in contact with ORS can disturb the isotope systematics of the Re-Os system. Kendall et al. (2009) and Yang et al. (2009) provided geological accounts of how post-depositional hydrothermal fluids adversely affected the Re-Os systematics of ORS via either introduction of allochthonous-sourced Re and Os and/or mobilization of autochthonous-sourced Re and Os, which largely parallels our experimental findings. In the case of Kendall et al. (2009), Re-Os isochron regression analysis of the Wollogorang Formation yielded a highly imprecise Re-Os age that was 200 Ma younger than previous U-Pb shrimp zircon estimates. Analysis of the sub-millimeter dolomite veinlets revealed enrichments of ^{187}Re/^{188}Os (~8.5%) and ^{187}Os/^{188}Os (~2.8%) relative to adjacent shale material that reaffirmed disturbance of Re-Os systematics implicating post-depositional hydrothermal fluids as the cause of the scatter in the

isochron (Kendall et al., 2009). These observed ^{187}Re/^{188}Os enrichments of dolomite veinlets are comparable to the observed ^{187}Re/^{188}Os enrichments of the leachate from SBC-1 at high extraction temperatures. Yang et al. (2009) found similar evidence of post-depositional disturbance in drill core samples from Joy Lake carbonaceous slates. Comparison of Re-Os isochrons DH 26503 and DH 26505 revealed statistical Re-Os age agreement, but disagreement in the initial ^{187}Os/^{188}Os ratios of the regression. Rather than removal of Re/Os from Joy Lake carbonaceous slates, Yang et al. (2009) reasoned that hydrothermal fluids infused with anomalous quantities of radiogenic Re leached from proximal tuffaceous beds was introduced into sample set DH 26505. The slight introduction of radiogenic Re into DH 26505 had the effect of tilting the slope of the isochron such that the Os$_I$ was offset from a chondritic value to a negative value whilst maintaining Re-Os age coherency with sample set DH 26503.

Extraction of Re and Os from ORS at room temperature (18.5°C) - in the absence of an external heat source - also parallels Re and Os mobility observed in the exogenic environment, such as during black shale weathering. For example, Jaffe et al. (2002) reported removal of Re (~99%) and Os (~39%) from weathered black shales alongside decreases in black shale C$_{org}$ content. The proximity of the weathering horizon to the surface combined with the loss of Re and Os restricted to the top 4 m of the weathering profile suggested that surficial runoff charged with dissolved O$_2$ oxidized reduced OM by percolating top down through the black shale weathering horizon, which in turn liberated liable OM-bound Re and Os. Provided that low extraction temperatures (18.5C) removed only a modest amount of Re (10%) an Os (10%) over a 72-hour period, it is conceivable that extending the exposure time of SBC-1 to water will increase the faction of Re and Os removed. Similarly, modest increases in extraction temperatures (i.e. 10°C) simulating warm temperate climatic conditions will likely improve Re and Os extraction yields. However, whether these experimental modifications will yield comparable results to those observed in the exogenic environment remains challenging to establish, since Jaffe et al. (2002) reported Re and Os removal in the present, and not absent, of organic matter oxidation. Based off observations of post-extracted shale power aliquots of SBC-1, it remains unclear whether Re and Os were leached from reduced-OM or liberated via OM-oxidation. However, organic matter oxidation has been observed in black shales of the

Ravnefjeld Formation in East Greenland that appeared macroscopically pristine (Georgiev et al., 2012). Analysis of the Re and Os isotopes has revealed disturbance of the Re-Os systematics relative to samples taken from drill core (Georgiev et al. 2012). Georgiev et al. (2012) propose a coupled Rock-Eval and S analysis to constrain organic matter oxidation in pristine looking shales where disturbance of Re-Os systematics is suspect. Therefore, based on this evidence alone oxidation of organic matter likely occurred to some extent in SBC-1. This combined with the fact that (1) the deionized Millipore water used during the extraction experiment was not purged of dissolved O_2 and (2) atmosphere was trapped in the extraction vessel increases the overall likelihood that organic matter oxidation played some role in removal of Re and Os from SBC-1. Irrespective of the extraction mechanisms, the experiment results reported here provide direct experimental evidence of the overall sensitivity of Re-Os systematics to fluid as first observed in geological settings.

7.6 Conclusion

Cold and hot (subcritical) water effectively removed Re and Os from shale powders of USGS reference material SBC-1 under a range of extraction temperatures (18.5°C – 275°C) over a 72-hour period. Rhenium and Osmium yields differed at low extraction temperatures, which suggests that Re and Os may occupy different sites of residency within the source organic matter of ORS. In addition, the removal of both Re and Os by cold and (hot) water provides experimental evidence of the overall sensitivity of Re-Os systematics to fluids, which has implications for how Re-Os systematics can be disturbed in near surface weathering environments and low temperature environments.

8 | Kerogen Carbon Isotopes of the Lower Jurassic Fernie Formation

8.1 Introduction

High molecular weight hydrocarbons comprise, by weight, >90% of the total organic content found in immature organic-rich sedimentary rocks (Durand, 1980). The remaining <10% is comprised of, non-polar, low molecular weight hydrocarbons (Philp, 2014). The former fraction, collectively defined as kerogen, is a composite of microbially and thermally degraded insoluble organic macromolecules biosynthesized from precursor microorganisms and plants, which depending on source input can be of terrestrial or marine origin (Philp, 2014). The carbon isotopic composition of kerogen, therefore, varies in response to both the source and fractional components (algal vs. plant) of the organic material (Whiticar, 1996). For example, terrestrial bound algae of lacustrine environments are isotopically lighter (-25 to -40 permil) than their marine counterparts (-15 to -30 permil) (Chikaraishi, 2014). These C isotopic signatures are reflected in algae dominated - Type I/II – kerogens (- 20 to -37 ‰), whereas high plant dominated - Type III - kerogens tend to be isotopically heavy (~ -26 to – 28.5 ‰) (Whiticar, 1996).

The relationship between organic-rich sedimentary rocks and Re and Os enrichment has be known since the early developments of ORS Re-Os geochronometer (Ravizza and Turekian, 1989). Selby and Creaser (2003), for example, conducted the first experimental work isolating organic matter present in ORS for their Re and Os content. Their findings established an explicit correlation between Re and Os present in organic matter and Re and Os present in whole rock (Selby and Creaser, 2003). This study set the ground work for future studies by demonstrating that organic matter is the primary source of Re and Os in ORS. Subsequent investigations of Re and Os residency in soluble (oil and asphaltenes) and insoluble (kerogen and bitumen) organic matter fractions, however, have revealed Re and Os to be predominantly concentrated in

kerogen (Re = ~ 1184 ppb, Os ~4710 ppt), followed by bitumen (Re = ~ 91 ppb, Os = ~ 129 ppt), and then oil and asphaltenes (Re = ~ 91 ppb, Os = 192 ppt) (Wright, 2015). These findings are in strong agreement with hydrous pyrolysis experiments by Rooney et al. (2012) that showed minimal Re and Os fractionation in the source rock following oil generation. For example, the Re and Os concentrations of non-pyrolysed extracted rock (insoluble organic matter + inorganic minerals) was near equivalent to that of pyrolysed extracted rock independent of pyrolysis temperature (250°C to 350°C over a 72 hour period). The retention of Re and Os in kerogen following oil generation implies that Re and Os must be tightly bound to the kerogen in order for the Re-Os ORS chronometer to remain robust in overmature shales (Rooney et al., 2012).

Even though the general source of Re and Os in organic-rich sediment has been identified, the relationship between Re and Os and the C isotopic composition of kerogen remains to be explored. Here we aim to bridge this knowledge gap by exploring the relationship between the C isotopic composition of kerogen in the Gordondale and Poker Chip Members in relation to Re and Os concentrations and isotopic ratios. In addition, we explore the claim as to whether the Gordondale Member is in fact the preeminent source rock for the WCOS.

8.2 Geological background

The reader is referred to chapter 3 for a detailed summary of the geology of the Gordondale Member and overlying Poker Chip Member.

8.2.1 Organic Geochemistry

Gordondale Member

TOC, with respect to each stratigraphic unit in the Gordondale Member, is unevenly distributed (Figure 8.1) with the highest weight percentage found in the Lower Radioactive Unit (TOC up to 28 wt.% TOC), followed by the Upper Radioactive Unit (TOC up to 18.5 wt.% TOC), and the Middle Silty Unit (TOC up to 5 wt.%). Irrespective of mass distribution, organic matter, in the form of bitumen, presents itself as a pervasive porosity filled-matrix visible in all Gordondale stratigraphic units (Riediger, 1993). Rock-Eval analysis characterized the residual

(kerogen) component as predominately Type I/II (algal-sourced) sulphur-rich (Riediger, 1990). Riediger (1993) reports sulphur content as high as 7 wt.%, which presumably changed the cracking kinetics and expanded the oil window (see Figure 3.1). Key kerogen components identified through organic petrography include abundant liptinite macerals – alginate, sporinite (rare), liptodetrinite, and bituminite -, and lesser amounts of inertinite and exsudatinite (Riediger, 1993). N-alkane, primarily C_{14}-C_{17} compounds, further support algae and/or bacteria as the dominant source of organic matter (Riediger, 1993). Vitrinite and long-gain N-alkanes of the high land plant derivative have been identified, although only in minor amounts (Riediger et al., 1990).
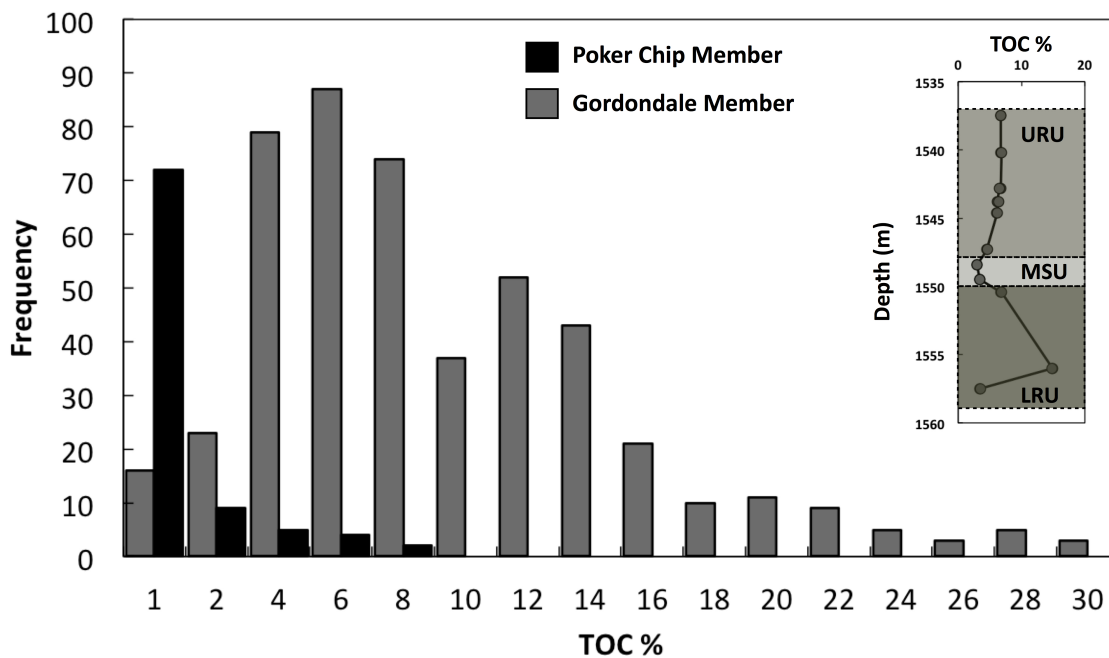
Figure 8.1 Total organic carbon (TOC) distribution of the Gordondale (grey) and Poker Chip (black) Member. The average TOC concentration of the Gordondale and Poker Chip Member is 8.36 weight percent and 0.80 weight percent. The insert depicts the TOC distribution in the Gordondale with respect to depth (UWI = 7-31-79-10W6). On average, the Lower Radioactive Unit (LRU) (shown in dark brown) has the highest TOC, followed by the Upper Radioactive Unit (URU) (shown in medium brown), and then the Middle Silty Unit (MSU) (shown in light brown). TOC data was retrieved from Riediger (1990, 2002).

Poker Chip Member

Riediger (2002) stratigraphically divided the Poker Chip Member into a lower, organic-rich, Early to Late Toarcian unit and an upper, organic-poor, Toarcian to Aalenian age unit. The Lower (A) unit has a mean TOC wt.% of 3.83, whereas the upper (B) unit has a mean TOC wt.% of 0.38. The full TOC distribution for the Poker Chip Member, however, is shown in Figure 8.1 above. The kerogen composition is identified as marine algal, Type II, kerogen (Riediger, 2002).

8.3 Methods

The methods used to isolate and analysis the C isotopic composition and content of kerogen from a select set of ORS from the Poker Chip and Gordondale Member are described in section 4.3.1.

8.4 Results

Organic carbon kerogen weight percent and isotopic data and frequency distribution plots for the Gordondale and Poker Chip Member are presented in Table 9 (see appendix) and Figure 8.2. Organic carbon kerogen weight percent values ($C_{kerogen}$ wt.%) in the Gordondale Member range from 6.88 to 10.85 wt.% in the Upper Radioactive Unit and 7.23 to 39.26 wt.% in the Lower Radioactive Unit. In comparison, $C_{kerogen}$ wt.% in the Poker Chip Member are constrained to a much narrower range of 3.11 to 5.26 wt.%, which amounts to a mere 13-45% of the $C_{kerogen}$ wt.% present in Gordondale Member samples. Although there is a clear asymmetry in the amount of carbon in the form of kerogen present in Gordondale and Poker Chip Member samples, the C isotopic composition (δ^{13}C) of the kerogen from each stratigraphic member broadly overlap, with the Gordondale Member having slightly higher and lower $\delta^{13}C_{kerogen}$ values than Poker Chip samples. For example, $\delta^{13}C_{kerogen}$ values of Gordondale Member samples range from -28.71 ‰ to -31.2 ‰, whereas Poker Chip samples range from -30.00 ‰ to -30.27 ‰.
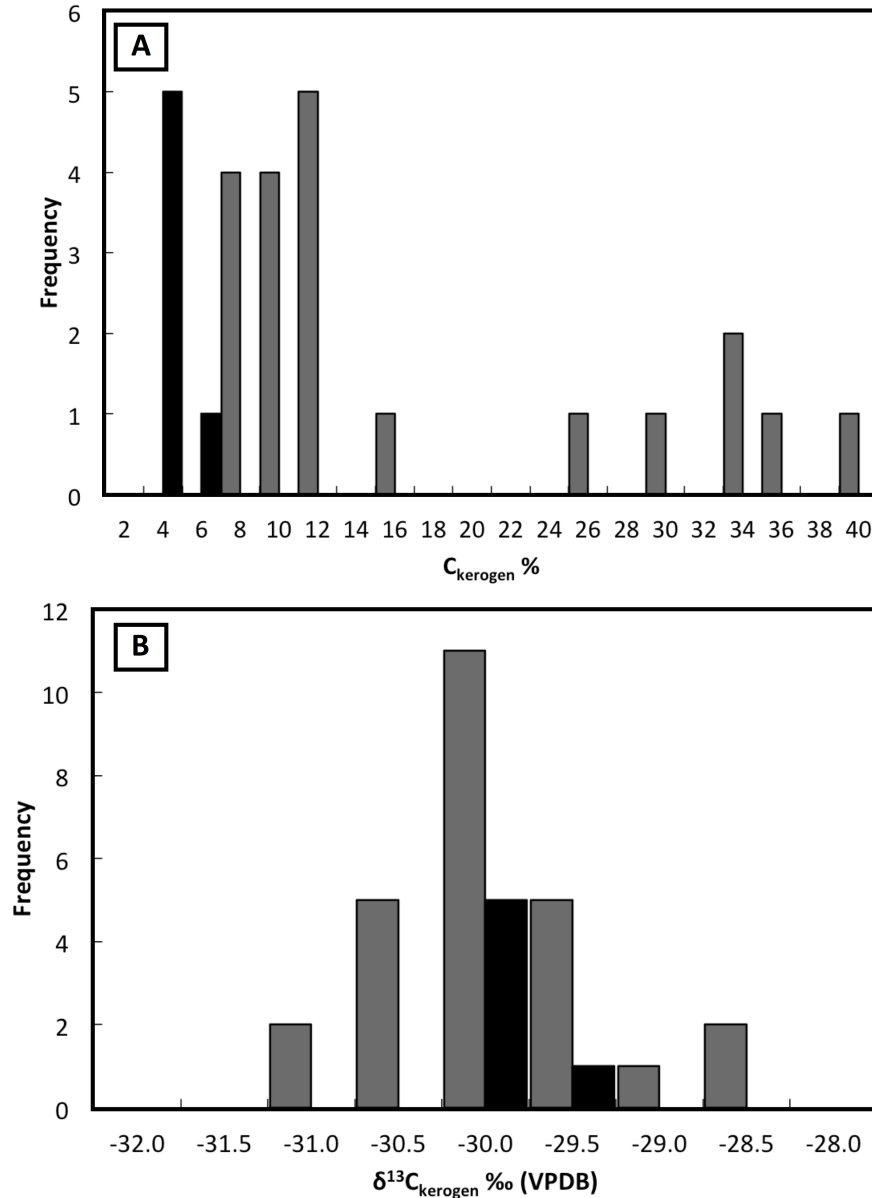
Figure 8.2 Organic carbon weight percent kerogen ($C_{kerogen}$ wt.%) distribution plot (A) of Gordondale (grey) and Poker Chip (black) samples. $\delta^{13}C_{kerogen}$ distribution plot (B) of Gordondale (grey) and Poker Chip (black) samples.

8.4.2 Kerogen, δ^{13}C, and Re-Os

Rhenium, ^{192}Os, and ^{187}Re/^{188}Os plots normalized to C$_{kerogen}$ % and δ^{13}C$_{kerogen}$ fractionation are presented in Figure 8.3. Rhenium normalized to C$_{kerogen}$ formed three distinct populations that are well correlated (R^2$_{population1}$ = 0.7, R^2$_{population2}$ = 0.9, and R^2$_{population3}$ = 0.7). Population 1, which - with the exception of two samples (basal Gordondale: JT17-19202A and JT1-19202F) - is a composite of upper Gordondale (JT17-19204) and basal Poker Chip (JT17-19203) samples, has the steepest slope (m$_1$ = 40), whereas basal Gordondale samples form two distinct populations (population 2 = JT1719201/2/TS0027-31; population 3 = JT1719205) that have shallower slopes (m$_2$ = 11 and m$_3$ =-2). These populations have been propagated throughout the remaining plots (i.e. ^{192}Os/C$_{kerogen}$ %) to see if similar correlations persist. Although populations (1,2,3) for ^{192}Os and ^{187}Re/^{188}Os are poorly correlated with respect to kerogen content (R^2 < 0.5), the slopes (with the exception of population 1 in plot C) follow similar trends in orientation to Re. Correlations of Re and Os and δ^{13}C$_{kerogen}$ fractionation, however, reveals contrasting slope orientations (negative) relative to kerogen content, suggesting that light isotopic enrichment corresponds to increased Re and Os concentrations. However, correlation coefficients are fairly weak with respect to Re (R^2 < 0.3), but strong with populations 2 and 3 for Os (R^2$_{population2}$ = 0.8, R^2$_{population3}$ = 0.9). In contrast, ^{187}Re/^{188}Os ratios are positively oriented, but exhibit weak correlations in population 1 (R^2 = 0.0) and 2 (R^2 = 0.2) and strong correlations in population 3 (R^2 = 0.8).

Although some correlations are observed between sample populations, there are also some inherent ambiguities between sample populations for Re, Os and ^{187}Re/^{188}Os. For example, ^{192}Os/δ^{13}C$_{kerogen}$ populations have more robust correlation coefficients than Re/δ^{13}C$_{kerogen}$, and it remains unclear as to whether the scaling of Re and ^{192}Os is related to a proportional increase in the percent C$_{kerogen}$ in each sample population. To compensate for this effect, ^{192}Os and ^{187}Re/^{188}Os ratios are normalized to C$_{kerogen}$ % (y-axis) and plotted against δ^{13}C$_{kerogen}$ (x-axis) on the same graph (Figure 8.4). From this approach two important relationships become explicit: (1) ^{187}Re/^{188}Os/C$_{kerogen}$% of basal Poker Chip (Fig. 8.4a) and Upper

Gordondale Samples (Figure 8.4b) are negatively correlated with respect to $\delta^{13}C_{kerogen}$, whereas basal Gordondale samples are positively correlated (Figure 8.4c/d), and (2) $^{192}Os/C_{kerogen}$% for all samples are negatively correlated with respect to $\delta^{13}C_{kerogen}$. Although this implies a general trend of ^{192}Os concentration increasing with light isotope enrichment, some samples are better correlated than others. For example, samples in Plot C (R^2 =0.96) and D (R^2 = 0.70) are well correlated with respect to light isotope enrichment, whereas samples in Plot A (R^2 = 0.12) and B (R^2 = 0.05) are not. Interestingly, $^{187}Re/^{188}Os$ is well correlated with respect to $\delta^{13}C_{kerogen}$ in all samples. For example, all samples have a correlation coefficient > 0.6 with on sample set (JT17-19203) exhibiting a correlation coefficient of 0.99. These observations tentatively suggest that $^{187}Re/^{188}Os$ and $\delta^{13}C_{kerogen}$ in ORS are related.
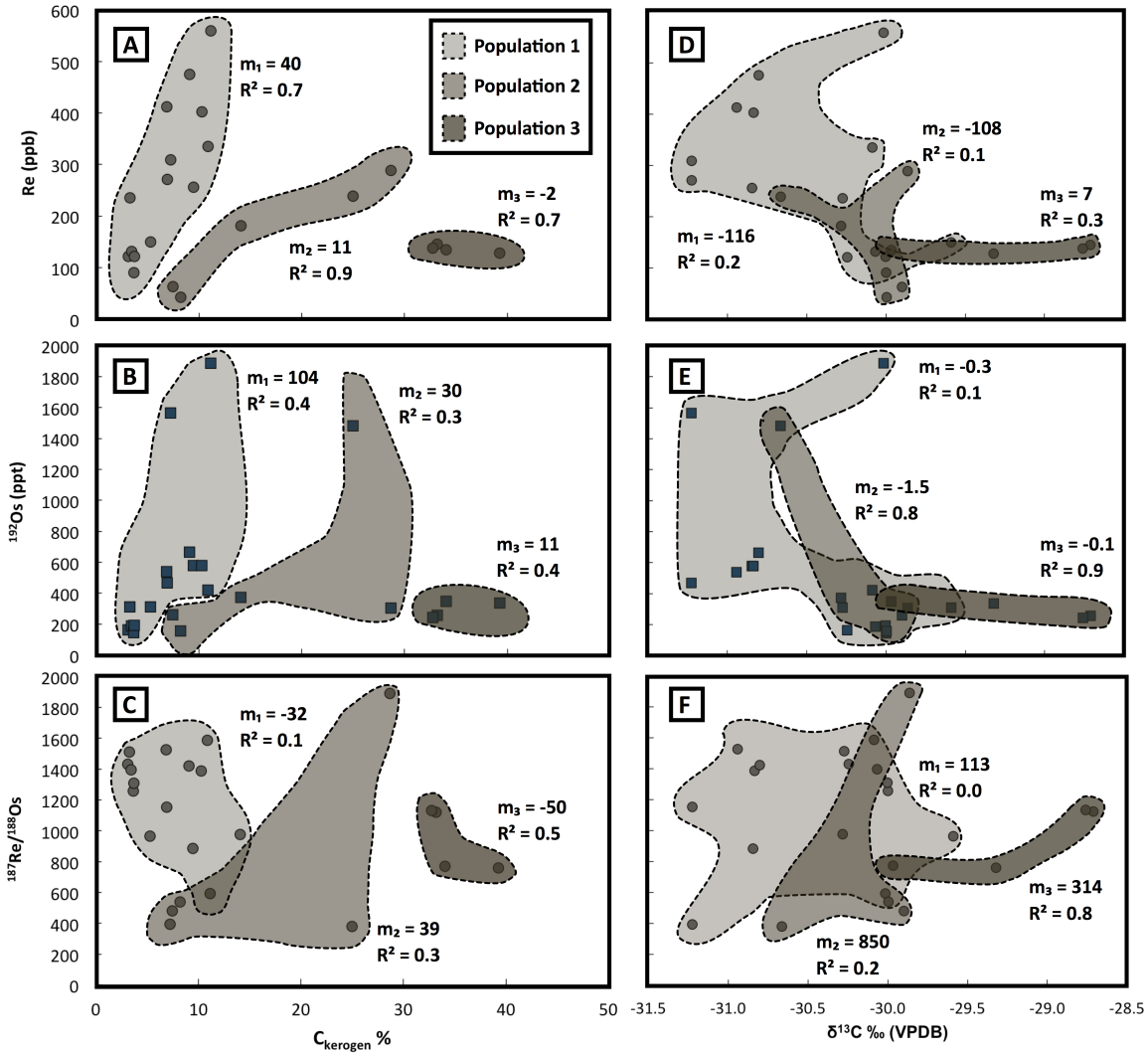
Figure 8.3 Plot A-F illustrates the relationship between Re, ^{192}Os, and ^{187}Re/^{188}Os and $C_{kerogen}$ and δ^{13}C in both basal Poker Chip and Gordondale Member sample sets. Three main populations (population 1 = light brown, population 2, = medium brown, population 3 = dark brown) have been identified with respect to how Re, Os, and ^{187}Re/^{188}Os are distributed in kerogen, which have been propagated through to δ^{13}C. Each population has a corresponding slope (population 1 = m_1, population 2 = m_2, population 3 = m_3) and R^2 value associated with it.
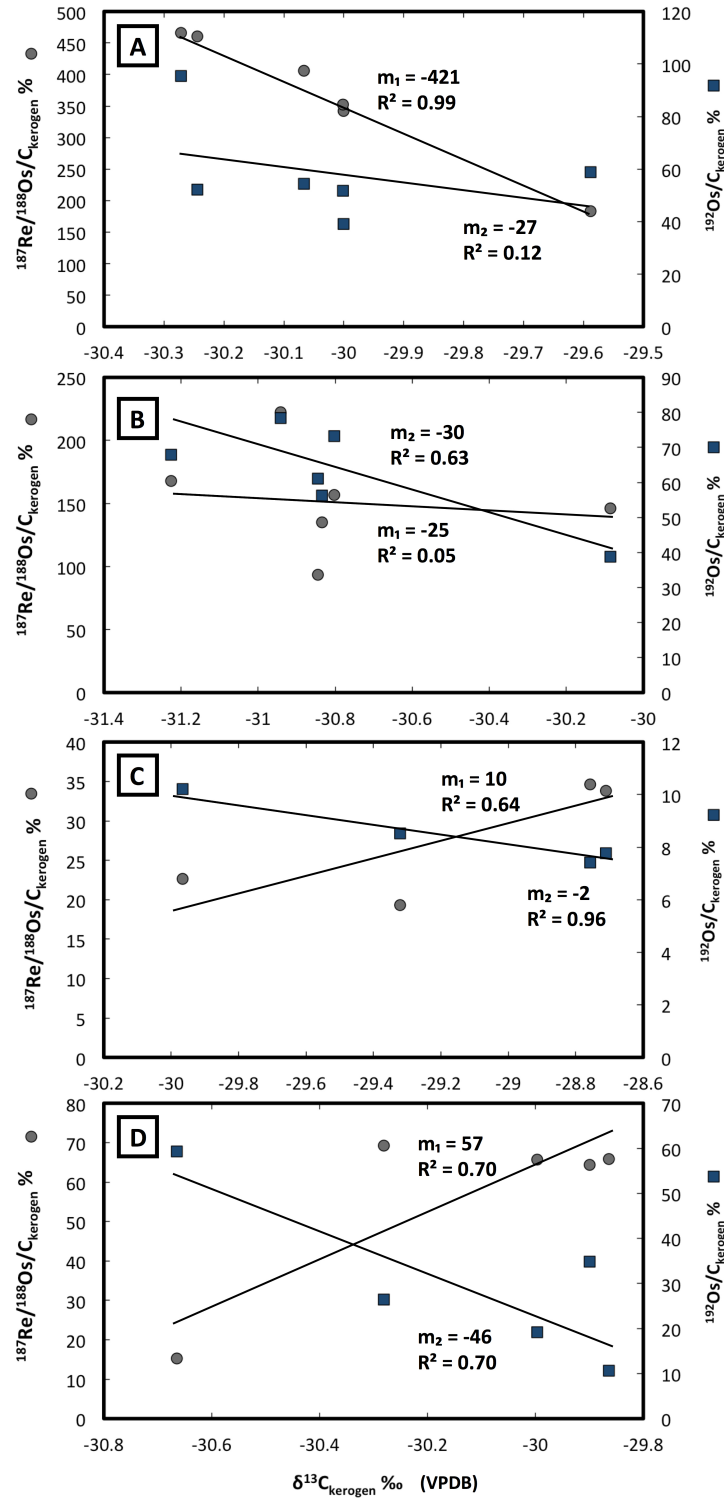
Figure 8.4 $^{192}Os/C_{kerogen}\%$ and $^{187}Re/^{188}Os/C_{kerogen}\%$ vs. delta$^{13}C_{kerogen}$ plots. Plot A, B, C, and D correspond to basal Poker Chip (A = JT17-19203), Upper Gordondale (B = JT17-19204), and Lower Gordondale (C = 19205, D = JT19201, 2, TS0028-31) samples. $M_1 = {}^{187}Re/^{188}Os/C_{kerogen}$ slope, $M_2 = {}^{192}Os/C_{kerogen}$ slope.

8.5 Discussion

8.5.1 $\delta^{13}C_{kerogen}$ Composition

The carbon isotopic composition of kerogen is linked to the organic macerals that comprise the constituent kerogen (Whiticar, 1996). For kerogens dominated by vitrinite/inertinite macerals the $\delta^{13}C$ value is reminiscent of the precursor terrestrial high land plant material from which they are derived, whereas in those dominated by alginite macerals the $\delta^{13}C$ value is derivative of the precursor marine planktonic and bacterial microfauna (Whiticar, 1996). This is in part related to the selective preservation of certain recalcitrant biomacromolecules of the source organics during kerogen formation (Tegelaar et al., 1989). This source-typing feature of kerogen provided by organic C isotopes remains in effect even for rocks subjected, as is the case for the Gordondale and Poker Chip Member samples, to the effects of early diagenesis and thermal maturation (Gearing et al., 1984; Lewan, 1983). During high-grade metamorphism, the C isotopic composition of the kerogen exhibit large per mil isotopic shifts, and breaks down as an isotopic tracer (Baker and Claypool, 1970). This, therefore, uniquely allows for both source-typing the kerogen and oil-to-source rock correlations.

The kerogen composition of the Gordondale Member has been explored extensively, through both the use of organic petrography, Rock-Eval analysis, and GS-MS (Kondla et al., 2017; Riediger et al., 1990, Riediger, 1993). The results of such investigations, which include microscopically identified macerals of liptinite and inertinite, H-rich organic matter, and N-alkanes C_{14}-C_{17} biomarkers, concluded a dominantly Type I/II S-rich kerogen (Riediger et al., 1990). Similarly, Rock-Eval analysis of the Poker Chip Member revealed a predominantly Type I/II kerogen source (Riediger, 2002). A predominantly marine algal biomass is fitting with the basinal depositional model interpretation of the Gordondale and Poker Chip Member proposed by Poulton et al. (1994).

The $\delta^{13}C_{kerogen}$ values of the Gordondale and Poker Chip members fall within a tight range of -28 to -31 ‰ that overlap within isotopic range of other Type I and II kerogens (Whiticar, 1996). Known $\delta^{13}C_{kerogen}$ values range from -32 ‰ to -16 ‰, and overlap with a wide array of marine and terrestrial organic carbon isotopic sources. In the terrestrial domain, these include bulk plants (-36 ‰ to -22 ‰), cellulose (-27 ‰ to -24), marsh plants (-17 ‰ to -8 ‰), freshwater plankton (-33 ‰ to -24 ‰), and in the marine domain these include marine higher plants (-17 ‰ to -10 ‰), marine organisms (-20 ‰ to -10 ‰), and marine plankton (-30 ‰ to – 10 ‰). However, terrestrial and marine $\delta^{13}C$ values that overlap with the $\delta^{13}C_{kerogen}$ values of the Gordondale and Poker Chip Member are consistent with bulk plants and freshwater/marine planktonic sources. Previous kerogen typing by Riediger (1991, 1994, 2002) provides a means of eliminating bulk plant and freshwater planktonic sources as major contributors to the $\delta^{13}C$ signal of the kerogen present in the Gordondale and Poker Chip Member, and thereby helps to reaffirm a predominantly marine planktonic source.

8.5.2 Correlation of $C_{kerogen}$ and Re and Os

The kerogen component of ORS is established as the primary site of residency of Re and Os regardless of thermal maturation (Rooney et al., 2012; Wright, 2015). The correlation between Re and $C_{kerogen}$ observed in Early Jurassic shales of the Gordondale and Poker Chip is similar to other Phanerozoic ORS, such as the Permian Phosphoria Formation or the Cenomanian-Turonian Eagleford Formation (Rooney et al., 2012; Wright, 2015). Analogous correlations, however, are not observed in $^{192}Os/C_{kerogen}$ of the Gordondale and Poker Chip Member (0.3 to .0.4), which remains evident even when accounting for the radiogenic in-growth of ^{187}Os (0.3 to 0.5). With that said, the correlation coefficients of Re/$C_{kerogen}$ and $^{192}Os/C_{kerogen}$ of the Gordondale and Poker Chip member are comparatively low relative to Rooney et al. (2012) observed correlation between Re and Os and kerogen. This apparent discordance between Rooney et al. (2012) estimate and Gordondale/Poker Chip member samples could be an analytical artifact consequenced from (1) non-quantitative kerogen extraction and/or (2) Re and Os fractionation during kerogen extraction. Quantitative extraction

of kerogen is a persistent problem when isolating disparate organic phases using chemical extraction procedures, which depending on the chemical extraction medium used can result in varying extraction yields (Vandenbroucke and Largeau, 2007). Potential loss of kerogen during the extraction procedure, for example, could occur as kerogen particles suspended in the supernatant are decanted to waste. Furthermore, Re and Os isotopic fractionation was observed experimentally when isolating kerogen from whole rock samples (Wright, 2015). However, since our Re and Os data set is derived from conventional, extracted rock, procedures, then Re and Os isotopic fractionation can be disregarded as a viable hypothesis. Alternatively, the discordance may result from residual Re and Os hosted in soluble organic phases or sedimentary sulphide phases, such as pyrite. This latter hypothesis seems improbable knowing that the majority of Re and Os concentrated in ORS is in the form of kerogen, which constitutes > 90% of the organic matter in ORS. This, therefore, leaves non-quantitative kerogen extraction as the most probable source for the discrepancy in the Re and Os kerogen correlation. However, a non-quantitative kerogen extraction hypothesis does not explain why Re is better correlated with kerogen than Os.

8.5.3 Role of sulfurized-OM on ^{187}Re/^{188}Os fractionation

Organic matter (OM) is ubiquitously known as a major host of Re and Os in ORS (Selby and Creaser, 2003; Wright, 2015). Despite this fact, OM was originally assumed to play a passive and negligible role in ^{187}Re/^{188}Os fractionation of ORS. Instead, the water column/sediment redox conditions were favored for exerting the greatest control over ^{187}Re/^{188}Os fractionation in ORS (Yamashita et al., 2007). This picture has become somewhat more nuanced over the years, with some researchers speculating that OM-type may play a part in Re/Os fractionation (Cumming et al., 2014; Harris et al., 2013; Rooney et al., 2011). However, no direct evidence has been reported until now that causally connects Re/Os fractionation to OM-type in ORS. The observed relationship between carbon isotope fractionation of kerogen and ^{187}Re/^{188}Os fractionation (Figure 8.4) reported here, however, directly implies that OM exerts at least partial, and perhaps secondary-order, control over Re/Os fractionation in ORS. This relationship

may derive from Re and Os having specific affinities for isotopically distinct biomacromolecules that collectively comprise kerogen and that ^{187}Re/^{188}Os ratios change in response to which biomacromolecules dominate.

Numerous micro-imaging (TEM) and chemical analysis (^{13}C NMR) studies have identified a range of isotopically distinct aliphatic biopolymers that make up 10-30% of extant marine and terrestrial biomass, which remain preserved during diagenesis and contribute to the bulk kerogen content (Biller et al., 2015; Goth et al., 1988; Hatcher et al., 1984; Tegelaar et al. 1989; Vandenbroucke and Largeau, 2007; Whiticar, 1996). Pyrolysis studies have revealed that fossilized micro-algae are dominated by algaenan biomacromolecules that yield n-alkenes/n-alkane pyrolysates (Glen et al., 1996). In contrast, terrestrial (vascular) material composed, in part, by lignin biomacromolecules yield condensed aromatic pyrolysates (Gelin et al., 1996; Tegelaar et al., 1989). Eglinton (1994) and others analyzed the carbon isotopic compositions of algaenan pyrolysis products of Type I and II kerogens, and found that n-alkenes/n-alkanes are generally isotopically lighter than the average source kerogen, while isoprenoid-alkanes/alkenes are isotopically heavier (Burwood et al., 1988; Eglinton, 1994; Hold et al., 1998). These findings provide evidentiary support that algal-dominated kerogens (Type I), such as those identified in the Gordondale Member, are likely to be composed of numerous algaenan biomacromolecules with distinct carbon isotopic compositions related to different algal sources (Eglinton, 1994; Hold et al., 1998; Riediger, 1990, 2002; Riediger et al. 1993). However, attributing Re/Os fractionation exclusively to different algaenan biomacromolecular species remains challenging since Re and Os isotopic ratios would fractionate in response to kerogen cracking during catagenesis, which is not supported either experimentally, as in Re and Os pyrolysis experiments, or geologically, such as in overmature shales (Rooney et al., 2012; Creaser et al., 2001). Besides algaenans, bulk kerogens are also composed of ^{13}C enriched hydrocarbon that yield short carbon chain pyrolysis products (Hold et al., 1998). These ^{13}C enriched post-pyrolysis kerogen residues may, therefore, form major hosts of Re and Os.

Van Kaam-Peters et al. (1998) surmised that sulfurization of organic matter results in the preservation of carbohydrates, an otherwise less resistant, but ^{13}C enriched carbon molecule

prone to microbial degradation (Hatcher et al., 1984). Sulfurized carbohydrates, which derive their sulfur from sulfur reducing bacteria (SRB), form carbon chains of isotopically heavy C_1-C_3 alkylated thiophenes that act as opposite isotopic end-members to algaenan (lipid-like) biomacromolecules that collectively comprise marine kerogens (Sinninghe Damsté et al., 1998; Van Kaam-Peters et al., 1998). Van Kaam-Peters et al. (1998), employing a two end-member mixing model, found a clear correlation between heavy isotope enrichment and carbohydrate carbon content and light isotope enrichment and algaenan content. Organic matter present in the Gordondale Member is dominated by S-rich (1-7 wt.%) kerogen, which by inference, implies that sulfurized carbohydrates exist to some degree alongside algaenan material in the kerogen (Riediger, 1990, 1993; Riediger and Block, 1995; Ross and Bustin, 2006). Organic matter of the Poker Chip Member, however, is less well studied petrographically speaking, and therefore the extent of sulfurization remains largely unknown (Riediger, 2002). Ross and Bustin (2006), however, provided geochemical evidence that subsurface basal Poker Chip strata of NE British Columbia was absent of sulfurized-OM. Irrespective of this, Gordondale Member sample plots of $C_{kerogen}$ content vs. $\delta^{13}C_{kerogen}$ fractionation (Figure 8.5 B, D) confirm a relationship between $C_{kerogen}$ content and heavy isotopic enrichment that may be explained as a relative increase in a ^{13}C enriched sulfurized-OM biomass component that would have otherwise biodegraded in non-S-rich kerogens.
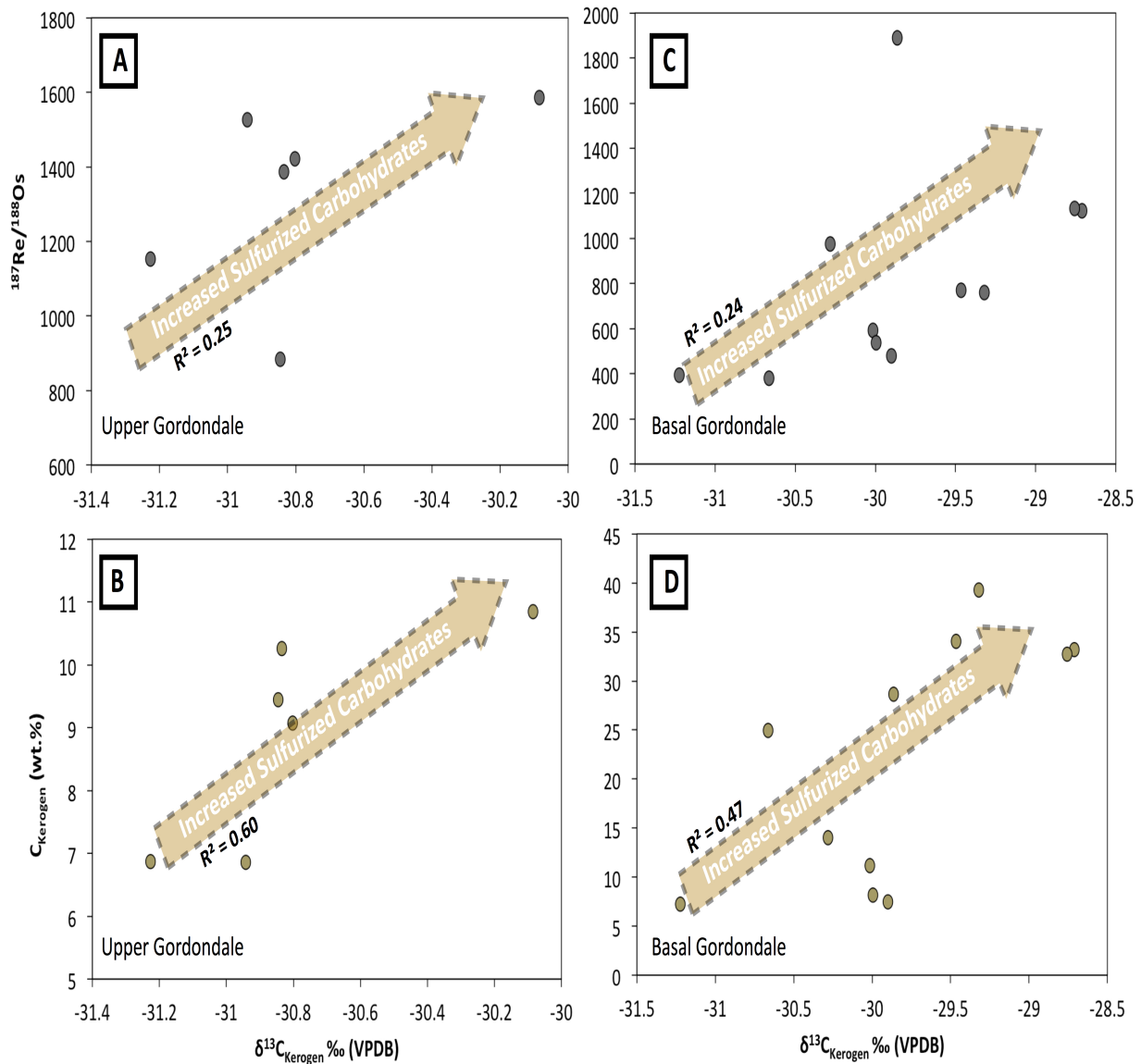
Figure 8. 5 Relationship between Re/Os fractionation, $C_{kerogen}$ concentration (wt.%), and $\delta^{13}C_{kerogen}$ for Upper Gordondale and Basal Gordondale samples. The orange arrow points in direction of increased sulfurized-OM content.

Sulfurization of organic matter is strongly linked to ocean euxinia or euxinic sediment porewaters and likely contributed to redox trace element enrichment in the Gordondale Member (Ross and Bustin, 2006). This is particularly true of Molybdenum (Mo), which is a geochemical analogue of Re, and becomes preferentially enriched in sediment deposited in

sulfidic waters (Helz et al., 1996; Morford et al., 2007). Enrichment of Mo in euxinic sediment occurs via HS^- pathway that transforms inert molybdenate into a reactive thiomolybdate species that is sequestered by S-rich organic matter (Tribovillard et al., 2004). For example, Tribovillard et al. (2004) examined Mo enrichment in sulfurized (orange) amorphous organic matter (AOM) and non-sulfurized (brown) AOM of Orbagnoux, Kimmeridge Clay, and Kashpir oil shales, and found in all cases that Mo was positively correlated with sulfurized AOM. In contrast, Mo shared no relation to non-sulfurized AOM or sulfur-derived pyrite (Tribovillard et al., 2004). Chappaz et al. (2014) reported similar findings of Mo primarily being bound to non-pyrite matrix of euxinic muds and shales. Studies detailing Re uptake mechanisms into euxinic basins have similarly found that HS- plays an important role in its sequestration into ORS, which implicates sulfurized organic matter, and in particular sulfurized carbohydrates, as a possible major host of Re in organic-rich sediment (Morford et al., 2011). Although the pathway of Re enrichment in euxinic basins is much less explored, Helz and Dolor (2012) purposed a thiolation pathway similar to Mo that does not rely on ReO_4^- reduction. However, laboratory studies of Xu et al. (2000) show that such a pathway can be circumvented by reduction of ReO_4^- by SRB. Yamashita et al. (2007) have also confirmed that reduction of ReO_4^-, albeit in the absence of SRB, in reduced sediments is possible under controlled laboratory settings.

Although Os is similarly enriched in anoxic and euxinic sediments, if the rate of Re incorporation into OM of anoxic sediment exceeds that of Os, then this would induce an elemental fractionation effect. Given that Re shares similar geochemical affinities to Mo that are not expressed in Os, then preferentially incorporating Re over Os into sulfurized-OM seems likely, resulting in a predictive increase in Re/Os. Contrary to expectation, the absolute Re and Os concentrations vary between heavy and light isotope enrichment in both Upper and Basal Gordondale Member samples (Figure 8.6 A, B). However, when computing the relative distribution coefficients [see equation 1-3] between Re/Os in sulfurized-OM and non-sulfurized-OM (assuming heavy (sulfurized-OM) and light (non-sulfurized-OM) $\delta^{13}C_{kerogen}$ values as isotopic end-members) shows that K_dRe/Os values of sulfurized-OM exceed nonsulfurized-OM (KdRe/Os Upper Gordondale = 1.37; KdRe/Os Basal Gordondale = 2.86). This explains why $^{187}Re/^{188}Os$ of Upper and Basal Gordondale Member samples approximately correlate with heavy carbon

isotope enrichment (Figure 8.5, A,B), which is even more so the case when two out of the eleven samples in Fig. 8.5B are excluded as outliers that deviate from the trend line ($R^2 = 0.24$ to $R^2 = 0.86$).
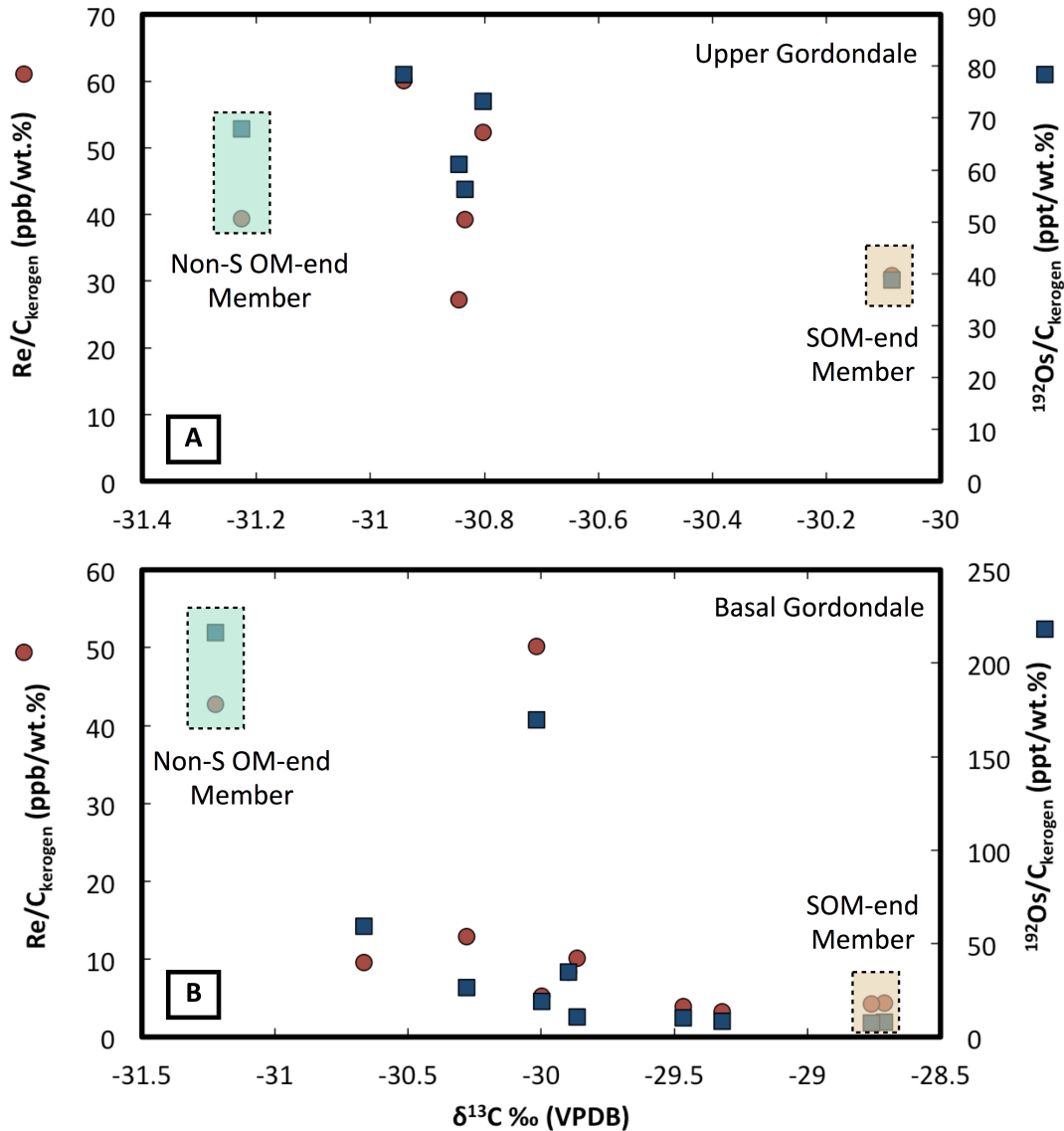
Figure 8. 6 Plots A and B depict the relationship between Re (ppb) and Os (ppt) concentration, $C_{kerogen}$ content (wt.%), and $\delta^{13}C_{kerogen}$ of Upper and Basal Gordondale samples. The green and orange boxes illustrate the assumed non-sulfurized OM and sulfurized-OM carbon isotopic-end members.

Equation 8.1:
$$^{SOM}K_{D[Re/Os]} = \frac{[Re/Os]_{SOM}}{[Re/Os]_{AQ}}$$

Equation 8.2:
$$^{OM}K_{D[Re/Os]} = \frac{[Re/Os]_{OM}}{[Re/Os]_{AQ}}$$

Equation 8.3:
$$^{SOM}K_{D[Re/Os]}\big/^{OM}K_{D[Re/Os]} = \frac{[Re/Os]_{SOM}}{[Re/Os]_{OM}}$$

These observations suggest that sulfurized-OM plays a complimentary part in Re/Os fractionation in ORS. If Re/Os fractionation scales proportionally with the degree of sulfurized-OM in anoxic and euxinic sediments, then this could viably account for the wide range of Re/Os ratios (100-5000) observed in anoxic sediment (Dubin and Peucker-Ehrenbrink; Georgiev et al., 2011). Furthermore, terrestrial coals (Type-III kerogens) deposited in comparably anoxic conditions of lacustrine environments exhibit both *lower* Re and Os concentrations and *lower* Re/Os ratios relative to their marine counterparts (Goswami et al., 2018), which confirms that sediment redox conditions cannot exclusively account for Re/Os fractionation in ORS. Rooney et al. (2011) purposed that coals lack specific organic chelating sites, otherwise preserved in Type I and Type II kerogens, that preferentially enable the sequestration of larger amounts of Re and Os. Yet besides major compositional differences, coals form in lacustrine environments, which are inherently sulfate limited (Sinninghe Damsté et al., 1993; Vandenbroucke and Largeau, 2007). This is in contrast to the large supply of sulfate in the marine environment, which may explain why marine-influenced coals are both heavily enriched in Re and Os and heavily fractionated in their ^{187}Re/^{188}Os ratios (Tripathy et al., 2015). Similarly, sulfidic terrestrial coals, such as Fire Clay Coals, have more dispersed Re/Os ratios than their terrestrial counterparts (Goswami et al., 2018).

Although sulfate is more abundant in the marine environment, its availability to react with and form sulfurized-OM will change in response to the amount of reactive Fe(II) available that would otherwise readily consume sulfate to form diagenetic pyrite (Vandenbroucke and Largeau, 2007). Anoxic sediments inundated with a large detrital flux, such as during the marine regression that marked the deposition of basal Poker Chip strata, will contain excess reactive

Fe(II) that will consume any available sulfide (HS⁻) derived from SRB, whereas during a marine transgression, such as during the deposition of basal Gordondale strata, a low detrital flux will stifle Fe(II) availability such that any excess sulfate will react with OM to form sulfurized-OM. This complex interplay between Fe(II) and sulfate availability exerts control over the types of biomacromolecules preserved in the kerogen (dominantly algaenan or a mixture of algaenan and sulfurized carbohydrates), the carbon isotopic composition of the kerogen, and the fractionation mechanisms of Re/Os in organic-rich sediment. This appears to be the discriminating factor between Basal Poker Chip and Gordondale strata with the former being comparably more clay-rich, iron-rich (i.e. pyrite), and OM –depleted (Riediger, 2002; Ross and Bustin, 2006). As a result, sulfurized-OM is unlikely to have contributed to the bulk kerogen content of basal Poker Chip strata (Ross and Bustin, 2006). Rather, terrestrial detritus comprised of ^{13}C enriched biomacromolecules, such as lignin, are far more likely to be present in the Type II kerogen of basal Poker Chip strata due to a larger influx of argillaceous sediment (Riediger, 2002; Ross and Bustin, 2006).

Despite the Gordondale Member being classified as Type I/II S-rich kerogen, small amounts of inertinite (i.e. coal) have been identified petrographically (Kondla et al., 2017; Riediger et al., 1990). This, therefore, opens the opportunity for inertinite to be present in kerogen of basal Poker Chip strata whose bulk sediment is more argillaceous-rich. Indeed, Riediger (2002) identified plant fragments in subsurface sections of basal Poker Chip Member strata overlying Gordondale and Nordegg Member strata. In addition, basal Poker Chip Member strata, both in outcrop and subsurface, contain Rock-Eval HI and OI values that overlap in range of Type III, terrestrial coal, kerogens indicating a flux of terrestrial biomass (Dembicki, 2009; Riediger, 2002).

A detrital flux of ^{13}C lignin component provides a possible solution of inducing small permil carbon isotopic shifts, which can plausibly account for the observed increased kerogen carbon content with heavy carbon isotope enrichment (Figure 8.7B). Similarly, a change in the relative proportions of algal-to-terrestrial organic matter also helps to explain both the relationship between Re/Os fractionation and light carbon isotope enrichment (Figure 8.7A),

since vascular plants are speculated to lack the necessary organic chelating sites required to preferentially sequester large amounts of Re and Os and induce large isotope fractionation effects. These observations support prior suppositions of Harris et al. (2013) that OM-type may influence Re/Os fractionation. Harris et al. (2013), for example, examined the Woodford Formation for Re/Os geochronology and observed the highest Re and Os concentrations and some of the largest Re/Os ratios in samples deposited in oxygenated waters that contain a mixture of marine- and terrestrial-sourced organic matter.
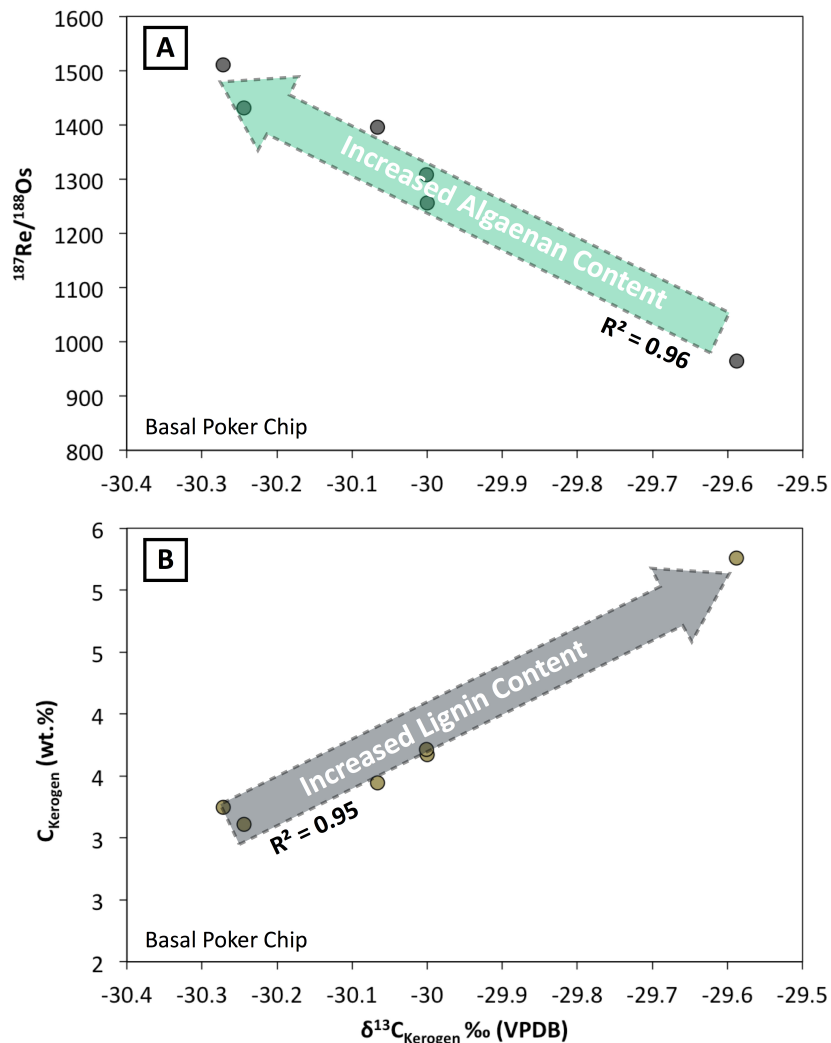
Figure 8. 7 Plot A and B illustrates the relationship between [187]Re/[188]Os fractionation, $C_{kerogen}$ content (wt.%), and $\delta^{13}C_{kerogen}$ in non-sulfurized OM of basal Poker Chip samples.

Alternatively, a second hypothesis may be proposed that does not invoke a relative change in the biomacromolecular content of kerogen, but rather a change in organic productivity of the water column. This hypothesis would viably account for the observed relationship between increased $C_{kerogen}$ content and heavy isotope enrichment in both Gordondale and Poker Chip samples. For example, algae preferentially sequester ^{12}C over ^{13}C during photosynthesis, leaving behind a residual pool of dissolve carbon depleted in ^{12}C in the photic zone (Hollander and McKenzie, 1991). Therefore, successive algal generations will become isotopically heavier due to a limiting supply of ^{12}C in the water column (Hollander and McKenzie, 1991).

Although this interpretation accounts for the positive relationship between $C_{kerogen}$ content and $\delta^{13}C_{kerogen}$, it fails to offer an explanation for the observed correlation between $^{187}Re/^{188}Os$ and $\delta^{13}C_{kerogen}$ values in basal Poker Chip Member and Gordondale Member samples, since $^{187}Re/^{188}Os$ ratios of basal Poker Chip Member and Gordondale Member samples show an inverse relationship between $\delta^{13}C_{kerogen}$ fractionation (Figure 8.5 and Figure 8.7). If organic productivity directly influenced $^{187}Re/^{188}Os$ fractionation in ORS by a simple increase in OM, then a positive relationship between $^{187}Re/^{188}Os$ and $\delta^{13}C_{kerogen}$ should be expressed in both data sets. Furthermore, there should be a positive correlation between TOC and $^{187}Re/^{188}Os$ fractionation in ORS (see Figure 8.3 plot C). However, $^{187}Re/^{188}Os$ fractionation is only poorly correlated with TOC in ORS (Dubin and Peucker-Ehrenbrink, 2015). Therefore, a relative change in biomacromolecular content of kerogen is the favoured hypothesis for driving Re/Os elemental fractionation in basal Poker Chip Member and Gordondale Member samples.

With that said, the mechanism of Re/Os fractionation in ORS remains to be conclusively established, and although the observations reported above are interesting, the conclusions should not be overstated. A possible solution to help either confirm or disprove a biomacromolecular-driven hypothesis would be characterization of the C/N ratios and S_{org} content of basal Poker Chip and Gordondale Member OM.

8.5.4 Gordondale Member Potential Source Rock For WCOS?

Petroleum generation, migration, and emplacement of hydrocarbon deposits of the Western Canadian Oil Sands (WCOS) have been bracketed via direct Re-Os dating of hydrocarbons to 112 ± 5.3 Ma (Selby and Creaser, 2005). Biomarkers evidence of Paleozoic and Cretaceous reservoirs implicates a single episode of petroleum generation coincident with the Cordilleran orogeny, which presumably expelled hydrocarbons from a (predominantly) single stratigraphic unit of WCSB (Creaney and Alan, 1990; Selby and Creaser, 2005). The Duvernay Formation (Late Devonian), the Exshaw Formation (Early Mississippian), Doig Formation (Triassic) and the Gordondale Member (Early Jurassic) are the four main purported candidate source rock contributors for the WCOS (Creaney and Allan, 1990). However, due to its high TOC content (up to 28 wt.%), H-rich organic matter, and biomarker geochemistry, the Gordondale Member was argued to have contributed the largest quantities of hydrocarbons (Creaney and Allan, 1990, 1991; Riediger, 1990; Riediger, 1994). This in part is related to the Type I/II-S kerogen of the Gordondale Member, particularly in the basal unit, which purportedly expanded the oil window, and resulted in a predominantly mature, oil-prone, subcrop (Creaney and Allan, 1990; Riediger, 1994).

Although inhibited by the overlying Poker Chip Member, Creaney and Allan (1990) postulated an oil flow pathway within the Middle Silty Unit of the Gordondale Member. This highly permeable conduit allowed oil to travel updip towards the eastern subcrop edge of the Gordondale Member, and expelled oil into Cretaceous sands of the Mannville Group, which subsequently supplied oil on a regional scale to the Athabasca, Cold Lake, and Peace River areas (Creaney and Allan, 1990). Riediger (1994), however, contested that biomarker evidence of the Athabasca and Cold Lake tar sands, contrary to Creaney and Allan (1990) assertions, were inconsistent with those found in the Gordondale Member. However, heavy oil, analogous to that of the WCOS, is a biodegraded form of light oil and likely decomposes any affiliate biomarkers (Barson et al., 2000). Therefore the use of biomarkers is insufficient evidence to rule out oil-to-source rock correlations. Mass balance estimates of the Exshaw Formation and

Gordondale, however, do contrast a single source for the WCOS. For example, expulsion of the Gordondale Member is estimated to have amounted to a mere 6.5% of the total oil emplaced in the Lower Cretaceous tar sands. Stratigraphic barriers inhibiting oil migration from the Gordondale Member to Athabasca and Cold Lake regions are also considered a major impediment to the Gordondale Member oil supply chain. The Peace River tar sands deposit was ruled as the only hydrocarbon deposits in logistical proximity to the Gordondale Member (Riediger, 1994). Riediger (1994) argued that these evidences reflected multiple, not single, source rock contributors to the WCOS, and that the Gordondale Member likely supplied only a fraction of the hydrocarbon present in the Peace River tar sands deposits. However, basin and migration models of Higley et al. (2009) and Berbesi et al. (2012) refute these stratigraphic barrier objections of Riediger (1994).

Recently, Finlay et al. (2012) employed a coupled geochemical approach of radioisotopic and elemental tracers, namely Os isotopes and PGE elementals, to re-examine each of the purported source rocks of the WCOS. Contrary to other tracer techniques (i.e. biomarkers), Os isotopes and PGE elemental ratios do not fractionate during oil generation or any subsequent biodegradation events (Finlay et al., 2012). This allows initial Os isotopic composition present in migratable hydrocarbons during oil generation (112 ± 5.3 Ma) to be used as effective oil-to-source rock tracers. Of the above stated source rocks, the Os isotopic composition during oil generation (Os_g) and coupled PGE elements of the Gordondale Member (Os_g = 1.04-2.8; Pt/Pd = ~ 0.4-1) are most consistent in range with hydrocarbons of the WCOS (Os_g = 1.4-1.7; Pt/Pd = 0.25-1.25) (Finlay et al., 2012). Os_g evidence, in turn, has eliminated the Duvernay Formation as a possible source rock and minimized the overall hydrocarbon contribution from the Exshaw Formation. This was shown to remain true even when using the antithetical petroleum generation model of 60 Ma (Finlay et al., 2012). The Os_g of the Gordondale Member from this study provides substantive evidence of Finlay et al. (2012) original conclusions (Table 9). Although this new evidence does not address the mass balance concerns presented by Riediger (1994), it does provide strong geochemical support of Creaney and Alan's (1990, 1991, 1992) single source rock hypothesis.

Organic carbon isotopes of kerogen provide another tool for discriminating oil-to-source rock correlations. If an oil-to-source rock correlation exists, then the $\delta^{13}C_{kerogen}$ signature of the bitumen in the WCOS may reflect the $\delta^{13}C_{kerogen}$ signature of the Gordondale Member. Jha et al. (1979) compiled a series of bitumen samples from the Athabasca and Cold Lake oil sands and analyzed their $\delta^{13}C$ content, which yielded values that ranged from -29.7 ‰ in Athabasca and -30.6 ‰ in Cold Lake. The $\delta^{13}C_{kerogen}$ of Upper and Lower Radioactive Unit Gordondale Member samples range from -28.71 and -31.22, which comparatively overlap within uncertainty of the $\delta^{13}C$ values of bitumen found in the Athabasca and Cold Lake hydrocarbon deposits. Similarities in $\delta^{13}C_{kerogen}$ remain true irrespective of hydrocarbon maturity. For example, samples from immature (TS0027 = -30.281 ‰) and mature (JT17-19202J = -30.665 ‰) regions exhibit indiscriminate $\delta^{13}C_{kerogen}$ values. Catagenesis tends to shift the $\delta^{13}C$ values of kerogen to more positive values by breaking ^{12}C-^{12}C bonds and liberating CO_2 (Sharp, 2017). The Gordondale Member has been shown to have a variable Hydrogen Index (HI), indicating both immature (high HI) and overmature (low HI) regions (Riediger, 1990). However, the effects of thermal maturation can only cause a finite amount of fractionation – with the most notable effects reflected in thermally overmature regions. This explains why both immature and mature samples in the Gordondale Member show statistically overlapping $\delta^{13}C$ values. It could be argued that overmature samples of the Gordondale Member would be isotopically lighter than immature and mature samples, thereby scrambling the $\delta^{13}C_{kerogen}$ signal and dissociating the apparent oil-to-source rock correlation presented here - although this hypothesis remains to be tested at the moment. Alternatively, biodegradation can play a role in fractionating the $\delta^{13}C_{org}$ signature. As oil breaks down into bitumen the isotopic signature shifts towards more negative values. Therefore, it could be argued that the precursor oil was isotopically heavier than the bitumen, and through biodegradation, the bitumen became isotopically lighter such that it appears to reflect the $\delta^{13}C$ values of Gordondale Member kerogen. Although this hypothesis cannot be fully ruled out, the coupled Os isotopic evidence provides assuring support that the $\delta^{13}C$ signature of source reflects that of the oil with minimal influence by biodegradation.

8.6 Conclusion

The kerogen carbon isotopic compositions of Gordondale Member and Poker Chip samples ranged from -29 to -30 ‰, which is similar to the organic carbon isotopic signature of bitumen from the WCOS. This evidence combined with previous literature results suggests that the Gordondale Member is a probably source rock for the WCOS. Furthermore, comparison of kerogen carbon isotopic compositions and $^{187}Re/^{188}Os$ values of ORS from the Gordondale and Poker Chip Member suggests that such a relationship exists. A tentative hypothesis to account for this relationship includes Re and Os being structurally bound to different combinations of biomacromolecules within the source kerogen that have distinct carbon isotopic signatures. Specifically, sulfurized-kerogens dominated by algal biomass (Type I) contain a ^{13}C-rich carbohydrate component that Re will preferentially partition into over Os, thereby inducing an elemental fractionation effect, whereas in Type-II kerogens Re will preferentially partition into the marine biomass (^{13}C-depleted) component over Os, which induces a similar elemental fractionation effect.

9 | Conclusion

9.1 Final Remarks and Future Considerations

This thesis focused on elucidating (1) the depositional ages of Early Jurassic shale beds of the Lower Fernie Formation (Chapter 5-6) via Re-Os chronostratigraphy, as well as (2) experimental investigations of Re and Os removal from USGS reference material SBC-1 by cold and hot (subcritical) water, and (3) explored the relationship between kerogen carbon isotope and Re/Os fractionation in ORS (Chapter 7).

1. Re-Os chronostratigraphy coupled with chemostratigraphy (Sr, Os) and biostratigraphy constrains the lower Gordondale Member (subunit 1A of Lower Radioactive Unit) to Late Sinemurian-Early Pliensbachian stages (190.14 ± 0.94 and 192.0 ± 1.4), intermediate sections of the Gordondale Member (subunit 1B of Lower Radioactive Unit) to Late Pliensbachian-Early Toarcian stages (183.9 ± 1.3), and the Gordondale-Poker Chip contact to the Late Toarcian (179.39 ± 0.60). These new high-precision ages constrain the deposition of the entire ~ 30 m stratigraphic section of the Gordondale Member in NW Alberta to 12.24 ± 1.92 Ma interval extending from the Late Sinemurian to the Late Toarcian. Fruitful areas of future exploration include: (1) detailed biostratigraphy of Gordondale Member cores outline in this study and (2) chemostratigraphy (C, Os, Sr) of the Lower Radioactive Unit (particularly of subunit 1A) to enhance global stratigraphic correlations.

2. Extraction of Re and Os from shale powders of USGS reference material SBC-1 by cold and hot (subcritical) water proved to be a successful non-destructive extraction technique for the removal of near-quantitative amounts of Re and Os at high extraction temperatures. However, only modest amounts of Re and Os was removed from SBC-1 at low extraction temperatures. Nonetheless the removal of Re and Os at both low and high extraction temperatures has important implications for Re and Os mobility in geologic settings including continental weathering and diagenesis. In

addition, Re was more efficiently leached from SBC-1 by water than Os at low extraction temperatures, which tentatively suggests differences in either bonding and/or residency are controlling this asymmetric behaviour. Future studies looking to build upon this research should explore the valence states and residency of Re and Os in ORS through some form of XANES and micro-imaging techniques.

3. Characterization of the kerogen carbon isotopic composition of Gordondale and Poker Chip Member samples reveals relatively homogenized organic carbon isotopic values ($\sim$ -29 to -31 ‰), which are consistent with organic carbon isotopic values of bitumen from the WCOS. This evidence combine with previous literature data implicates the Gordondale Member as one of the main source rocks for the WCOS. Furthermore, correlations between $\delta^{13}C_{kerogen}$ and $^{187}Re/^{188}Os$ fractionation suggests organic matter type may be influencing Re/Os fractionation in ORS. While speculative, this correlation may be related to different combinations of biomacromolecules within the source kerogen. In order to expand upon this research, future studies should explore the organic carbon isotopic composition of each discriminate biomacromolecule within the source kerogen of ORS in relation to $^{187}Re/^{188}Os$ fractionation to help resolve this knowledge gap.

References

Akinlua, A., and Smith, R.M. (2010) Subcritical water extraction of trace metals from petroleum source rock. Talanta, vol. 81, pp. 1346-1349.

Alberta's Energy Reserves 2005 and Supply/Demand Outlook 200602015; Alberta Energy and Utilities Board. http://www.ercb.ca (accessed 01/01/2016)

Allègre, C., and Luck, J.-M. (1980) Osmium isotopes as petrogenetic and geological tracers. Earth and Planetary Science Letters, vol. 48, pp. 148-154.

Anbar, A.D., Creaser, R.A., Papanastassiou, D.A., and Wasserburg, G.J. (1992) Rhenium in seawater: Confirmation of generally conservative behavior. Geochimica et Cosmochimica Acta Letter, vol. 56, pp. 4099-4103.

Asgar-Deen, M. (2003) Stratigraphy, Sedimentology and Paleogeography of the Lower Jurassic Nordegg Member (Gordondale Member), west-central Alberta, Canada. Master of Science Thesis. University of Calgary.

Asgar-Deen, M., Hall, R., Craig, J., and Riediger, C. (2003) New biostratigraphic data from the Lower Jurassic Fernie Formation in the subsurface of west-central Alberta and their stratigraphic implications. Canadian Journal of Earth Sciences, vol. 40, pp. 45-63.

Asgar-Deen, M., Riediger, C., and Hall, R. (2004) The Gordondale Member: designation of a new member in the Fernie Formation to replace the informal "Nordegg Member" nomenclature of the subsurface of west-central Alberta. Bulletin of Canadian Petroleum Geology, vol. 52, pp. 201-214.

Asgar-Deen (2018) Revision of Gordondale Member Pick at Maclean Creek. Personal Communications.

Barre, A.B., Prinzhofer, A., and Allegre, C.J. (1995) Osmium isotopes in the organic matter of crude oil and asphaltenes. Terra Abstracts, vol. 7, pp. 199.

Barson, D., Barlett, R., Hein, F., Fowler, M., Grasby, S., Riediger, and Underschultz (2000). Hydrogeology of heavy oil and tar sand deposits: Water flow and supply, migration and degradation, Field Trip Notes. Geological Survey of Canada, Open File Report 3946.

Berbesi, L.A., di Primio, R., Anka, Z., Horsfield, B., and Higley, D.K. (2012) Source rock contributions to the Lower Cretaceous heavy oil accumulations in Alberta: A basin modeling study: AAPG Bulletin, vol. 96, pp. 1211-1234.

Berglund, M., and Wieser, M.E. (2011) Isotopic compositions of the elements 2009 (IUPAC Technical Report). Pure and Applied Chemistry, vol. 83, pp. 397-410.

Beutel, E.K., Nomade, S., Fronabarger, A.K., and Renne, P.R. (2005) Pangaea's complex breakup: A new rapidly changing stress field model. Earth and Planetary Science Letters, vol. 236, pp. 471-485.

Biller, P., Ross, A.B., and Skill, S.C. (2015) Investigation of the presence of an aliphatic biopolymer in cyanobacteria: Implications for kerogen formation. Organic Geochemistry, vol. 81, pp. 64-69.

Birck, J.L., Barman, M.R., and Capmas, F. (1997) Re-Os Isotopic Measurements at the Femtomole Level in Natural Samples, vol. 20, p. 19-27.

Bodin, S., Mattioli, E., Frohlich, S., Marshall, J.D., Boutib, L., Lahsini, S., and Redfern, J. (2010) Toarcian carbon isotope shifts and nutrient changes from the Northern margin of Gondwana (High Atlas, Morcocco, Jurassic): Palaeoenvironmental implications. Palaeogeography, Palaeoclimatology, Palaeoecology, vol. 297, pp. 377-390.

Bowring, S.A., Schoene, B., Crowley, J.L., Ramezani, J., and Condon, D.J. (2006) High-precision U-Pb zircon geochronology and the stratigraphic record: progress and promise. Paleontological Society Papers, vol. 11, pp. 23-43.

Burwood, R., Drozd, R.J., Halpern, H.I., and Sedivy, R.A. (1988) Carbon isotopic variations of kerogen pyrolyzates. Organic Geochemistry, vol. 12, pp. 195-205.

Calvert, S.E., and Pedersen, T.F. (1993) Geochemistry of recent oxic and anoxic marine sediments: Implications for the geological record. Marine Geology, vol. 113, pp. 67-88.

Carlson, R.W. (2005) Application of the Pt-Re-Os isotopic systems to mantle geochemistry and geochronology. Lithos, vol. 82, pp. 249-272.

Chappaz, A., Lyons, T.W., Gregory, D.D., Reinhard, C.T., Gill, B.C., Li, Chao, Large, R.R. (2014) Does pyrite act as an important host for molybdenum in modern and ancient euxinic sediments? Geochimica et Cosmochimica Acta, vol 126, pp. 112-122.

Chikaraishi, Y. (2014) 13C/12C Signatures in Plants and Algae. In: Holland, H.D. and Turekian, K.K. Treatise on Geochemistry, Second Edition, pp. 95-123. Oxford: Elsevier

Cohen, A.S., Coe, A.L., Bartlett, J.M., and Hawkesworth, C.J. (1999) Precise Re-Os ages of organic-rich mudrocks and the Os isotope composition of Jurassic seawater. Earth and Planetary Science Letters, vol. 167, pp. 159-173.

Cohen, A.S., and Coe, A.L. (2002) New geochemical evidence for the onset of volcanism in the Central Atlantic magmatic province and environmental change at the Triassic-Jurassic boundary. Geology, vol. 30, pp. 267-270.

Cohen, A.S. (2004) The rhenium-osmium isotope system: applications to geochronological and paleoenvironmental problems. Journal of the Geological Society of London, vol. 161, pp. 729-734.

Cohen, A.S., and Coe, A.L. (2007) The impact of the Central Atlantic Magmatic Province on climate and on the Sr- and Os-isotope evolution of seawater. Paleogeography, Paleoclimatology, and Paleoecology, vol. 244, pp. 374-390.

Colodner, D., Sachs, J., Ravizza, G., Turekian, K., Edmond, J., and Boyle, E. (1993) The geochemical cycle of rhenium: a reconnaissance. Earth and Planetary Science Letters, vol. 117, pp. 205-221.

Creaney, S., and Allan, J. (1990) Hydrocarbon generation and migration in the Western Canada sedimentary basin. Geological Society Special Publication, pp. 189-202.

Creaser, R.A., Papanastassiou, D.A., and Wasserburg, G.J. (1990) Negative thermal ion mass spectrometry of osmium, rhenium, and iridium. Geochimica et Cosmochimica Acta, vol. 55, pp. 397-401.

Creaser, R.A., Sannigraphi, P., Chacko, T., and Selby, D. (2002) Further evaluation of the Re-Os geochronometer in organic-rich sedimentary rocks: A test of hydrocarbon maturation effects in the Exshaw Formation, Western Canada Sedimentary Basin. Geochimica et Cosmochimica Acta, vol. 66, pp. 3441-3452.

Crusius, J., Calvert, S., Pedersen, T., and Sage, D. (1996) Rhenium and molybdenum enrichments in sediments as indicators of oxic, suboxic, and sulfidic conditions of deposition. Earth and Planetary Science Letters, vol. 145, pp. 65-78.

Crusius, J., and Thomson, J. (2000) Comparative behavior of authigenic Re, U, and Mo during reoxidation and subsequent long-term burial in marine sediments. Geochimica et Cosmochimica Acta, vol. 64, pp. 2233-2242.

Cumming, V.M., Selby, D., Lillis, P.G., and Lewan, M.D. (2014) Re-Os geochronology and Os isotope fingerprinting of petroleum sourced from a Type I lacustrine kerogen: Insights from the natural Green River petroleum system in the Uinta Basin and hydrous pyrolysis experiments. Geochimica et Cosmochimica Acta, vol. 138, pp. 32-56.

Dabek, J., and Halas, S. (2007) Physical Foundations of Rhenium-Osmium Method – A Review. Geochronometria, vol. 27, pp. 23-26.

Dembicki, J. H. (2009) Three common source rock evaluation errors made by geologists during prospect or play appraisals. AAPG Bulletin, vol. 93, pp. 341-356.

Dickin, A.P. (2018) Radiogenic Isotope Geology Third Edition. United States of America, Cambridge University Press.

Duarte, L.V., Silva, R.L., Oliveira, L.C.V., Comas-Rengifo, and Silva, F. (2010) Organic-rich facies in the Sinuemurian and Pliensbachian of the Lusitanian Basin, Portugal: Total organic carbon distribution and relation to transgressive-regressive facies cycles. Geologica Acta, vol. 8, pp. 325-340.

Duarte, L.V., Silva, R.L., Mendonca Filho, J.G., Pocas Ribeiro, N., and Chagas, R.B.A. (2012) High-resolution stratigraphy, palynofacies and source rock potential of the Agua De Madeiros Formation (Lower Jurassic), Lusitanian Basin, Portugal. Journal of Petroleum Geology, vol., 35, pp. 105-126.

Dubin, A., and Peucker-Ehrenbrink, B. (2015) The importance of organic-rich shales to the geochemical cycles of rhenium and osmium. Chemical Geology, vol. 403, pp. 111-120.

Durand, B. (1980) Kerogen-Insoluble Organic Matter from Sedimentary Rocks. Paris: Editions Technip.

Eglinton, T.I. (1994) Carbon isotopic evidence for the origin of macromolecular aliphatic structures in kerogen. Organic Geochemistry, vol. 21, pp. 721-735.

Esser, B., and Turekian, K.K. (1993) The osmium isotopic composition of the continental crust. Geochimica et Cosmochimica Acta, vol. 57, pp. 3093-3104.

Finlay, A., Selby, D., and Osborne, M.J. (2012) Petroleum source rock identification of United Kingdom Atlantic Margin oil fields and the Western Canadian Oil Sands using Platinum, Palladium, Osmium and Rhenium: Implications for global petroleum systems. Earth and Planetary Science Letters, vol. 313-314, pp. 95-104.

Frebold, H. (1957) The Jurassic Fernie Group in the Canadian Rocky Mountains and Foothills. Geological Survey of Canada, Memoir 287, pp. 187.

Frebold, H. (1970) Pliensbachian Ammonoids from British Columbia and southern Yukon. Canadian Journal of Earth Sciences, vol. 7.

Garrels, R.M., Mackenzie, F.T. (1969) Sedimentary rock types: relative proportions as a function of geological time. Science, vol. 163, pp. 570-571.

Gelin, F., Boogers, I., Noordeloos, A.A.M., Sinninghe Damste, J.S., Hatcher, P.G., De Leeuw, J.W. (1996) Novel, resistant microalgal polyethers: An important sink of organic carbon in the marine environment? Geochimica et Cosmochimica Acta, vol. 60, pp. 1275-1280.

Georgiev, S.V., Stein, H.J, Hannah, J.L., Bingen, B., Weiss, H.M., and Piasecki, S. (2011) Hot acidic Late Permian seas stifle life in record time. Earth and Planetary Science Letters, vol. 310, pp. 389-400.

Georgiev, S., Stein, H.J., Hannah, J.L., Weiss, H.M., Bingen, B., Xu, G., Rein, E., Hatlo, V., Loseth, H., Nali, M., Piasecki, S. (2012) Chemical signals for oxidative weathering predict Re-Os isochroneity in black shales, East Greenland. Chemical Geology, vol. 324-325, pp. 108-121.

Georgiev, S.V., Stein, H.J., Hannah, J.L., Xu, G., Bingen, B., and Weiss, H.M. (2017) Timing, duration, and causes for Late Jurassic-Early Creaceous anoxia in the Barents Sea. Earth and Planetary Science Letters, vol. 461, pp. 151-162.

Gómez, J.J., Comas-Rengifo, M.J., and Goy, A. (2016) The hydrocarbon source rocks of the Pliensbachian (Early Jurassic) in the Asturian Basin (northern Spain): Their relationship with the paleoclimatic oscillations and gamma-ray response. Journal of Iberian Geology, vol. 42, pp. 259-273.

Goswami, V., Hannah, J.L., and Stein, H.J. (2018) Why terrestrial coals cannot be dated using the Re-Os geochronometer: Evidence from the Finnmark Platform, southern Barents Sea and the Fire Clay coal horizon, Central Appalachian Basin. International Journal of Coal Geology, vol. 188, pp. 121-135.

Goth, K., De Leeuw, J.W., Puttmann, W., and Tegelaar, E.W. (1988) Origin of Messel Oil Shale kerogen. Nature, vol. 336, pp. 22-29.

Gröcke, D.R., Hesselbo, S.P., and Findlay, D.J. (2007) Atypical diagenetic effects on strontium-isotope composition of Early Jurassic belemnites, Queen Charlotte Islands, British Columbia, Canada. Canadian Journal of Earth Sciences, vol. 44, pp. 181-197.

Gradstein, F. M. (2012). *The Geologic time scale 2012.* [Oxford, U.K.]: Elsevier

Hall, R.L. (1984) Lithostratigraphy and biostratigraphy of the Fernie Formation (Jurassic) in the Southern Canadian Rocky Mountains. Canadian Society of Petroleum Geologists, vol. 9, pp. 233-247.

Hall, R.L. (1987) New Lower Jurassic ammonite faunas from the Fernie Formation, southern Canadian Rocky Mountains. Canadian Journal of Earth Sciences, vol. 24, p. 1688-1704.

Hall, R.L., Kendall, D.R, Taylor, D.G., and Craig, J. (2000) A new ammonite and coccolith fauna from the lowermost Fernie Formation (Hettangian) in northwestern Alberta, Canada. Canadian Journal Earth Science, vol. 37, p. 1378-1376.

Hall, R., and Pitaru, S. (2003) New Hettangian Ammonite Faunas and A Triassic Jurassic Boundary Succession, Fernie Formation, Williston Lake, British Columbia. Rivista Italiana di Paleontologia e Stratigrafia, vol. 110, pp. 53-60.

Hall, R., Mcnicoll, V., Gröcke, D., Craig, J, and Johnston, K. (2003) Integrated stratigraphy of the lower and middle Fernie in Alberta and British Columbia, Western Canada. Rivista Italiana di Paleontologia e Stratigrafia, vol. 110, pp. 61-68.

Hall, R. (2006) New, biostratigraphically significant ammonites from the Jurassic Fernie Formation, southern Canadian Rocky Mountains. Canadian Journal of Earth Sciences, vol. 43, pp. 555-570.

Hannah J.L., and Stein H.J. (2002) Re-Os model for the origin of sulfide deposits in anorthosite-associated intrusive complexes. Economic Geology, vol. 97, pp.371–383.

Haq, B.U. (2017) Jurassic Sea-level Variations: A Reappraisal. Geological Society of America, vol. 28.

Harris, H.B., Mnich, C.A., Selby, D., and Korrn, D. (2013) Minor and trace element and Re-Os chemistry of the Upper Devonian Woodford Shale, Permian Basin, west Texas: Insights into metal abundance and basin processes. Chemical Geology, vol. 356, pp. 76-93.

Hatcher, P.G., Spiker, E.C., Szeverenyi, N.M., and Maciel, G.E. (1983). Selective preservation and origin of petroleum-forming aquatic kerogen. Nature, vol. 305, pp. 498-501.

Helz, G.R., Miller, C.V., Charnock, J.M., Mosselmans, J.F.W., Pattrick, R.A.D., Garner, C.D., and Vaughan, D.J. (1996) Mechanism of molybdenum removal from the sea and its concentration in black shales: EXAFS evidence. Geochimica et Cosmochimica Acta, vol. 60, pp. 3631-3642.

Helz, G.R., and Dolor, M.K. (2012) What regulates rhenium deposition in euxinic basins? Chemical Geology, vol. 304-305, pp. 131-141.

Hesselbo, S.P., Gröcke, D.R., Jenkyns, H.C., Bjerrum, C.J., Farrimond, P., Morgans Bells, H.S., and Green, O.R. (2000) Massive dissociation of gas hydrate during a Jurassic oceanic anoxic event. Nature, vol. 406, pp. 392-395.

Higley, D.K., Lewan, M.D., Roberts, L.N.R., and Henry, M. (2009) Timing and petroleum sources for the Lower Cretaceous Mannville Group oil sands of northern Alberta based on 4-D modeling. AAPG Bulletin, vol. 93, pp. 203-230.

Höld, L.M., Schouten, S., Van Kaam-Peters, M.E., and Sinninghe Damsté, J.S. (1998) Recognition of n-alkyl and isoprenoid algaenans in marine sediments by stable carbon isotopic analysis of pyrolysis products of kerogens. Organic Geochemistry, vol. 28, pp. 179-194.

Hollander, D.J., and McKenzie, J.A. (1991) CO_2 control on carbon-isotope fractionation during aqueous photosynthesis: A paleo-pCO_2 barometer. Geology, vol. 19, pp. 929-932.

Jaffe, L.A., Peucker-Ehrenbrink, B., and Petsch, S.T. (2002) Mobility of rhenium, platinum group elements and organic carbon during black shale weathering. Earth and Planetary Science Letters, vol. 198, pp. 339-353.

Jenkyns, H.C., Jones, C.E., Gröcke, D.R., Hesselbo, S.P., and Parkinson, D.N. (2002) Chemostratigraphy of the Jurassic System: applications, limitations and implications for palaeoceanography. Journal of the Geological Society, London, vol. 159, pp 351-378.

Jenkyns, H.C. (2010) Geochemistry of oceanic anoxic events. Geochemistry, Geophysics, Geosystems, vol. 11, pp. 1525-2027.

Jha, K.N., Gray, J., and Strausz, O.P. (1979) The isotopic composition of carbon in the Alberta oil sand. Geochimica et Cosmochimica Acta, vol. 43, pp. 1571-1573.

Jones, C.E., Jenkyns, H.C., and Hesselbo, S.P. (1994) Strontium isotopes in Early Jurassic seawater. Geochimica et Cosmochimica Acta, vol. 58, pp. 1285-1301.

Jourdan, F., Marzoli, A., Bertrand, H., Cirilli, S., Tanner, L.H., Kontak, D.J., McHone, G., Renne, P.R., and Bellieni, G. (2009) 40Ar/39Ar ages of CAMP in North America: Implications for the Triassic-Jurassic boundary and the 40K decay constant bias. Lithos, vol. 110, pp 167-180.

Kaufman, A.J., Knoll, A.H. (1995) Neoproterozoic variations in the C-isotopic composition of seawater: stratigraphic and biogeochemical implications. Precambrian Research, vol. 73, pp. 27-49.

Kendall, B.S., Creaser, R.A., Ross, G.M., and Selby, D. (2004) Constraints on the timing of Marinoan "Snowball Earth" glaciation by [187]Re-[188]Os dating of a Neoproterozoic, post-

glacial black shale in Western Canada. Earth and Planetary Science Letters, vol. 222, pp. 729-740.

Kendall, B., Creaser, R.A., and Selby, D. (2006) Re-Os geochronology of postglacial black shales in Australia: Constraints on the timing of "Sturtian" glaciation. Geology, vol. 34, pp. 729-732.

Kendall, B., Creaser, R.A., and Selby, D. (2009) ^{187}Re-^{187}Os geochronology of Precambrian organic-rich sedimentary rocks. The Geological Society of London, vol. 326, pp. 85-107.

Kendall, B., Creaser, R.A., Gordon, G.W., and Anbar, A.B. (2009) Re-Os and Mo isotope systematics of black shales from the Middle Proterozoic Velkerri and Wollogorang Formations, McArthur Basin, northern Australia. Geochimica et Cosmochimica Acta, vol. 73, pp. 2534-2558.

Koide, M., Hodge, V.F., Yang, J.S., Stallard, M., Goldberg, E.G., Calhoun, J., and Bertine, K.K. (1986) Some comparative marine chemistries of rhenium, gold, silver, and molybdenum. Applied Geochemistry, vol. 1, pp. 705-714.

Koide, M., Goldberg, E.D., Niemeyer, S., Gerlach, D., Hodge, V., Bertine, K.K, and Padova, A. (1991) Osmium in marine sediments. Geochimica et Cosmochimica Acta, vol. 55, pp. 1641-1648.

Kondla, D., Sanei, H., Clarkson, C.R., and Goodarzi, F. (2017) High resolution characterization of a core from the Lower Jurassic Gordondale Member, Western Canada Sedimentary Basin. Marine and Petroleum Geology, vol. 83, pp. 50-59.

Korte, C., Hesselbo, S.P. (2011) Shallow marine carbon and oxygen isotope and elemental records indicate icehouse-greenhouse cycles during Early Jurassic. Palaeoceanography, vol. 26, pp. 4219.

Kuroda, J., Hori, R.S., Suzuki, K., Gröcke, D.R., and Ohkouchi, N. (2010) Marine osmium isotope record across the Triassic-Jurassic boundary from a Pacific pelagic site. Geology, vol. 38, pp. 1095-1098.

Levasseur, S., Birck, J.-L., and Allègre, C.J. (1999) The osmium riverine flux and the oceanic mass balance of osmium. Earth and Planetary Science Letters, vol. 174, pp. 7-23.

Lewan, M.D. (1983) Effects of thermal maturation on stable organic carbon isotopes as determined by hydrous pyrolysis of Woodford Shale. Geochimica et Cosmochimica Act, vol. 47, pp. 1471-1479.

Lewan, M.D. (1986) Stable carbon isotopes of amorphous kerogens from Phanerozoic sedimentary rocks. Geochimica et Cosmochimica Acta, vol. 50, pp. 1583-1591.

Li, C., Qu, W., Du, A., and Sun, W. (2009) Comprehensive study on extraction of rhenium with acetone in Re-Os isotopic dating. Rock Mineralogical Analysis, vol. 22, pp. 233-238 (in Chinese, with English abstract).

Li, D., Shields-Zhou, G.A., Ling, H-F., and Thirlwall, M. (2011) Dissolution methods for strontium isotope stratigraphy: Guidelines for the use of bulk carbonate and phosphorite rocks. Chemical Geology, vol. 290, pp. 133-144.

Little, C.T.S., and Benton, M.J. (1995) Early Jurassic mass extinction: A global long-term event. Geology, vol. 23, pp. 495-498.

Longridge, L.M., Smith, P.L., and Tipper, H.W. (2008) Late Hettangian (Early Jurassic) ammonites from Taseko Lakes, British Columbia, Canada.

Ludwig, K.R. (2012) User's Manual for Isoplot 3.75. A Geochronological Toolkit for Microsoft Excel. Berkeley Geochronological Center. kludwig@bgc.org (accessed: 01/04/2016)

Markey, R., Stein, H.J., Hannah, J.L., Georgiev, S.V., Pedersen, J.H., and Dons, C.E. (2016) Re-Os identification of glide faulting and precise ages for correlation from the Upper Jurassic Hekkingen Formation, southwestern Barents Sea. Palaeogeography, Palaeoclimatology, Palaeoecology, vol. 466, pp. 209-220.

Mattioli, E., and Erba, E. (1999) Synthesis of Calcareous Nannofossil Events in the Tethyan Lower and Middle Jurassic Succession. Rivista Italiana di Paleontologia e Stratigrafia, vol. 105, pp 343-376.

Mazzini, A., Svensen, H., Leanza, H.A., Corfu, F., and Planke, S. (2010) Early Jurassic shale chemostratigraphy and U-Pb ages from the Neuquen Basin (Argentina): Implication for the Toarcian Ocean Anoxic Event. Earth and Planetary Science Letters, vol. 297, pp. 633-645.

McArthur, J.M., Donovan, D.T., Thirlwall, M.F., Fouke, B.W., and Mattey, D. (2000) Strontium isotope profile of the early Toarcian (Jurassic) oceanic anoxic event, the duration of ammonite biozones, and belemnite palaeotemperatures. Earth and Planetary Science Letters, vol. 179, pp. 269-285.

McArthur, J.M., Algeo, T.J., van de Schootbrugge, D., Li, Q., and Howarth, R.J. (2008) Basinal restriction, black shales, Re-Os dating, and the Early Toarcian (Jurassic) oceanic anoxic event. Paleoceanography, vol. 23, pp. 1-22.

Meisel, T., Walker, R.J., Morgan, J.W. (1996) The osmium isotopic composition of the Earth's primitive upper mantle. Nature, vol. 383, pp. 517-520.

Meister, C., Aberhan, M, Blau, J., Dommergues, J.-L., Feist-Burkhardt, S., Hailwood, E.A., Hart, M., Hesselbo, S., Hounslow, M.W., Hylton, M., Morton, N., Page, K., and Price, G.D. (2006) The Global Boundary Stratotype Section and Point (GSSP) for the base of the Pliensbachian Stage (Lower Jurassic), Wine Haven, Yorkshire, UK. Episodes, vol. 29, pp. 93-106.

Merino-Tome, O., Della Porta, G., Kenter, J.A.M., Verwer, K., Harris, P.M., Adams, E.W., Playton, T., and Corrochano, D. (2012) Sequence development in an isolated carbonate platform (Lower Jurassic, Djebel bou Dahar, High Atlas, Morocco): influence of tectonics, eustacy and carbonate production. Sedimentology, vol. 59, pp. 118-155.

Morford, J.L., and Emerson, S. (1999) The geochemistry of redox sensitive trace metals in sediments. Geochimica et Cosmochimica Acta, vol. 63, pp. 1735-1750.

Morford, J.L., Martin, W.R., Kalnejais, L.H., Francois, R., Bothner, M., Karle, I.-M., (2007) Insights on geochemical cycling of U, Re, and Mo from seasonal sampling in Boston Harbor, Massachusetts, USA. Geochimica et Cosmochimica Acta, vol. 71, pp. 895-917.

Morford, J.L., Martin, W.R., and Carney, C.M. (2011) Rhenium geochemical cycling: Insights from continental margins. Chemical Geology, vol. 324-325, pp. 73-86.

Nomade, S., Knight, K.B., Beutel, E., Renne, P.R., Verati, C., Feraud, G., Marzoli, A., Youbi, N., and Bertrand, H. (2006) Chronology of the Central Atlantic Magmatic Province: Implications for the Central Atlantic rifting processes and the Triassic-Jurassic biotic crisis. Palaeogeography, Palaeoclimatology, Palaeoecology, vol. 244, pp. 326-344.

Ogg, J. G, Ogg, G., & Gradstein, F. M. (2016). *A concise geologic time scale 2016.* Amsterdam, Netherlands: Elsevier.

Pálfy, J., Smith, P.L., Mortensen, J.K., and Friedman, R.M. (1999) Integrated ammonite biochronology and U-Pb geochronometry from a basal Jurassic section in Alaska. Geological Society of America Bulletin, vol. 111, pp. 1537-1549.

Pálfy, J., Mortensen, J.K., Smith, P.L., Friedman, R.M., McNicoll, V., and Villeneuve, M. (2000) New U-Pb zircon ages integrated with ammonite biochronology from the Jurassic of the Canadian Cordillera. Canadian Journal of Earth Sciences, vol. 37, pp. 549-567.

Pálfy, J., Smith, P.L., and Mortensen, J.K. (2000) A U-Pb and 40Ar/39Ar time scale for the Jurassic. Canadian Journal of Earth Sciences, vol. 37, pp. 923-944.

Panǎ, D.I., Poulton, T.P., and DuFrane, S.A. (2018a) U-Pb detrital zircon dating supports Early Jurassic initiation of the Cordilleran foreland basin in southwestern Canada. GSA Bulletin, doi: https://doi-org.login.ezproxy.library.ualberta.ca/10.1130/B31862.1

Panǎ, D.I., Poulton, T., and Heaman, L. (2018b) U-Pb zircon ages of volcanic ashes integrated with ammonite biostratigraphy, Fernie Formation (Jurassic), Western Canada, with implications for Cordilleran-Foreland basin connections and comments on the Jurassic time scale. Canadian Petroleum Geology Bulletin, *in press*.

Percival, L.M.E, Cohen, A.S., Davies, M.K., Dickson, A.J., Hesselbo, S.P., Jenkyns, H.C., Leng, M.J., Mather, T.A., Storm, M.S., and Xu, W. Osmium isotope evidence for two pulses of increased continental weathering linked to Early Jurassic volcanism and climate change. Geology, vol. 44, pp. 759-762.

Peti, L., Thibault, N, Clemence, M.-E., Korte, C., Dommergues, J.-L., Bougeault, C., Pellenard, P., Jelby, M.E., and Ullmann, C.V. (2016) Sinemurian-Pliensbachian calcareous nannofossil biostratigraphy and organic carbon isotope stratigraphy in the Paris Basin: Calibration to the ammonite biozoniation of NW Europe. Paleogeography, Paleoclimatology, and Paleoecology, vol. 468, pp. 142-161.

Peucker-Ehrenrink, B, and Ravizza, G. (2000) The marine osmium isotope record. Terra Nova, vol. 12, pp. 205-219.

Philp, R.P. (2014) Formation and Geochemistry of Oil and Gas. In: Holland, H.D. and Turekian, K.K (eds) Treatise on Geochemistry, Second Edition, vol. 9, p. 233-265. Oxford: Elsevier.

Plancq, J., Mattioli, E., Pittet, B., Baudin, F., Duarte, L.V., Boussaha, M., and Grossi, V. (2016) A calcareous nannofossil and organic geochemical study of marine paleoenvironmental changes across the Sinemurian/Pliensbachian (early Jurassic, ~ 191 Ma) in Portugal. Paleogeography, Paleoclimatology, Paleoecology, vol. 499, pp. 1-12.

Poirier, A., and Hillaire-Marcel, C. (2011) Improve Os-isotope stratigraphy of the Arctic Ocean. Geophysical Research Letters, vol. 38, pp. L14607.

Porter, S.J., Selby, D., Suzuki, K., and Gröcke, D. (2013) Opening of trans-Pangaean marine corridor during the Early Jurassic: Insights from osmium isotopes across the Sinemurian-Pliensbachian GSSP, Robin Hood's Bay, UK. Paleogeography, Paleoclimatology, Paleoecology, vol. 375, pp. 50-58.

Porter, S.J., Smith, P.L., Caruthers, A.H., Hou, P., Gröcke, D.R., and Selby, D. (2014) New high resolution geochemistry of Lower Jurassic marine sections in western North America:

global positive carbon isotope excursion in the Sinemurian? Earth and Planetary Science Letters, vol. 397, pp. 19-31.

Poulton, T.P., Tittemore, J., and Dolby, G. (1990) Jurassic strata of northwestern (and west-central) Alberta and northeastern British Columbia. Bulletin of Canadian Petroleum Geology, vol. 38A, pp. 159-175.

Poulton, T.P., Christopher, J.E., Hayes. B.J.R., Loster, J., Tittemore, J., and Gilchrist, R.D. (1994) Jurassic and Lowermost Cretaceous Strata of the Western Canada Sedimentary Basin.

Racionero-Gomez, B., Sproson, A.D., Selby, D., Gannoun, A., Gröcke, D.R., Greenwell, H.C., and Burton, K.W. (2016) Osmium uptake, distribution, and 187Os/188Os and 187Re/188Os compositions in Phaeophyceae macroalge, Fucus vesiculosus: Implications for determining the 187Os/188Os composition of seawater. Geochimica et Cosmochimica Acta, vol. 199, pp. 48-57.

Tripathy, G.R., Hannah, J.L., Stein, H.J., Geboy, N.J., and Ruppert, L.F. (2015) Radiometric dating of marine-influenced coal using Re-Os geochronology, vol. 432, pp. 13-23.

Ravizza, G., and Turekian, K.K. (1989) Application of the 187Re-188Os system to black shale geochronometry. Geochimica et Cosmochimica Acta, vol. 53, pp. 3257-3262.

Ravizza, G., Turekian, K.K., and Bay, B.J. (1991) The geochemistry of rhenium and osmium in recent sediments from the Black Sea. Geochimica et Cosmochimica Acta, vol. 55, pp. 3741-3752.

Redding, C.E., Schoell, M., Monin, J.C., and Durand, B. (1980) Hydrogen and carbon isotopic composition of coals and kerogens. Physics and Chemistry of the Earth, vol. 12, pp. 711-723.

Riding, J.B., Leng, M.J., Kender, S., Hesselbo, S.P., Feist-Burkhardt, S. (2013) Isotopic and palynological evidence for a new Early Jurassic environmental perturbation. Palaeogeography, Palaeoclimatology, Palaeoecology, vol. 374, pp. 16-27.

Riediger, C.L. (1990) Rock-Eval/TOC data from the Lower Jurassic "Nordegg Member", and the Lower and Middle Triassic Doig and Montney Formations, Western Canada Sedimentary Basin, Alberta and British Columbia. Geological Survey of Canada, Open File 2308.

Riediger, C.L., Fowler, M.G., Snowdon, L.R., Goodarzi, F., and Brooks, P.W. (1990) Source rock analysis of the Lower Jurassic "Nordegg Member" and oil-source rock correlations, northwestern Alberta and northeastern British Columbia. Bulletin of Canadian Petroleum Geology, vol. 38A, pp. 236-249.

Riediger, C.L., and Coniglio, M. (1992) Early diagenetic calcites and associated bitumens in the "Nordegg Member": implication for Jurassic paleogeography of the Western Canada Sedimentary Basin. Bulletin of Canadian Petroleum Geology, vol. 40, p. 381-394.

Riediger, C.L. (1993) Solid bitumen reflectance and Rock-Eval T_{max} as maturation indices: an example from the "Nordegg Member", Western Canada Sedimentary Basin. International Journal of Coal Geology, vol. 22, pp. 295-315.

Riediger, C.L. (1994) Migration of "Nordegg" oil in the Western Canada Basin. How much and how far? Bulletin of Canadian Petroleum Geology, vol. 42, pp. 63-73.

Riediger, C.L., and Bloch, J.D. (1995) Depositional and Diagenetic Controls on Source-rock Characteristics of the Lower Jurassic "Nordegg Member", Western Canada. Journal of Sedimentary Research, vol. A65, pp. 112-126.

Riediger, C.L. (2002) Hydrocarbon source rock potential and comments on correlation of the Lower Jurassic Poker Chip Shale, west-central Alberta. Bulletin of Canadian Petroleum Geology, vol. 50, pp. 263-276.

Rooney, A.D., Selby, D., Houzay, J.-P., and Renne, P.R. (2010) Re-Os geochronology of a Mesoproterozoic sedimentary succession, Taoudeni basin, Mauritania: Implications for basin-wide correlations and Re-Os organic-rich sediments systematics. Earth and Planetary Science Letters, vol. 289, pp. 486-496.

Rooney, A.D, Selby, D., Lewan, M.D., Lillis, P.G., and Houzay, J-P. (2012) Evaluating Re-Os systematics in organic-rich sedimentary rocks in response to petroleum generation using hydrous pyrolysis experiments. Geochimica et Cosmochimica Acta, vol. 77, pp. 275-291.

Rooney, A.D., Selby, D., Lloyd, J.M., Roberts, D.H., Luckge, A., Sageman, B.B., and Prouty, N.G. (2016) Tracking millennial-scale Holocene glacial advance and retreat using osmium isotopes: Insights from the Greenland ice sheet. Quaternary Science Reviews, vol. 138, pp. 49-61.

Ross, D.J.K, and Bustin, R.M. (2006) Sediment geochemistry of the Lower Jurassic Gordondale Member, northeastern British Columbia. Bulletin of Canadian Petroleum Geology, vol. 54, pp. 337-365.

Ruhl, M., Hesselbo, S.P, Hinnov, L., Jenkyns, H.C., Xu, W., Riding, J.B., Storm, M., Minisini, D., Ullmann, C.V., and Leng, M.J. (2016) Astronomical constraints on the duration of the Early Jurassic Pliensbachian Stage and global climatic fluctuations. Earth and Planetary Science Letters, vol. 455, pp. 149-165.

Sato, Honami, Onoue, T., Nozaki, T., and Suzuki, K. (2013) Osmium isotope evidence for a large late Triassic impact event. Nature Communications.

Scotese, C.R. (2014) Atlas of Jurassic Paleogeographic Maps, PALEOMAP Atlas for ArcGIS, volume 4, The Jurassic and Triassic, Maps 32-42, Mollweide Projection, PALEOMAP Project, Evanston, IL.

Selby, D., and Creaser, R.A. (2003) Re-Os geochronology of organic rich sediments: an evaluation of organic matter analysis methods. Chemical Geology, vol. 200, pp. 225-240.

Selby, D., and Creaser, R.A. (2005) Direct Radiometric Dating of Hydrocarbon Deposits Using Rhenium-Osmium Isotopes. Science, vol. 308, pp. 1293-1295.

Selby, D., and Creaser, R.A. (2005) Direct radiometric dating of the Devonian-Mississippian time-scale boundary using the Re-Os black shale geochronometer. Geology, vol. 33, pp. 545-548.

Selby, D., Creaser, R.A., Stein, H.J., Markey, R.J., Hannah, J.L. (2007) Assessment of the 187Re decay constant by cross calibration of Re-Os molybdenite and U-Pb zircon chronometers in magmatic ore systems. Geochimica et Cosmochimica Acta, vol. 71, pp. 1999-2013.

Selby, D. (2007) Direct Rhenium-Osmium age of the Oxfordian-Kimmeridgian boundary, Staffin bay, Isle of Syke, U.K., and the Late Jurassic time scale. Norwegian Journal of Geology, vol. 87, pp. 291-299.

Sell, B., Ovtcharova, M., Guex, J., Bartolini, A., Jourdan, F., Spangenberg, J.E., Vicente, J.-C., and Schaltegger, U. (2014) Evaluating the temporal link between the Karoo LIP and climatic-biologic events of the Toarcian Stage with high-precision U-Pb geochronology. Earth and Planetary Science Letters, vol. 408, pp. 48-56.

Sharma, M., Wasserburg, G.J., Hofmann, A.W., and Butterfield, D.A. (2000) Osmium isotopes in hydrothermal fluids from the Juan de Fuca Ridge. Earth and Planetary Science Letters, vol.179, pp. 139-152.

Sharp, Z. (2007) Principles of Stable Isotope Geochemistry. Pearson Prentice Hall, United States of American, chapter 7. pp. 9.

Shen, J.J., Papanastassiou, D.A., and Wasserburg, G.J. (1996) Precise Re-Os determinations and systematics of iron meteorites. Geochimica et Cosmochimica Acta, vol. 60, pp. 2887-2900.

Shirey, S.B., and Walker, R.J. (1995) Carius tube digestions for low-blank rhenium-osmium analysis. Analytical Chemistry, vol. 67, pp. 2136-2141.

Shirey, S.B., and Walker, R.J. (1998) The Re-Os Isotope System in Cosmochemistry and High-Temperature Geochemistry. Annual Review of Earth and Planetary Science Letters, vol. 26, pp. 423-500.

Sinninghe Damsté, J.S., Hartgers, W.A., Baas, M., and De Leeuw, J.W. (1993) Characterization of high-molecular-weight organic matter in marils of the Salt IV Formation of the Mulhouse Basin. Organic Geochemistry, vol. 20, pp. 1237-1251.

Sinninghe Damsté, J.S., Marika, D.K., Koster, J., and Schouten, S. (1998) Sulfurized carbohydrates: an important sedimentary sink for organic carbon? Earth and Planetary Science Letters, vol. 164, pp. 7-13.

Smith, D.G., and Bailey, R.J. (2017) Comment on "Astronomical constraints on the duration of the Early Jurassic Pliensbachian Stage and global climatic fluctuations" [Earth Planet. Sci. Lett. 455 (2016) 140-165]. Earth and Planetary Science Letters, vol. 481, p 412-414.

Smoliar, M.I., Walker, R.J., and Morgan, J.W. (1996) Re-Os Ages of Group IIA, IIIA, IVA, and IVB Iron Meteorites. Science, vol. 271, pp. 1099-1102.

Spivak, J. (1949) Jurassic sections in Foothills of Alberta and northeastern British Columbia. Bulletin of the American Association of Petroleum Geologists, vol. 33, pp. 533-546.

Strauss, H., Kump, L.R., Lepland, A., Fallick, A.E., Hanski, E., Prave, A.R., and Melezhik, V.A. (2013) Reading the archive of Earth's oxygenation. Springer, London, pp. 1510.

Sundby, B., Marinez, P., and Gobeil, C. (2004) Comparative geochemistry of cadmium, rhenium, uranium, and molybdenum in continental margin sediments. Geochimica et Cosmochimica Acta, vol. 68, pp. 2485-2493.

Svensen, H., Planke, S., Chevallier, L., Malthe-Sorenssen, A., Corfu, F., Jamtveit, B., 2007. Hydrothermal venting of greenhouse gases trigger Early Jurassic global warming. Earth and Planetary Science Letters, vol. 256, pp. 554-566.

Tegelaar, E.W., De Leeuw, J.W., Derenne, S., and Largeau, C. (1989) A reappraisal of kerogen formation. Geochimica et Cosmochimica Acta, vol. 53, pp. 3103-3106.

Them II, T.R. (2016) Biogeochemical cycling and paleoenvironmental reconstructions of the Toarcian Ocean Anoxic Event from western North America. Doctoral Thesis, Virginia Polytechnic Institute and State University.

Them, T.R., Gill, B.C., Caruthers, A.H., Gröke, D.R., Tulsky, E.T., Martindale. R.C., Poulton, T.P., and Smith, P.L. (2017) High-resolution carbon isotope records of the Toarcian Oceanic

Anoxic Event (Early Jurassic) from North America and implications for the global drivers of the Toarcian carbon cycle. Earth and Planetary Science Letters, vol. 459, pp. 118-126.

Them, T.R., Gill, B.C., Selby, D., Gröke, D.R., Friedman, R.M., and Owens, J.D. (2017) Evidence for rapid weathering response to climatic warming during the Toarcian Oceanic Anoxic Event. Nature Scientific Reports, vol. 7, pp. 5003.

Them, T.R., Gill, B.C., Caruthers, A.H., Gerhardt, A.M., Gröcke, D.R., Lyons, T.W., Marroquin, S.M., Nielsen, S.G., Trabucho Alexandre, J.P., and Owens, J.D. (2018). Thallium isotopes reveal protracted anoxia during the Toarcian (Early Jurassic) associated with volcanism, carbon burial, and mass extinction. PNAS, vol., pp. 1-6.

Theirstein, H.R., and Younger, J.R. (2004) Coccolithophores: From Molecular Processes to Global Impact. New York, Springer-Berlag Berlin Heidelberg, pp. 149, 263.

Tribovillard, N., Riboulleau, A., Lyons, T., and Baudin, F. (2004) Enhanced trapping of molybdenum by sulfurized marine organic matter of marine origin in Mesozoic limestones and shales. Chemical Geology, vol. 213, pp. 385-401.

Tucker, R.D., Bradley, D.C., Ver Straeten, C.A., Harris, A.G., Erbert, J.R., and McCutcheon, S.R. (1998) New U-Pb zircon ages and the duration and division of Devonian time. Earth and Planetary Science Letters, vol. 158, pp. 175-186.

Turgeon, S.C., Creaser, R.A., and Algeo, T.J. (2007) Re-Os depositional ages and seawater Os estimates for the Frasnian-Famennian boundary: Implications for weathering rates, land plant evolution, and extinction mechanisms. Earth and Planetary Science Letters, vol. 261, pp. 649-661.

Turgeon, S., and Creaser, R.A. (2008) Cretaceous oceanic anoxic event 2 triggered by a massive magmatic episode. Nature Letters, vol. 454, pp. 323-327.

Vandenbroucke, M., and Largeau, C. (2007) Kerogen, origin, evolution and structure. Organic Geochemistry, vol. 38, pp. 719-833.

Van de Schootbrugge, B., Bailey, T.R., Rosenthal, Y., Katz, M.E., Wright, J.D, Miller, K.G., Feist-Burkhardt, S., and Falkowski, P.G. (2005) Early Jurassic climate change and the radiation of organic-walled phytoplankton in the Tethys Ocean. Paleobiology, vol. 31, pp. 73-97.

Van Der Meer, D.G., Zeebe, R.E., van Hinsbergen D.J.J, Sluijs, A., Spakman, W., and Orsvik, T.H. (2014) Plate tectonic controls on atmospheric CO2 levels since the Triassic. PNAS, vol. 111, pp. 4380-4385.

Van Kamm-Peters, H.M.E., Schouten, S., Koster, J., and Sinninghe Damste, J.S. (1998) Controls on the molecular and carbon isotopic composition of organic matter deposited in a Kimmeridgian euxinic shelf sea: Evidence for preservation of carbohydrates through sulfurization. Geochimica et Cosmochimica Acta, vol. 62, pp. 3259-3283.

Venturi, F., Bilotta, M., Ricci, C. (2006) Comparison between western Tethys and eastern Pacific ammonites: futher evidence for a possible late Sinemurian-early Pliensbachian trans-Pangaean marine connection. Geology, vol. 143, pp. 699-711.

Verati, C., Rapaille, C., Feraud, G., Marzoli, A., Bertrand, H., and Youbi, N. (2007) ^{40}Ar/^{39}Ar ages and duration of the Central Atlantic Magmatic Province volcanism in Morocco and Portugal and its relation to the Triassic-Jurassic boundary. Palaeogeography, Palaeoclimatology, Palaeoecology, vol. 244, pp. 308-325.

Whiticar, M.J. (1996) Stable isotope geochemistry of coals, humic kerogens and related natural gases. International Journal of Coal Geology, vol. 32, pp. 191-215.

Wilson, S.A. (2012) Certificate of Analysis: Brush Creek Shale, SBC-1. United States Geological Survey, Denver, Colorado.
https://crustal.usgs.gov/geochemical_reference_standards/pdfs/SBC-1.pdf (accessed: 01/01/2016)

Woodhouse, O.B., Ravizza, G., Falkner, K.K., Statham, P.J., and Peucker-Ehrenbrink, B. (1999) Osmium in seawater: vertical profiles of concentration and isotopic composition in the eastern Pacific Ocean. Earth and Planetary Science Letters, vol. 173, pp. 223-233.

Wright, S.C. (2015) Applications of the Rhenium-Osmium Isotopic System, and Platinum and Iridium Abundances in Organic-rich Mud rocks: A Geochronology, Geochemistry, and Redox Study. PhD Thesis. University of Houston.

Yamashita, Y., Takahashi, Y., Haba, H., Enomoto, S, and Shimizu, H. (2007) Comparison of reductive accumulation of Re and Os in seawater-sediment systems. Geochimica et Cosmochimica Acta, vol. 71, pp. 3458-3475.

Xu, H., Barton, L.L., Zhang, P., and Wang, Y. (2000) TEM Investigation of U+6 and Re7+ Reduction by Dsulfovibrio desulfuricans, a Sulfate-Reducing Bacterium. Material Research Society, vol. 608, pp. 299-304.

Xu, G., Hannah, J.L., Stein, H.J., Mørk, A., Os Vigran, J., Bingen. B., Schutt, D.L., and Lundschien B.A. (2013) Cause of Upper Triassic climate crisis revealed by Re-Os geochemistry of Boreal black shales. Palaeogeography, Palaeoclimatology, Palaeoecology, vol. 395, pp. 222-232.

Yang, G., Hannah, J.L, Zimmerman, A., Stein, H.J., and Bekker, A. (2009) Re-Os depositional age for Archean carbonaceous slates from the southwestern Superior Province: Challenges and insights. Earth and Planetary Science Letters, vol. 280, pp. 83-92.

York, D. (1969) Least Squares Fitting of a Straight Line with Correlated Errors. Earth and Planetary Science Letters, vol. 5, pp. 320-324.

Appendix
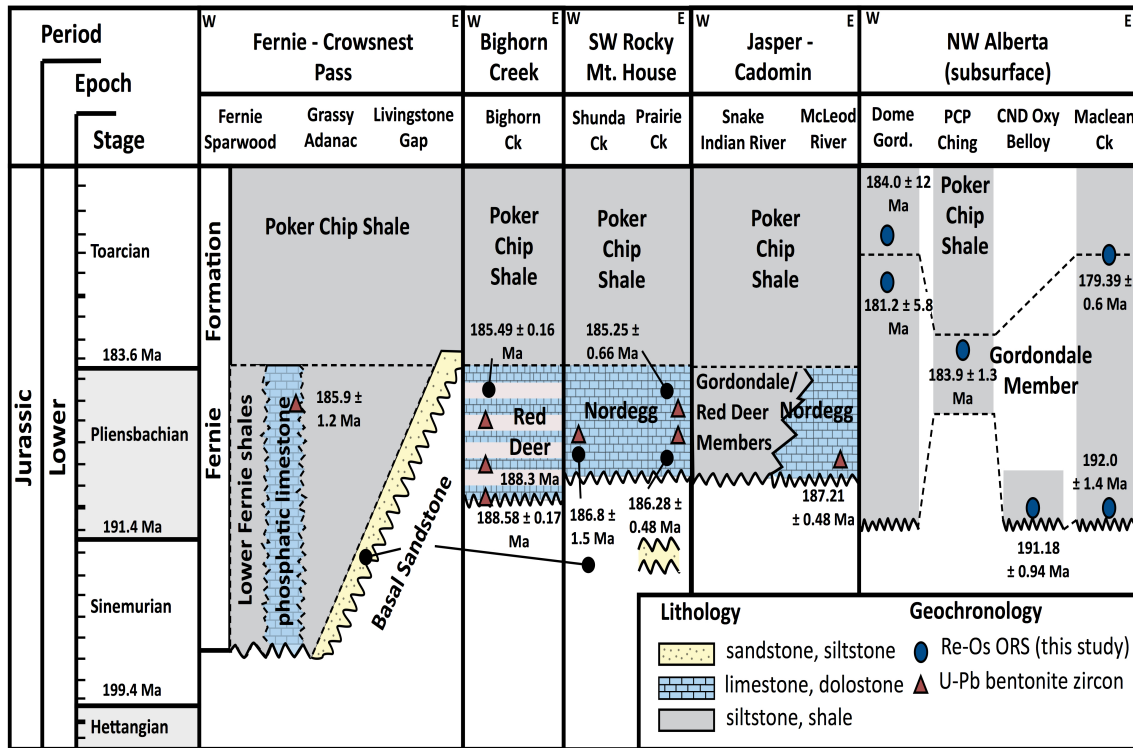
Figure 10. 1 Depositional age correlations of Lower Fernie stratigraphy in the WCSB (modified after Păna et al. 2018 a,b). U-Pb dates are taken from Hall et al. (2004), Them et al. (2017), and Păna et al. (2018 a,b). See Figure 3.1 for spatial relationships of Lower Fernie stratigraphy.

Table 1 Re-Os Sample Cores

Core	Well Name	UWI	Stratigraphic Unit	Subunit
TS00-16 to TS00-20	PCP Ching	6-32-78-5W6	Upper Gordondale	1B
TS00-27 to TS00-31	Canadian Oxy Belloy	6-19-78-25W5	Lower Gordondale	1A
JT17-19201	Dome Gordondale	7-31-79-10W6	Lower Gordondale	1A
JT17-19202	Dome Gordondale	7-31-79-10W6	Lower Gordondale	1A
JT17-19203	Dom Gordondale	7-31-79-10W6	Lower Poker Chip	3B
JT17-19204	Dome Gordondale	7-31-79-10W6	Upper Gordondale	3A
JT17-19205	CNRL Maclean Creek	13-28-73-21W6	Lower Gordondale	1A
JT17-19206	CNRL Maclean Creek	13-28-73-21W6	Upper Gordondale	3A
JT17-19207	CNRL Maclean Creek	13-28-73-21W6	Lower Poker Chip	3B

Note: UWI = Unique well identifier; TOC = Total Organic Carbon; TOC values sourced from Riediger (1990)

Lithology	Depth (m)	Gamma Ray (API)	TOC (wt.%)
Calcitic mudstone	1221.78-1221.94	-	-
Calcitic mudstone	1018.65-1018.39	-	-
Calcitic mudstone	1557.35-1557.54	195	~ 3.41-3.54
Calcitic mudstone	1555.82-1556.04	285	~ 14
Calcitic mudstone	1537.15-1537.28	170	~ 6
Argillaceous mudstone	1537.86-1538.11	240	-
Calcitic mudstone	1193.04-1193.28	273	-
Argillaceous mudstone	1169.38-1169.62	260	-
Calcitic mudstone	1168.50-1168.70	220	-

Table 2 Re and Os Procedural Blanks

Month	Re (ppb)	±	Os (ppt)	±	^{187}Re/^{188}Os	±	^{187}Os/^{188}Os	±
17-04-05	0.0099		0.467		118.06		0.163	
17-05-04	0.0082		0.028		1311.54		0.000	
17-05-16	0.0119		0.143		677.32		0.000	
17-06-02	0.0121		0.264		656.20		0.847	
17-06-13	0.0086		0.092		561.89		0.236	
17-06-20	0.0134		0.045		1802.76		0.147	
17-07-07	0.0128		0.069		1245.89		0.272	
17-07-13	0.0141		0.109		753.83		0.152	
17-08-05	0.0090		0.196		271.51		0.184	
17-09-08	0.0078		0.039		1441.41		0.275	
17-09-21	0.0102		0.062		1449.77		0.514	
17-10-19	0.0114		0.010		5794.94		0.731	
17-11-01	0.0127		0.178		401.27		-	
17-11-15	0.0094		0.063		778.37		-	
17-11-20	0.0168		0.017		245.76		-	
17-12-14	0.0094		0.032		1789.78		-	
18-05-10	0.0064		0.032		1223.96		-	
Mean	0.0108		0.127		935.47		0.293	
Median	0.0102		0.081		999.86		0.254	
Standard Deviation	0.0026		0.125		516.69		0.257	

Table 3 Re-Os data for subunit 1A of the Lower Radioactive Unit of the Gordondale Member

Sample	Re (ppb)	±	Os (ppt)	±	^{192}Os (ppt)
TS-0027	181.26	0.35	1304.83	6.41	370.52
TS-0027-RPT*	181.34	0.36	1309.16	7.09	371.41
TS-0028*	146.30	0.28	1172.42	5.37	345.16
TS-0028-RPT	146.46	0.28	1175.05	5.30	346.02
TS-0028-RPT2	145.28	0.29	1164.73	5.16	342.90
TS-0029*	166.20	0.32	1164.26	5.32	326.15
TS-0030*	302.54	0.58	1602.36	7.82	391.10
TS-0031*	288.77	0.55	1354.33	8.67	304.19
TS-0031-RPT	290.57	0.55	1385.21	7.56	313.83
JT17-19201A*	62.63	0.12	798.91	3.05	259.73

JT17-19201C*	42.50	0.09	483.49	2.14	157.00
JT17-19201D*	30.55	0.07	319.06	1.63	105.51
JT17-19201F*	32.91	0.07	346.77	1.71	114.45
JT17-19201G*	42.05	0.09	558.23	2.26	188.39
JT17-19202A*	559.14	1.07	5731.85	18.86	1888.24
JT17-19202A-RPT	496.20	0.95	5058.71	18.10	1665.74
JT17-19202C*	243.66	0.48	2460.69	8.45	822.85
JT17-19202E*	272.26	0.53	3812.70	11.54	1321.97
JT17-19202F*	308.90	0.60	4480.95	12.70	1564.56
JT17-19202G*	303.72	0.59	3486.65	11.09	1183.18
JT17-19202H*	318.92	0.61	3818.22	11.77	1300.22
JT17-19202I*	318.11	0.61	4128.45	12.21	1423.72
JT17-19202J*	283.59	0.55	4223.65	12.06	1482.35
JT17-19205B	136.35	0.26	1184.25	4.79	358.74
JT17-19205B-RPT*	127.80	0.25	1107.13	4.83	334.90
JT17-19205D*	144.83	0.28	945.39	4.68	257.46
JT17-19205I	147.73	0.29	959.40	4.77	260.30
JT17-19205I-RPT*	138.05	0.27	893.78	4.85	242.44
JT17-19205K*	128.11	0.25	1032.10	4.53	304.87
JT17-19205L*	134.74	0.26	1153.31	4.93	347.52

$^{187}Re/^{188}Os$	±	$^{187}Os/^{188}Os$	±	rho	$^{187}Os/^{188}Os_i$
973.21	3.08	3.607	0.014	0.68	0.51
971.30	4.42	3.617	0.017	0.88	0.53
843.24	2.67	3.212	0.012	0.72	0.53
842.05	2.65	3.209	0.011	0.74	0.53
842.87	2.64	3.212	0.011	0.72	0.53
1013.78	3.18	3.759	0.013	0.77	0.54
1538.94	4.48	5.428	0.017	0.74	0.54
1888.58	7.00	6.553	0.031	0.68	0.55
1841.98	5.95	6.431	0.023	0.76	0.58
479.69	1.42	2.196	0.007	0.71	0.67
538.59	2.22	2.208	0.009	0.84	0.50
575.92	3.24	2.032	0.011	0.89	0.20
572.05	3.00	2.051	0.011	0.88	0.23
444.08	1.63	1.840	0.007	0.75	0.43
589.10	1.30	2.069	0.005	0.57	0.21
592.61	1.42	2.073	0.006	0.57	0.20
589.10	1.62	1.926	0.006	0.72	0.06
409.71	0.97	1.589	0.004	0.62	0.29
392.78	0.87	1.526	0.004	0.61	0.28

510.67	1.23	1.788	0.005	0.64	0.17
487.96	1.13	1.755	0.004	0.62	0.21
444.50	1.01	1.639	0.004	0.62	0.23
380.60	0.86	1.479	0.004	0.60	0.28
756.14	2.20	2.909	0.009	0.76	0.51
759.19	2.44	2.924	0.010	0.76	0.51
1119.09	3.90	4.083	0.015	0.81	0.53
1129.03	4.02	4.126	0.015	0.83	0.54
1132.80	4.32	4.129	0.018	0.77	0.53
836.01	2.69	3.176	0.011	0.79	0.52
771.32	2.36	2.965	0.010	0.74	0.51

Table 4 Strontium Batch #1

Samples	CaCO$_3$ wt.%	[a]Mg/Ca	[a]Mn/Sr	[a][Sr] ppm
TS0027	21.40	0.04	0.07	438.96
TS0029	19.64	0.05	0.06	476.55
JT17-19205I	19.63	0.05	0.09	465.93
JT17-19205L	16.72	0.05	0.10	379.74
JT17-19207A	13.41	0.05	0.10	445.66
JT17-19207B	12.28	0.06	0.15	332.90
TS0017	26.53	0.04	0.02	1451.60
TS0019	29.08	0.03	0.02	1691.04

[a] *Derived from HCl-soluble phases and measured on ICP-MS*
[b] *Measured on MC-ICP-MS*
[c] *Estimated from Re-Os ORS age data*
[d] *0.035 N Acetic Acid Treament*

[b]87Sr/86Sr	±	[b]87Sr/86Sr	±	[c]Deviation from seawater	[d]% Dissolved Calcite	[d]% Dissolved Calcite
Leach 2		Leach 3			Leach 2	Leach 3
0.707952	0.000031	0.707814	0.000026	0.000323	16.15	40.37
0.707770	0.000032	0.707672	0.000030	0.000176	17.56	43.90
0.707794	0.000034	0.707630	0.000021	0.000145	15.86	43.62
0.707720	0.000032	0.707683	0.000025	0.000193	20.33	40.65
0.707640	0.000033	0.707340	0.000028	0.000002	17.94	41.87
0.707564	0.000034	0.707365	0.000027	0.000029	19.79	39.57
0.707179	0.000023	0.707215	0.000024	-0.000053	16.81	40.35
0.707194	0.000065	0.707209	0.000021	-0.000080	15.91	37.13

Table 5 Geochemical Analysis

Sample	Al (ppm)	Mg (ppm)	P (ppm)	K (ppm)	Ca (ppm)	Mn (ppm)	Sr (ppm)
TS0027	1536.76	3789.41	1891.19	815.87	85695.21	30.52	438.96
TS0028	3555.22	9392.29	1905.75	1653.11	65052.09	56.01	354.02
TS0029	1112.31	3929.17	1302.11	588.31	78636.51	28.92	476.55
TS0030	2029.31	9473.45	1282.14	1257.70	61246.08	52.44	329.00
TS0031	2244.30	11394.48	1413.17	1451.37	56791.72	72.17	263.17
JT17-19205B	883.48	4996.08	1775.37	867.96	75636.97	43.97	349.64
JT17-19205B-RPT	847.00	4782.51	1739.00	848.77	74781.41	44.68	351.08
JT17-19205D	1009.62	6134.20	1384.71	939.39	77200.55	49.46	364.02
JT17-19205I	997.57	3703.71	1586.95	888.43	78586.97	41.26	465.93
JT17-19205K	1059.63	4152.06	1703.09	1050.28	80303.70	47.13	481.31
JT17-19205L	961.07	3436.25	1502.17	900.17	66951.85	38.85	379.74
JT17-19207A	2369.95	2520.74	1588.54	1189.03	53690.83	46.79	445.66
JT17-19207B	2496.17	2818.12	1729.97	1248.97	49178.94	50.88	332.90
JT17-19207C	2490.35	2669.10	1526.00	1133.98	53081.15	52.17	364.48
JT17-19207D	2158.76	2406.24	1117.98	1036.31	54626.12	48.72	388.06
JT17-19207E	2129.92	2398.50	950.01	1098.35	56538.05	52.92	443.48
JT17-19207F	2266.85	2893.20	891.04	1245.39	65291.36	65.58	427.36
JT17-19207G	1821.32	2167.22	799.75	995.37	51714.47	50.78	362.03
JT17-19207G-RPT	1820.70	2194.24	781.79	974.02	51809.89	49.93	364.43
TS00-16	1836.42	5460.67	2212.90	984.30	78171.64	73.96	772.13
TS00-17	1176.58	4693.18	3832.41	542.37	106234.49	27.44	1451.60
TS00-18	771.84	2573.20	2689.81	382.93	105985.77	26.45	830.60
TS00-19	1218.48	3902.86	2738.32	523.32	116427.22	32.11	1691.04

Note: Major and Trace Element Concentrations are derived from 6 N HCl-soluble mineral phases

Rb (ppm)	V (ppm)	Cr (ppm)	Fe (ppm)	Co (ppm)	Ni (ppm)	Cu (ppm)
4.56	46.56	24.23	466.81	1.09	85.31	14.77
10.81	54.56	27.67	785.39	1.52	42.32	7.32
4.91	26.10	14.75	318.86	0.95	45.34	5.04
7.84	45.44	22.93	642.24	1.71	85.57	14.85
8.53	46.15	23.04	685.79	1.77	65.82	11.16

7.51	42.61	12.15	361.24	1.00	52.63	4.40
7.48	42.89	12.23	362.79	1.03	53.58	4.54
7.19	32.79	9.61	411.04	1.68	79.47	5.90
7.39	29.52	9.93	335.32	1.51	78.85	4.96
8.68	31.19	11.94	421.14	1.51	76.83	6.72
7.36	26.51	10.70	380.19	1.31	72.36	6.39
11.56	16.19	7.31	835.52	2.30	30.78	1.95
12.09	17.92	7.81	944.75	2.32	27.38	1.84
9.54	18.36	7.58	871.51	2.58	34.68	1.68
8.90	17.77	6.91	814.86	2.45	32.80	1.14
9.29	17.60	6.96	930.12	2.62	32.21	0.99
10.63	20.71	8.39	1231.83	3.46	40.81	1.45
8.72	15.94	6.28	888.70	2.86	35.16	1.47
8.62	15.85	6.25	873.90	2.87	34.65	1.48
4.89	78.58	16.32	14326.23	6.56	289.94	80.48
2.44	55.60	8.48	483.36	1.19	194.00	7.72
1.82	50.49	7.00	405.29	1.02	161.31	6.28
2.36	48.67	6.92	578.06	1.23	119.34	11.00

Zn (ppm)	Se (ppm)	Mo (ppm)	Ba (ppm)	Re (ppb)
159.78	6.40	103.71	525.34	-
340.53	4.66	137.28	585.52	-
74.88	5.98	82.34	514.29	-
217.27	5.20	241.53	477.40	90.87
107.40	5.00	165.43	469.24	90.90
250.41	6.56	133.41	276.48	-
254.40	6.53	132.00	272.23	-
102.49	5.86	103.59	215.76	-
73.62	6.44	98.06	118.54	-
323.08	5.86	105.40	162.83	-
395.69	4.93	90.42	147.58	-
129.73	3.79	41.82	546.31	30.21
198.58	3.21	39.64	639.91	-
129.41	3.27	43.66	244.40	-
90.18	3.60	48.66	180.60	-
51.87	3.49	49.45	215.14	-
54.47	3.84	59.01	210.37	-
62.87	2.89	47.73	258.58	-
62.86	2.89	47.55	258.57	-

611.59	12.07	261.90	463.84	242.05
641.64	7.24	398.72	406.67	-
942.11	6.15	297.77	329.11	-
815.76	7.84	289.63	327.75	-

Table 6
Geochemical data from leachate with acetic acid

Sample	Mg (ppm)	Al (ppm)	P (ppm)	K (ppm)	Ca (ppm)	V (ppm)
19207A-L2	16626.36	67836.24	24045.77	47777.22	1412796.53	9.82
TS0017-L2	2829.34	11582.20	3683.55	5414.81	401858.69	6.91
TS0029-L2	2639.53	11827.07	5056.28	5778.92	347935.86	11.97
19207A-L3	1736.10	4355.02	1479.48	3524.51	224898.91	0.43
TS0017-L3	3040.65	5698.57	1175.54	1441.29	254875.44	5.87
TS0029-L3	1552.63	3174.50	1379.06	1857.79	258193.43	13.40

Cr (ppm)	Fe (ppm)	Mn (ppm)	Co (ppm)	Ni (ppm)	Cu (ppm)	Zn (ppm)
92.75	42712.95	395.31	32.04	545.22	25.50	18.71
16.51	6734.00	34.06	6.05	827.19	4.79	83.41
27.11	7835.93	40.94	5.10	369.02	4.16	-
6.68	2688.70	139.82	7.70	95.57	1.28	91.57
4.95	1677.23	54.47	3.37	428.39	1.84	482.70
4.08	1956.64	60.18	3.10	181.84	2.12	110.20

Se (ppm)	Rb (ppm)	Sr (ppm)	Mo (ppm)	Cd (ppm)	Ba (ppm)	Re (ppm)
119.20	189.38	10053.01	2940.23	5.97	22071.80	-
15.31	31.07	4774.65	4440.43	8.02	4046.65	0.91
15.61	31.95	1448.90	1332.79	2.80	4399.99	-
4.31	11.08	1602.40	89.53	1.10	1534.42	-
4.09	15.22	5452.50	2097.44	5.90	1402.49	0.37
3.55	8.26	1125.07	140.37	7.04	1486.80	-

Table 7 Strontium Isotope Batch #2

Samples	CaCO$_3$ wt.%	[a][Rb] ppm	[a][Sr] ppm	[b]^{87}Sr/^{86}Sr	±	^{87}Rb/^{86}Rb	^{87}Sr/^{86}Sr$_{corr}$
					Leach 2		
TS0029-RPT	19.64	163.74	7425.61	0.707855	0.000026	0.092792	0.707603
JT17-19207A-RPT	13.41	189.38	10053.01	0.707573	0.000040	0.079273	0.707371
TS0017-RPT	26.53	194.18	29841.58	0.707244	0.000029	0.027382	0.707173

Samples	CaCO$_3$ wt.%	[a][Rb] ppm	[a][Sr] ppm	[b]^{87}Sr/^{86}Sr	±	^{87}Rb/^{86}Rb	^{87}Sr/^{86}Sr$_{corr}$
					Leach 3		
TS0029-RPT	19.64	158.50	21579.45	0.707669	0.000029	0.030908	0.707585
JT17-19207A-RPT	13.41	171.60	24814.89	0.707364	0.000022	0.029099	0.707290
TS0017-RPT	26.53	174.32	62438.69	0.707230	0.000027	0.011749	0.707200

[a] *Derived from 0.035 N Acetic Acid-soluble phases and measured on ICP-MS*

[b] *Measured on MC-ICP-MS*

[c] *Estimated from Re-Os ORS age data*

[d] *0.035 N Acetic Acid Treament*

[c]Deviation from seawater	[a]% Dissolved Calcite Leach 2
0.000178	35.36
0.000101	31.97
0.000004	31.75

[c]Deviation from seawater	[a]% Dissolved Calcite

	Leach 3
0.000160	63.15
0.000020	63.94
0.000031	59.98

Table 8

Re-Os data for the Lower Poker Chip and Upper Gordondale Member

Sample	Re (ppb)	±	Os (ppt)	±	¹⁹²Os (ppt)
TS0016	291.35	0.56	1392.90	9.05	322.58
TS0016-RPT	311.99	0.59	1486.86	8.50	344.01
TS0016-RPT2	254.72	0.50	1207.85	8.64	279.17
TS0017*	261.79	0.50	1363.92	7.25	338.33
TS0018	210.37	0.40	1071.18	8.25	263.60
TS0018-RPT*	213.15	0.41	1090.13	5.82	267.14
TS0019	229.52	0.44	1206.06	6.44	298.02
TS0019-RPT*	230.82	0.44	1213.39	8.90	301.75
TS0020	221.71	0.42	1508.22	11.80	427.86
TS0020-RPT*	219.43	0.42	1490.31	6.47	419.90
JT17-19203A*	235.51	0.45	1245.06	6.35	310.05
JT17-19203B*	138.22	0.27	792.24	4.69	204.74
JT17-19203C	117.08	0.23	638.05	3.99	162.41
JT17-19203C-RPT*	121.15	0.24	662.56	4.14	168.48
JT17-19203D*	131.56	0.26	732.16	4.42	187.54
JT17-19203D-RPT	124.42	0.24	690.79	4.28	176.80
JT17-19203E*	103.96	0.21	580.39	3.73	148.71
JT17-19203F*	90.25	0.18	536.55	3.61	143.09
JT17-19203G	121.50	0.24	706.00	4.29	184.74
JT17-19203G-RPT*	126.19	0.25	734.04	4.77	192.24
JT17-19203H*	149.87	0.29	1080.72	5.87	309.82
JT17-19204A*	256.23	0.49	1939.15	7.47	576.60
JT17-19204B	274.34	0.52	1706.49	7.11	473.92
JT17-19204B-RPT*	270.07	0.51	1686.74	7.13	467.03
JT17-19204B-RPT2	261.27	0.50	1631.78	6.98	453.48
JT17-19204C*	402.43	0.76	2222.43	9.57	577.45

JT17-19204D	340.56	0.65	1711.61	8.13	426.27
JT17-19204D-RPT*	333.94	0.64	1686.80	7.89	420.43
JT17-19204D-RPT2	320.71	0.61	1612.03	7.90	401.39
JT17-19204E*	407.56	0.77	1813.01	9.09	412.21
JT17-19204F*	412.47	0.78	2133.93	9.63	537.64
JT17-19204G*	475.32	0.90	2578.48	11.34	665.21
JT17-19206B*	275.00	0.52	1363.32	6.89	335.97
JT17-19206B-RPT	266.94	0.51	1328.42	6.59	188.90
JT17-19206C*	231.13	0.44	1152.70	5.86	285.09
JT17-19206E	283.56	0.54	1337.04	6.58	320.14
JT17-19206E-RPT*	276.71	0.52	1315.33	6.65	314.75
JT17-19206G*	242.22	0.46	1182.83	6.14	288.07
JT17-19206H*	194.27	0.37	946.59	5.23	232.02
JT17-19206H-RPT	192.33	0.37	939.45	4.38	230.55
JT17-19206H-RPT2	163.11	0.33	788.65	6.84	192.45
JT17-19206J*	199.94	0.38	892.61	5.37	204.68
JT17-19207A*	101.01	0.20	655.75	3.59	184.41
JT17-19207B*	89.82	0.18	653.69	3.42	192.15
JT17-19207C*	92.62	0.18	704.88	3.47	210.28
JT17-19207D	99.69	0.20	697.69	4.78	202.54
JT17-19207D-RPT*	103.14	0.20	723.98	5.33	209.74
JT17-19207D-RPT2	104.39	0.20	727.89	3.56	210.80
JT17-19207E*	88.21	0.18	606.14	3.51	174.22
JT17-19207E-RPT	72.29	0.15	498.07	2.98	143.08
JT17-19207F	98.13	0.19	663.50	3.46	190.01
JT17-19207F-RPT	98.25	0.19	626.46	3.72	174.46
JT17-19207F-RPT2*	98.85	0.19	627.79	4.14	174.96
JT17-19207G	101.30	0.20	644.08	3.77	180.35
JT17-19207G-RPT*	99.31	0.19	640.61	3.56	179.42

$^{187}Re/^{188}Os$	±	$^{187}Os/^{188}Os$	±	rho	$^{187}Os/^{188}Os_i$
1796.79	6.93	6.128	0.031	0.68	0.66
1804.24	5.93	6.141	0.024	0.70	0.65
1815.18	10.93	6.155	0.038	0.92	0.63
1539.33	4.74	5.220	0.020	0.68	0.54
1587.71	7.46	5.323	0.038	0.60	0.49
1587.33	5.50	5.377	0.020	0.80	0.55
1532.16	4.93	5.270	0.020	0.72	0.61
1521.77	6.58	5.188	0.035	0.59	0.56

1030.90	5.42	3.618	0.032	0.55	0.48
1039.61	2.90	3.694	0.011	0.72	0.53
1511.14	4.95	5.171	0.018	0.79	0.62
1343.05	6.06	4.708	0.023	0.85	0.66
1434.20	7.43	4.895	0.026	0.91	0.57
1430.60	7.33	4.908	0.026	0.90	0.60
1395.54	6.63	4.817	0.024	0.88	0.61
1400.00	6.86	4.827	0.025	0.87	0.61
1390.78	7.73	4.814	0.027	0.93	0.62
1254.67	7.72	4.329	0.028	0.91	0.55
1308.41	6.42	4.556	0.024	0.88	0.61
1305.94	6.53	4.546	0.026	0.80	0.61
962.33	3.66	3.501	0.017	0.70	0.60
884.05	2.11	3.105	0.008	0.64	0.43
1151.61	2.91	3.858	0.011	0.68	0.37
1150.38	2.94	3.892	0.011	0.68	0.41
1146.20	3.05	3.850	0.011	0.71	0.38
1386.46	3.36	4.642	0.012	0.66	0.45
1589.38	4.39	5.170	0.016	0.71	0.36
1580.16	4.32	5.159	0.015	0.72	0.38
1589.51	4.49	5.172	0.017	0.70	0.36
1966.98	5.52	6.382	0.020	0.73	0.43
1526.26	3.84	5.023	0.014	0.67	0.41
1421.51	3.34	4.729	0.013	0.61	0.43
1628.37	5.04	5.304	0.018	0.76	0.40
1619.19	4.89	5.280	0.017	0.76	0.41
1612.84	5.24	5.258	0.018	0.80	0.40
1762.11	5.28	5.680	0.018	0.78	0.38
1748.94	4.46	5.688	0.019	0.59	0.42
1672.79	5.53	5.457	0.019	0.80	0.42
1665.78	6.42	5.374	0.022	0.85	0.36
1659.65	4.35	5.358	0.016	0.69	0.36
1686.10	14.23	5.431	0.050	0.89	0.36
1943.33	8.26	6.264	0.028	0.87	0.41
1089.70	4.85	3.716	0.017	0.86	0.41
929.92	3.91	3.228	0.015	0.81	0.41
876.24	3.56	3.071	0.013	0.84	0.41
979.17	5.26	3.364	0.025	0.68	0.39
978.36	5.15	3.386	0.028	0.59	0.42
985.15	3.53	3.390	0.014	0.78	0.40
1007.27	5.08	3.473	0.019	0.86	0.42
1005.06	5.62	3.478	0.020	0.91	0.43
1027.39	4.33	3.513	0.015	0.86	0.40

1120.38	5.00	3.826	0.020	0.76	0.43
1123.99	5.63	3.818	0.025	0.72	0.41
1117.44	5.76	3.764	0.020	0.90	0.37
1101.13	3.72	3.761	0.018	0.61	0.42

Table 9 Re-Os data of water extraction experiment

Sample	Temp. (°C)	Re (ppb)	±	Os (ppt)	±
SBC-1-0011-FEB17*	240	10.11	0.04	93.3	1.0
SBC-1-0011-APR17*	240	10.52	0.03	95.7	1.0
SBC-1-0011-NOV17*	240	10.41	0.04	100.5	1.2
SBC-1-0011-G-AT	18.5	2.13	0.03	6.5	0.5
SBC-1-0011-G-100	100	8.08	0.03	-	-
SBC-1-0011-G-150	150	9.23	0.03	57.2	1.0
SBC-1-0011-G-240	240	9.39	0.03	109.3	1.2
SBC-1-0011-G-240-RPT	240	9.35	0.03	86.4	1.3
SBC-1-0011-G-240-RPT2	240	9.58	0.03	108.7	1.8
SBC-1-0011-G-275	275	8.57	0.03	103.9	1.3

* denotes conventional whole-rock acid digestion procedure

$^{187}Re/^{188}Os$	±	$^{187}Os/^{188}Os$	±	rho
863.223	12.048	5.133	0.071	0.95
886.978	12.152	5.292	0.074	0.94
801.629	12.983	4.774	0.081	0.92
2392.171	525.921	4.096	0.906	0.99
-	-	-	-	-
1285.527	38.210	5.144	0.164	0.92
583.162	8.153	3.263	0.052	0.82
909.227	19.138	5.824	0.136	0.87
587.083	12.531	3.059	0.100	0.64
500.932	9.208	2.123	0.050	0.74

Table 10 Carbon isotope data

Sample ID	Strat Unit	Depth (m)	C$_{kerogen}$ wt.%	$\delta^{13}C_{Kerogen}$	±
JT17-19205B	Basal Gordondale	1193.084	39.26	-29.321	0.013
JT17-19205D	Basal Gordondale	1193.123	33.18	-28.711	0.014
JT17-19205I	Basal Gordondale	1193.206	32.74	-28.758	0.052
JT17-19205L	Basal Gordondale	1193.252	34.05	-29.466	0.007
JT17-19204A	Upper Gordondale	1537.886	9.44	-30.845	0.024
JT17-19204B	Upper Gordondale	1537.9208	6.88	-31.226	0.018
JT17-19204C	Upper Gordondale	1537.9436	10.26	-30.834	0.024
JT17-19204D	Upper Gordondale	1537.9704	10.85	-30.085	0.014
JT17-19204F	Upper Gordondale	1538.029	6.86	-30.942	0.014
JT17-19204G	Upper Gordondale	1538.0988	9.08	-30.802	0.016
JT17-19203A	Basal Poker Chip	1537.171	3.24	-30.272	0.017
JT17-19203C	Basal Poker Chip	1537.1915	3.11	-30.244	0.008
JT17-19203D	Basal Poker Chip	1537.2005	3.44	-30.066	0.007
JT17-19203F	Basal Poker Chip	1537.2205	3.67	-30.000	0.013
JT17-19203G	Basal Poker Chip	1537.245	3.72	-30.001	
JT17-19203H	Basal Poker Chip	1537.261	5.26	-29.588	0.022
JT17-19202A	Basal Gordondale	1555.84	11.14	-30.016	0.014
JT17-19202D	Basal Gordondale	1555.92	11.60	-30.459	0.007
JT17-19202F	Basal Gordondale	1555.95	7.23	-31.224	0.006
JT17-19202J	Basal Gordondale	1556.01	24.98	-30.665	0.016
JT17-	Basal Gordondale	1557.352	7.46	-29.899	0.015

19201A					
JT17-19201C	Basal Gordondale	1557.39	8.20	-29.997	0.011
JT17-19201E	Basal Gordondale	1557.44	10.36	-30.396	0.010
JT17-19201H	Basal Gordondale	1557.5	8.17	-30.172	0.010
TS-0027	Basal Gordondale	1018.63	14.06	-30.281	0.021
TS-0031	Basal Gordondale	1018.407	28.65	-29.864	0.020

Re (ppb)	^{192}Os (ppb)	^{187}Re/^{188}Os	^{187}Os/^{188}Os	Os$_g$
127.8	0.33	759.191	2.924	1.51
145.2	0.26	1121.915	4.083	1.99
138	0.24	1132.803	4.129	2.01
134.7	0.35	771.318	2.965	1.52
256.2	0.58	884.049	3.105	1.45
270.7	0.47	1152.907	3.892	1.74
402.4	0.58	1386.455	4.642	2.05
335	0.42	1584.967	5.159	2.20
412.5	0.54	1526.258	5.023	2.17
475.3	0.67	1421.509	4.729	2.07
235.5	0.31	1511.142	5.171	2.35
121.2	0.16	1430.600	4.908	2.23
131.6	0.19	1395.536	4.817	2.21
90.3	0.14	1256.074	4.329	1.98
121.5	0.19	1308.407	4.556	2.11
150.1	0.31	963.792	3.501	1.70
559.1	1.89	592.608	2.073	0.97
-	-	-	-	-
308.9	1.56	392.778	1.526	0.79
238.6	1.48	380.602	1.479	0.77
62.6	0.26	479.689	2.196	1.30
42.5	0.16	538.588	2.208	1.20
-	-	-	-	-
-	-	-	-	-
181.3	0.37	974.500	3.628	1.81
288.8	0.30	1888.579	6.553	3.02

Note: Os$_g$ denotes the ^{187}Os/^{188}Os initial ratio generated at time of oil emplacement at ~113 Ma.